Role of Iron Chelation in Inflammation and Infection

by

Maral Aali

Submitted in partial fulfilment of the requirements
for the degree of Doctor of Philosophy

at

Dalhousie University
Halifax, Nova Scotia
July 2020

I dedicate this thesis to my parents,

Efat Mazloomi Lengeh and Gholam Aali.

TABLE OF CONTENTS

LIST OF TABLES

LIST OF FIGURES

ABSTRACT

Iron is an essential element for most forms of life, as its redox-cycling capabilities enable its participation in numerous physiological reactions. However, iron levels must be tightly regulated to avoid free iron toxicity via catalysis of reactive oxygen species (ROS), which activate pro-inflammatory pathways. Iron dysregulation and excessive ROS production (oxidative stress) have been linked to dysregulated immune response and persistent infections. Two well-known examples of pathology induced by these changes are sepsis and cystic fibrosis. At the present time, there are no specific approved treatments for immune dysregulation. Additionally, antibiotic-resistant infections are becoming more difficult to clear. Iron chelators are potentially capable of addressing both needs by restricting iron availability for ROS production and reducing bacterial growth through nutritional immunity. Thus, we sought to investigate the anti-inflammatory and anti-bacterial effects of iron chelation by using DIBI, a highly specific, synthetic iron chelator. DIBI's efficacy *in vivo* was assessed in three murine models of sepsis (endotoxemia, CASP, and CASP-I) and it was compared to the FDA-approved iron chelators deferiprone, deferoxamine, and desferasirox. We found that DIBI effectively alleviated sepsis-induced leukocyte-endothelial interactions and preserved capillary perfusion in the intestinal microvasculature. Moreover, when administered in combination with an antibiotic, imipenem, DIBI reduced bacterial growth and improved survival outcome. *In vitro*, DIBI had a dose-specific effect on the secretion of IL-6 and IL-8 by nasal epithelial cells with cystic fibrosis disease-causing mutations. The lower studied dose of DIBI (25 μM) had a pro-inflammatory effect, whereas the higher dose (200 μM) had an anti-inflammatory effect. Overall, these findings suggest a promising role for the therapeutic application of DIBI, as a novel approach for attenuating the dysregulated inflammatory response and potential adjuvant in anti-bacterial therapy.

LIST OF ABBREVIATIONS AND SYMBOLS USED

ABC	ATP Binding Cassette
AI	Anemia of inflammation
APACHE	Acute physiology and chronic health evaluation
ARDS	Acute respiratory distress syndrome
ASL	Airway surface liquid
BCA	Bradford Calorimetric Assay
CA-AM	Calcein acetoxymethyl ester
CACF	Carleton Animal Care Facility
CASP	Colon ascendens stent peritonitis
CASP-I	Colon ascendens stent peritonitis with intervention
CF	Cystic fibrosis
CFTR	Cystic fibrosis transmembrane conductance regulator
CFU	Colony forming unit
CLP	Cecal ligation and puncture
CTCF	Corrected total cell fluorescence
DAMP	Damage associated molecular pattern
DCYTB	Duodenal cytochrome B
DFO	Deferoxamine
DFP	Deferiprone
DFX	Desferasirox
DMT-1	Divalent metal-ion transporter-1
EGDT	Early goal directed therapy
ENaC	Epithelial sodium channel
ETC	Electron transport chain
FACS	Fluorescence-activated cell sorting
FBS	Fetal bovine serum
FCD	Functional capillary density
FITC	Fluorescein isothiocyanate
H&E	Hematoxylin and eosin

H_2O_2	Hydrogen peroxide
HFE	Human factors engineering
ICAM-1	Intercellular adhesion molecule 1
IL	Interleukin
ILIP	Intracellular labile iron pool
IMI	Imipenem
iNOS	Inducible nitric oxide synthase
IP	Intraperitoneal
IV	Intravenous
IVM	Intravital microscopy
JAK	Janus Kinase
LPS	Lipopolysaccharide
MCC	Mucociliary clearance
MODS	Multiple organ dysfunction syndrome
MSS	Murine sepsis score
NaCl	Sodium chloride
NETs	Neutrophil extracellular traps
NF-κB	Nuclear factor kappa B
NO	Nitric oxide
PAMP	Pathogen associated molecular pattern
PBS	Phosphate-buffered saline
PCBP	Poly(rC)-binding protein
PLF	Peritoneal lavage fluid
PRR	Pattern recognition receptors
PVP	Polyvinylpyrrolidone
qSOFA	Quick sequential organ failure assessment score
RBC	Red blood cells
RNS	Reactive nitrogen species
ROS	Reactive oxygen species
RPM	Revolutions per minute
RPMI	Roswell Park Memorial Institute medium

SC	Subcutaneous
SOFA	Sequential organ failure assessment score
STAT	Signal transducer and activator of transcription
TJ	Tight junction
TLR	Toll-like receptor
TSA	Tryptic soy agar
V1	Collecting venules
V3	Post-capillary venules

ACKNOWLEDGMENTS

The past few years were the most challenging yet deeply rewarding chapter of my life. I could not have done it without the network of inspiring and supportive people that I'm lucky to have in my life.

I want to start by thanking my supervisors, **Dr. Lehmann** and **Dr. Chappe** for their mentorship, intellectual nurturing, and unconditional support. You believed in me and gave me everything that I could have asked for in mentors. Thank you for helping me develop into a better person, both inside and outside of the lab.

I also want to extend my gratitude to my Supervisory Committee members, **Dr. Younes Anini, Dr. David Hoskin,** and **Dr. Alex Quinn,** for their expertise, helpful feedback, and encouragement throughout my degree. Thank you, **Dr. Juan Zhou**, for your invaluable surgical and research skills teachings. **Tanya Myers**, I knew I could come to you with any questions that I had; you are a well of knowledge! Thank you, **Dr. Bruce Holbein**, for sharing your expertise and providing me with insight for furthering my research. I have sincere appreciation for **Audrey Li** and **Patricia Colp** for their immense technical help and warm support.

Dr. Marie-Soleil Beaudoin, Dr. Cindy Penney, Dr. Elizabeth Cowley (Physiology & Biophysics), **Haitham Fathalla** and **Dianne Cox** (Collage of Pharmacy) thank you for providing me with the opportunity to practice knowledge translation through teaching. You trusted me to take on the role and I am forever grateful for sharing your teaching passion with me.

I am also thankful for my lab mates who supported me and gave me many colourful and cherishable memories. **Dr. Yan Burkovskiy**, right from the first day that I joined the lab, you have been providing me with advice and kind mentorship in all aspects of research. **Dr. Danielle Fokam**, we began as colleagues and now, you're one of the dearest people to me. Your dedication, work ethic, and kindness inspire me every day. **Kayle Dickson**, watching your grow from the day we met to where you are right now, makes me so proud of you. It warms my heart and gives me bright hope about the future generation of scientists. **Anna Semaniakou**, you have been with me through every step of this journey and words cannot express my gratitude for the love and support you have provided me. To the rest of **the wonderful lab members** who have left a great impression on me including Taylor (whom I started the journey with), Alexa (whom I worked with closely for CF research), Geraint, Casiddy, Bashir, Kiyana, Nazli, Saki, Mariane, Sophie, Anu, Sophie, Sarah, George, Robert, and Angel, thank you for all the joy you brought to my life.

The supportive environment was also available to me outside of my supervisory labs. **Dr. Wasundara Fernando** and **Javad Ghassemi Rad**, when I was out of my comfort zone, you made me feel at home in the Hoskin Lab. You were so patient as you taught me the experimental procedures. And I always looked forward to our delightful conversations, whether they were about movies, the moon, or experiments not working, you put a smile on my face. **Faculty of Medicine Graduate Student Society (FMGSS)**, thank you for becoming my second family. You provided me with a safe place to talk, to laugh, and to have useful discussions about science and future career. To the rest of my support circle and friends, you know who you are. I am grateful for having each one of you in my life. I don't know how I could have gone through this chapter without all of your help and support.

I would not have started my research path if it were not for **Dr. Liliana Portales** and **Dr. Jean Marshall**, who believed in me and provided me with my first research experience as an honours student. It was the passion, determination, and research joy which I saw in you that inspired me to continue this path.

I want to thank the **Izaak Walton Killam Predoctoral Scholarship** for funding and supporting my doctoral education. Additionally, I want to thank **Chelation Partners Inc**. for providing DIBI and making this research possible.

And finally, I want to acknowledge the mice that dedicated their lives to science and made this essential research feasible.

CHAPTER 1: INTRODUCTION

Iron is by mass the most abundant element on earth (1). Therefore, it is not surprising to find the element in so many organisms and its importance in health is well established. Impaired iron levels can lead to serious clinical syndromes and diseases: low iron levels can cause anemia, while high iron levels cause hemochromatosis and systemic toxicity. This thesis focused on the complex role that iron plays in inflammation and infection. In particular, iron catalyzes the production of reactive oxygen species (ROS), which is an important mediator in inflammation and contributor to the elimination of pathogens. However, excess iron and ROS availability leads to oxidative stress, harming the host tissues and organs. Also, pathogens including bacteria utilize iron too. Therefore, endogenous (within the organism) or exogenous (by iron chelator treatment) iron restriction can decrease infection severity. The goal of this research was to study the role of iron in experimental models of inflammation and infection through iron chelation.

1.1 Physiological role of iron

Iron is required by most forms of life for both health and survival. Iron's most common oxidation forms are Fe^{2+} (Ferrous) and Fe^{3+} (Ferric). On average, the human body contains 3-4 g of iron (2). Iron levels are tightly regulated by dietary absorption and efficient recycling of iron from senescent red blood cells (RBC). Iron's redox properties enable it to participate as co-factor in many biological reactions. Through the mitochondrial electron transport chain, iron-sulfur clusters play a critical role in generation of ATP. Iron is also utilized for synthesis of DNA, proteins, and receptors involved in intracellular signaling (3). Additionally, iron held in the center of a porphyrin ring forms the heme prosthetic group that is important in the function of many structural proteins and enzymes. Of these proteins, hemoglobin and myoglobin rely on this heme group to carry oxygen to tissues, organs and muscles. Moreover, the cytochrome P450 family of enzymes, located mainly in the mitochondria and the endoplasmic reticulum, conduct their metabolic function using heme as a co-factor.

Iron levels are maintained through absorption regulation without an active excretion pathway. Upon food digestion in the stomach, chyme passes into the small intestine for nutrient absorption at the duodenum and upper jejunum. Most of the dietary iron is found in ferric form and must first be converted to the ferrous form at the brush border (Figure 1). This redox reaction is carried out by the ferrireductase duodenal cytochrome B (DCYTB), which is found at the apical membrane of the enterocytes. Ferrous iron is then absorbed through a co-transporter channel named divalent metal-ion transporter-1 (DMT-1), also known as heme carrier protein-1, which is located on the apical side of enterocytes. DMT-1 is the first mammalian transmembrane iron transporter to be discovered (4). Once absorbed from the intestinal lumen, "free" labile iron binds to an iron-regulatory protein to form a stable complex. This is a protective step as unbound iron can generate toxic radicals and damages healthy tissues and organs.

Once inside the enterocyte cytoplasm, iron can either be stored within iron stores called ferritin (in the case of high plasma iron) or leave the cell for absorption into systemic circulation. This absorbed iron is incorporated into ferritin with the help of metallochaperones of the poly(rC)-binding protein (PCBP): PCBP1 and PCBP2 (5). Iron stored in enterocytes is considered lost as these cells have a high turnover (3-4 days) and aged enterocytes will be sloughed off and excreted in stool. Typically, 1-2 mg of iron is lost through this process and thus requires that a similar amount of iron is acquired from the diet. Interestingly, it has been observed that there is a positive correlation of fecal and serum ferritin with dietary bioavailability in humans (6, 7). Ferrous iron, however, travels to the basolateral side of the enterocyte with the help of chaperone proteins for absorption into the bloodstream. Iron leaves the cell through ferroportin, also known as iron-regulated transporter 1. Ferroportin is integral to iron export as its inactivation and deficiency lead to intracellular iron accumulation and anemia (8). Once in the blood, ferrous iron undergoes redox reaction by copper-dependent ferroxidase called hephaestin to become ferric. Ferric iron then binds to the protein carrier, apo-transferrin, which then matures into transferrin and creates a non-labile and non-reactive complex. Cells from various organs can acquire iron from transferrin. The fate of iron from here depends on the metabolic needs (Figure 2).

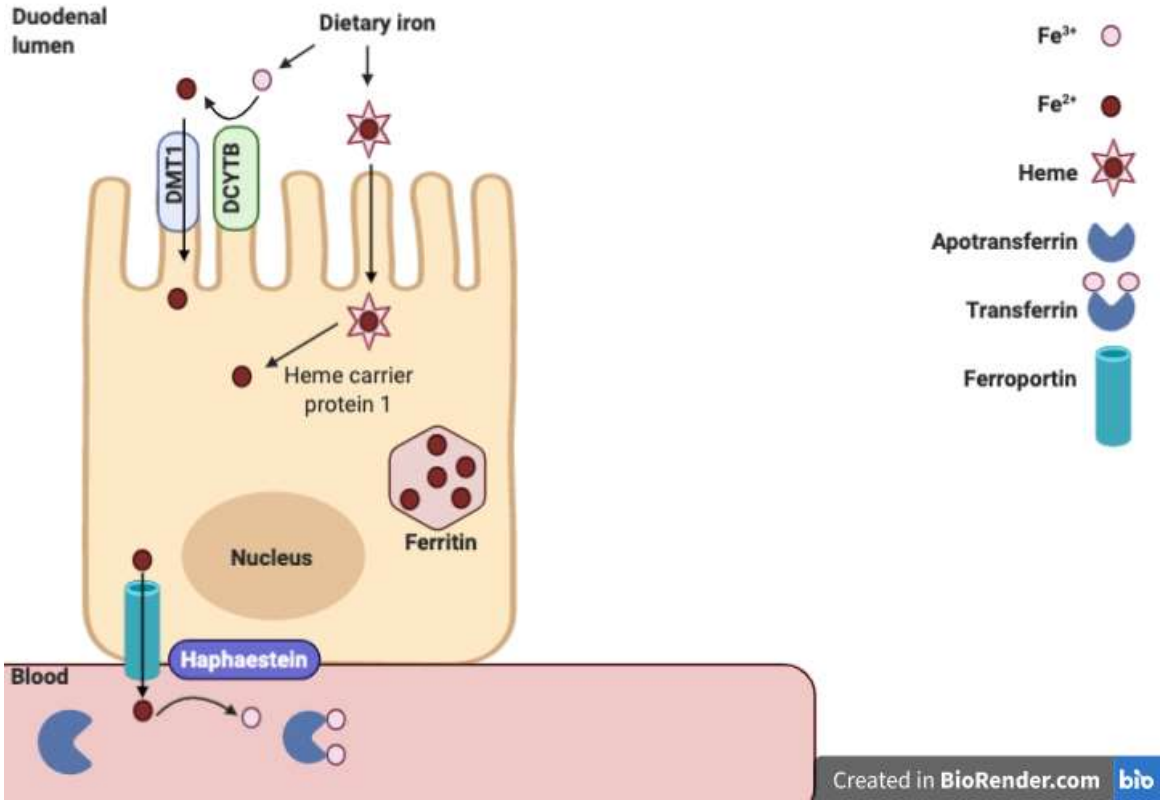

Figure 1. Cellular iron metabolism within enterocytes.

Dietary iron arrives in the intestine as heme ferric iron (Fe^{2+}) and non-heme ferrous iron (Fe^{3+}). Heme iron can be directly absorbed into the enterocytes and iron is released with the help of Heme carrier protein 1 into the cytosol. Ferrous iron is reduced by DCYTB and is then taken up into the cell by DMT1. Once inside the cell, iron can be stored within ferritin or be transported to the basolateral side for absorption into systemic circulation. Once near the basolateral compartment, iron passes through ferroportin and is oxidized to ferrous form by haphaestin. Ferrous iron is transported through blood and the rest of the body by transferrin. Abbreviations: DCYTB= Duodenal cytochrome B; DMT1= Divalent metal ion transporter 1; Fe= iron.

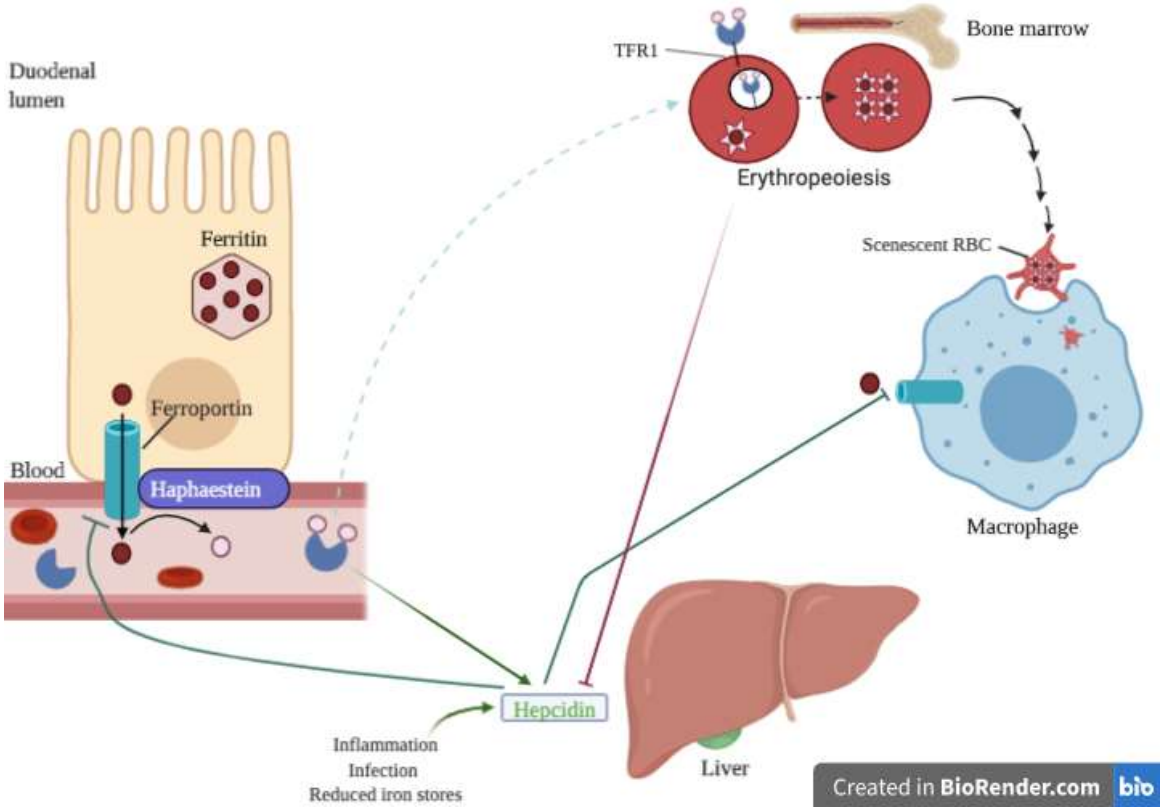

Figure 2. Fate of iron after intestinal absorption.

Once iron is bound to transferrin in the blood, it can be delivered to various organs for their iron needs. Most of the transferrin-bound iron is transported to bone marrow where the process of RBC maturation, erythropoiesis, takes place. Transferrin is internalized by RBCs after binding to Transferrin receptor 1 (TFR1). Upon iron removal from transferrin, it gets incorporated into the heme of hemoglobin of the newly synthesised RBC. Once RBCs have aged in circulation, they will enter the reticuloendothelial system to be phagocytosed by macrophages. The iron from heme is recycled and enters the circulation via ferroportin exporter. In addition to liver receiving iron for its use, the liver plays an important role in systemic iron regulation by producing hepcidin. Hepcidin blocks ferroportin exporter activity and induces its internalization to reduce iron absorption. Hepcidin release is inhibited with higher iron requirements such as by erythropoiesis. Its release is promoted by inflammatory mediators such as IL-6, pathogenic molecules, reduced iron storage, and high plasma transferrin levels.

One of iron's essential roles is the delivery of oxygen through the blood by hemoglobin and oxygen storage within muscles by myoglobin. Since RBCs have a heme complex, they have high iron requirement to perform hemoglobin production. During this process, iron is utilized for the maturation of erythrocyte progenitor cells in to mature RBCs, which enter the circulation. To ensure access to iron for their high iron needs, erythrocyte progenitor cells express 80 % of the transferrin receptors that are present in the body (9). Upon binding of transferrin to its receptor, it is taken into the RBCs via clathrin-mediated endocytosis (10). After the fusion/merging of a lysosome with this endosome and the acidification of the environment, the iron is released, and the transferrin proteins returns back into the circulation. This iron is reduced to Fe^{2+} by the six-transmembrane epithelial antigen of the prostate 3 (STEAP3) and enters the cytosol via DMT-1. This iron is utilized mainly in the mitochondria for heme synthesis. Once mature, these RBCs will leave the bone marrow and enter the blood stream to fulfil their role of oxygen carriage.

Once these RBCs age, they are cleared from circulation and are eliminated by macrophages within the reticuloendothelial system (also known as mononuclear phagocyte system). Macrophages residing in the liver, spleen, and bone marrow engulf the senescent RBCs. Within the phagolysosome, hydrolytic enzymes break down the hemoglobin into globin chains, iron, and a porphyrin ring (from heme which is converted to bilirubin). To minimize iron loss, 90 % of this iron is recycled internally (10), the majority of which is released back into the systemic pool (iron bound to transferrin) via ferroportin channel. Ceruloplasmin, a homologue of hephaestin, conducts iron oxidation reaction for the iron to bind onto transferrin. Alternatively, some of the recycled iron is stored in ferritin and hemosiderin iron stores, the latter being poorly available for utilization and formed only during excess local or systemic iron levels.

The liver is an important organ in iron homeostasis. Iron is delivered to the liver via the hepatic vessel where hepatocytes absorb transferrin-bound iron through their transferrin receptors (11). Similar to RBCs, the iron is released within endolysosome and transferrin is recycled back into circulation while ferritin and hemosiderin act as storage reservoirs. If needed, iron can go back into the circulation through the ferroportin mechanism. In addition

to these cellular metabolisms of iron through storage, the liver plays an important role in systemic regulation of iron. Hepatocytes predominantly produce the peptide hormone hepcidin, coined the master iron regulator, due to its ability to inhibit iron absorption (11). Hepcidin induces the internalization and degradation of ferroportin. Thus, hepcidin prevents iron efflux and ultimately decreases plasma iron concentrations.

Hepcidin impacts iron absorption in all cells expressing ferroportin, including macrophages, enterocytes, and hepatocytes (12–14). Upon hepcidin release, iron absorption is at a halt, resulting in iron retention within cellular iron stores and tissue (2). Hepcidin release is inhibited when there is a demand for iron such as during erythropoietic activity in the bone marrow. In contrast, hepcidin production is stimulated when there is an acute increase in transferrin saturation (supplements), increase in transferrin-bound iron/high plasma iron levels, presence of inflammatory mediators such as interleukin (IL-) 6 and tumor necrosis factor alpha (TNF-α), or microbial components (15).

Any disruptions to the above described homeostasis pathways can result in diseases. The main regulator of hepcidin is the human factors engineering (HFE) gene. Disruption of the HFE gene can lead to a downstream dysfunctional HFE protein. Hereditary hemochromatosis is the most common autosomal recessive disorder in the Caucasian population. The genetic mutation, commonly a C282Y polymorphism in the HFE gene, causes excessive iron absorption and release into the body (16). Because of the lack of an effective excretory mechanism, patients with hemochromatosis accumulate iron. This iron overload is toxic and can lead to organ dysfunction and death if not treated (17). Systemic iron levels are changed during inflammation and these levels are associated with inflammatory disorders. To understand this association, first the basic mechanisms of inflammation will be reviewed.

1.2 Role of iron in inflammation

1.2.1 Basic mechanisms of inflammation

Inflammation has evolved as a mechanism to protect organisms from harmful stimuli, minimize damage and initiate healing. The typical clinical signs of an ongoing inflammatory response are heat, redness, swelling, pain and loss of function which are based on activation of distinct pathophysiological processes. The immune system uses physical, chemical, and cellular components to orchestrate a highly regulated response between the immune, vascular, neurological, and coagulation system to restore homeostasis. The goal is to eliminate the threat and initiate the healing response by having the appropriate magnitude of response; an inadequate response can be ineffective, while an excessive response can be detrimental to the host (18).

The immune response is carried out by two consecutive systems: the innate and adaptive systems. The innate system generates an early generic cellular response (within minutes to hours). This response is critical, not only because it enables an early intervention for defence, but also because it initiates adaptive immunity. The adaptive immune system produces antigen-driven and specific humoral and cellular responses. These responses normally last only a few days. However, in the case of chronic inflammation and auto-immune diseases, the unresolved adaptive immune response can last for months. Adaptive immunity develops the tools and memory for protection against future attacks. It is integral that innate, adaptive, and non-immune cells communicate together to coordinate an effective and regulated response (19).

The inflammatory response can be triggered by sterile events or an infection. Sterile danger signals such as host damaged cell components (extra-nuclear DNA), heat shock proteins, metabolites, uric acid, and ATP are referred to as damage associated molecular patterns (DAMPs). DAMPs can drive the pathology in numerous inflammatory syndromes and diseases including autoimmune disease, ischemia, and systemic inflammatory response syndrome. If the inflammatory components are infectious in origin such as lipopolysaccharides (LPS) or peptidoglycans (bacteria), capsid proteins (virus), zymosans

(fungi), or glycophosphatidylinositols (protozoans), then they are referred to as pathogen associated molecular patters (PAMPs). During an infection, these PAMPs are found in areas that are generally sterile such as the blood stream, urinary tract, brain, and within enterocytes (20).

The resident and structural cells, such as airway epithelial cells, tissue-resident macrophages, and endothelial cells, are the first cells to detect those threats. These cells express innate immune receptors called pattern recognition receptors (PRR), that once activated are able to trigger a generic response towards the harmful stimuli. PRRs are present on the cell surface and within immune and structural cells (21). Upon binding of ligand to PRR, signaling cascades are rapidly activated which lead to initiation of the inflammatory response. The most extensively studied of the PRRs are the toll-like receptors (TLRs). There are 13 different mammalian TLRs discovered with 10 members (TLRs 1-10) expressed in humans (22). Upon binding of DAMPs and PAMPS to their respective receptors, the receptors dimerize and cytosolic adaptors (such as MYD88 and TRIF) are recruited to conduct downstream signaling. This activates nuclear factors which translocate into the nucleus to (up/down-) regulate the expression of inflammatory mediators. The classical nuclear factor in inflammatory signal transduction is nuclear factor kappa B (NF-κB). NF-κB activation induces the transcription of pro-inflammatory cytokines, chemokines, and other antimicrobial peptides. The signaling cascade can give rise to important players of the immune system. Such players include cytokine and pro-inflammatory mediators. These pathways can be activated experimentally as a model of inflammation through the administration of PAMPs such as LPS. Typically, this induces the expression of acute phase proteins and their gene expression which includes pro-inflammatory mediators such as IL-6, IL-1β, TNF-α, IFN-γ.

As a result of the intracellular signaling cascade, TNF-α and IL-1 are released by both immune and non-immune cells. These two inflammatory mediators induce fever, further cytokine production, and leukocyte chemotaxis. Upon activation of mast cells and basophils in inflammation, through antigen crosslinking complexes (IgE and Fc receptor), they release large amounts of histamine and bradykinin which increase vascular

permeability and result in vasodilation. Activated endothelium and macrophages release nitric oxide (NO), further inducing vasodilation. This increase in vessel permeability and blood perfusion (resulting in redness and heat), enables the influx of plasma proteins, antimicrobials, immunoglobulins, complement factors, and other inflammatory mediators into site of injury. Fluid leakage into tissue causes the edema and swelling. Neurological mediators that rush into the injured site contribute to the pain that is associated with inflammation (23). Activated endothelial cells increase their surface adhesion molecule expression for leukocyte adherence and extravasation (Figure 3). Cells, including macrophages and endothelial cells, will release IL-8 for neutrophils to migrate to the inflammation site.

Neutrophils are the most abundant type of leukocyte in the blood, and they are the first cells to arrive at the site of inflammation through chemotaxis. Since their main function is to defend the immune system, they have multiple mechanisms to eliminate sources of danger: phagocytosis of potentially harmful agents, releasing potent granular components, and creating neutrophil extracellular traps (NETs). Within the phagosome, they can produce reactive species as part of their antimicrobial defence (which will be expanded upon later).

The adaptive immune response is initiated when antigen presenting cells (macrophages, dendritic cells, or B cells) present the engulfed DAMPs and PAMPs on their cell surface MHC molecules to T cells. Upon interaction of the T cell receptor and the antigen, T cells proliferate and differentiate into various T cell subsets. One of their important functions is to activate B cells so they can initiate antibody development. Antibodies will bind to the specific antigen and induce antimicrobial effects: they can activate the complement system, neutralize the PAMPs by surrounding it, and opsonize PAMPs for phagocytosis. These antibodies can orchestrate an antigen-specific response and provide a faster response upon secondary exposure to the same antigen.

The immune responses, both innate and adaptive, enable the shift from the initial pro-inflammatory phase to an anti-inflammatory, pro-healing and resolution phase. The pro-inflammatory mediators are replaced with the recruitment of anti-inflammatory and

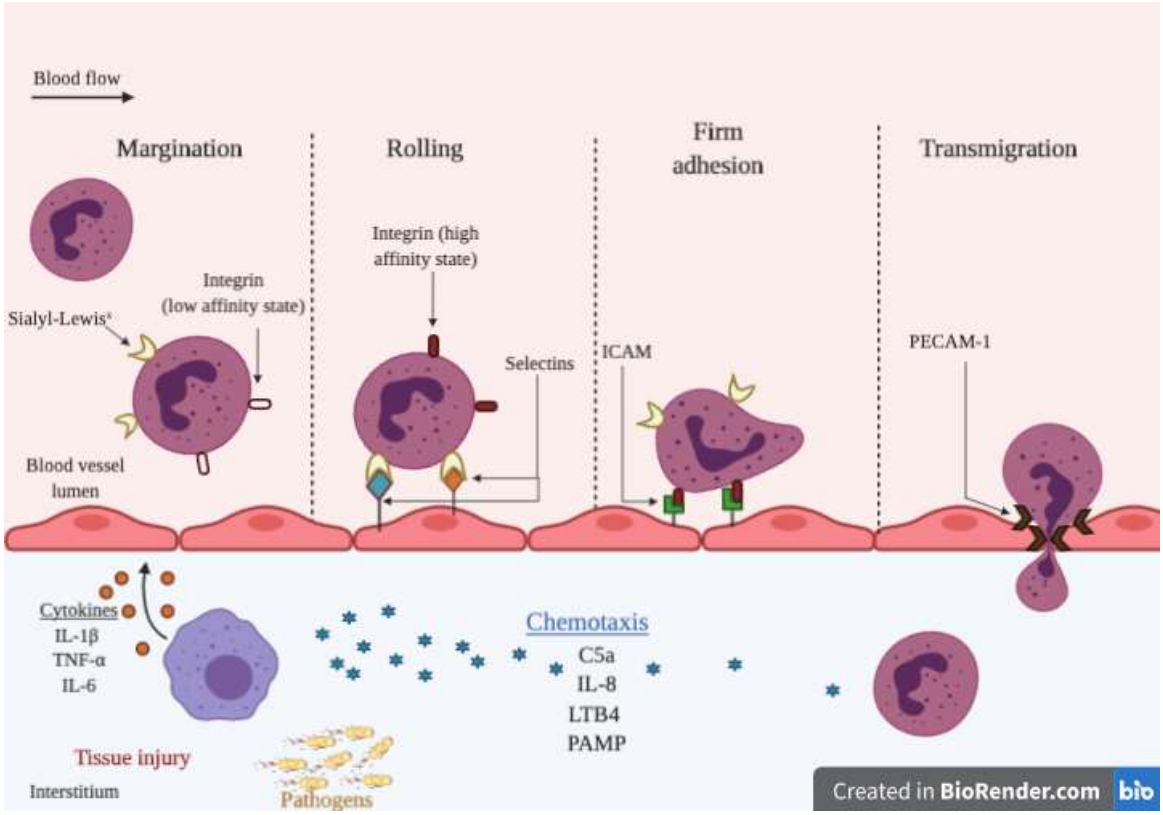

Figure 3. Leukocyte extravasation.

A simplified schematic representing leukocyte extravasation, migration of leukocytes from systemic circulation towards the site of inflammation (injury or infection site). Upon inflammatory stimulus, the free-flowing leukocytes become primed and slow down. Leukocytes tether to selectins on endothelial cells which causes them to tumble slowly across the endothelium (Rolling). Next, tight binding is initiated as integrins on the leukocytes bind to ICAM-1 expressed on endothelium (Firm adhesion). Leukocytes continue to flatten and strengthen their adhesion through integrin clusters and tyrosine phosphorylation signalling. As a final step on the lumen side, the leukocytes cross into the interstitial space/basement membrane either paracellular or transcellularly (Transmigration). The leukocyte then migrates to the site of inflammation via chemotaxis, chemical gradient composed of inflammatory chemokines and proteins such as IL-8, C5a, or pathogen associated molecular patterns (PAMPs).

pro-resolving mediators such as prostaglandins, IL-10, and glucocorticoids as the sources of inflammation are eliminated. This shift is an integral step in the resolution of inflammation as failure to switch to an anti-inflammatory state can lead to chronic inflammation. This highlights the importance of an adequate inflammatory response as an insufficient and non-effective response can lead to recurrent infections, prolonged oxidative stress, fibrosis, and development of auto-immune disorders. On the other hand, hyperactivation of the immune system can lead to consequential damage of healthy host tissues. As iron plays a pivotal role in immune defence, its role in the inflammatory process will be explored further.

1.2.2 Iron and inflammation

As discussed earlier, iron's redox properties make it a co-factor in many physiological processes. By transferring electrons, it can catalyze product and bond formation. One important set of reactions are the Fenton and Haber-Weiss reactions. During this reaction, iron catalyzes hydroxyl radical ($OH^{\bullet}$) formation from hydrogen peroxide (H_2O_2) and superoxide anion (O_2^-). Hydroxyl and superoxide radicals are highly reactive as they have an unpaired electron in their outermost shell. Hydroxyl and superoxide, collectively referred to as ROS, can break carbohydrate bonds, cause lipid peroxidation, oxidize proteins, and damage nucleic acid (DNA and RNA). They lead to the generation of additional radicals and oxidants. A superoxide anion generates reactive nitrogen species (RNS) as it reacts with NO. Nitric oxide synthase (NOS) catalyzes this reaction to generate peroxynitrite ($ONOO^-$), a potent oxidant. ROS and RNS are considered dangerous as they can create even more reactive hydroxyl radicals. Since they do not discriminate against the host, they can damage healthy bystander tissues and organs if their levels increase. As free, labile iron serves as a catalyst, it is important to regulate iron levels tightly. And therefore, ROS and RNS levels can be reduced by iron restriction.

In homeostasis, low levels of these ROS are produced as byproducts of aerobic respiration. The iron-sulfur clusters in mitochondria and aids the electron transport chain (ETC) and ATP production. Due to the rapid redox reactions, sometimes the reduction step does not go to completion, so the oxidative phosphorylation step produces radicals (superoxide

anion). If their levels increase, these ROS can damage the mitochondrial DNA, matrix, and potentially leak into the cytosol (24). ROS are also produced within peroxisomes and the multi-enzyme microsomal monooxygenase system as part of metabolism and drug detoxification (25,26).

ROS play a role in the regulation of inflammation and defence mechanisms independent of pathogen-activation. Within the immune system, ROS are produced in the phagocytic cells as they perform an oxidative burst, sometimes called a respiratory burst. Once PAMPs are internalized, nicotinamide adenine dinucleotide phosphate (NADPH) oxidase translocates from the cytosol to the phagosome to produce ROS (27). RNS are also produced within the phagosome by inducible NOS (iNOS). ROS, as messengers, initiate the inflammatory response and subsequent downstream events such as cell differentiation and up regulation of phagocytic activity. ROS production is critical as low ROS levels have been shown to reduce the phagocytic activity and oxidative bursts of immune cells (28). Immune and non-immune cells generate ROS as means of communication and signaling since ROS can act as messengers. Their small size enables them to work locally and at peripheral targets allowing them to act as first and secondary messengers in immune signaling, apoptosis, or cell differentiation (29).

Additionally, ROS induce calcium influx within a variety of immune cells, via local TRPM2 activation. This induces the nuclear translocation of redox-sensitive transcription factors including NF-κB and results in transcription of their inflammatory genes (30). This TRPM2-mediated calcium influx and ROS generation is associated with NLRP3 inflammasome assembly, where the inflammasome is a pro-inflammatory complex made of cytosolic proteins in response to stress and infectious triggers (31). Furthermore, ROS regulate the life cycle and behavioral profile of macrophages. NADPH oxidase is essential for monocyte differentiation to macrophages (32). ROS is also essential for the polarization of macrophages which are generally classified as having an M1 or M2 phenotype. M1 macrophages are classically activated by IFN-γ and TLR ligands and are pro-inflammatory. They produce large amount of ROS and RNS through oxidative burst, engulf and present antigens, and activate T cells as part of their powerful antimicrobial response (33). M2

macrophages, alternatively activated by IL-4 and IL-13, are anti-inflammatory and aid in tissue repair and remodeling. Higher ROS levels have been shown to promote an M2 polarization, while RS scavengers can inhibit this polarization (34, 35). Though the complex mechanism(s) are not well understood, it is evident that ROS plays an instrumental role in polarization of macrophages, and thus aids in potentiating an appropriate cellular response.

Since ROS do not discriminate against the host, compensatory antioxidant mechanisms are in place to protect against their damage and balance the levels of ROS. There are a series of enzymatic and non-enzymatic antioxidants spread all over the body. For example, catalase and peroxisomes break down hydrogen peroxide, glutathione neutralizes (reduces) reactive species, and superoxide dismutase catalyzes the metabolism of superoxide (36, 37). When the levels of ROS overwhelm the antioxidant system, the benefit of eliminating pathogens is outweighed by their damage, which leads to oxidative stress. Iron catalyzes ROS formation, thus modulating iron absorption is one way to stop the vicious cycle and positive feedback loop of ROS production. To lower oxidative stress, hepcidin is released and subsequently, iron absorption is inhibited. During inflammation, inflammatory mediators stimulate hepcidin release and in few hours, systemic iron levels are reduced. This is referred to as the hypoferremic response. This is a protective mechanism that has evolved to limit iron's bioavailability to pathogens in the face of inflammation and infection. A prolonged hypoferremic response, typical of chronic inflammation, lowers iron levels in the circulation and leads to iron deficiency known as anemia of inflammation (AI). AI, sometimes referred to as anemia of chronic disease, is the second most prevalent form of anemia and the most common in hospitalized, and chronically ill patients (38). As explained, the source of this deficiency lies in the inhibition of ferroprotein function. This long-term iron restriction has consequences such as reducing erythropoiesis (10).

Depending on the magnitude and duration of inflammation, we can see patterns and changes of iron storage. These changes to iron levels and their storage pattern are implicated in several chronic pathologies where oxidative stress contributes to host tissue and organ damage. This change is also observed in inflammatory pathologies such as auto-

immune diseases (e.g. rheumatoid arthritis), neurodegenerative diseases (e.g. Alzheimer's), ischemia, interstitial cystitis, and infections (e.g. sepsis and cystic fibrosis) (39–45). Changes to iron levels can be harmful or beneficial depending on the health status of the person. In infection, however, lower levels of iron are preferred as microbes utilize iron for their reproduction and growth. Given this dual role of iron in the host's inflammatory response, the role of iron in infection will be discussed next.

1.3 Role of iron in infection

The biological requirement for iron is conserved amongst all forms of life including bacteria and fungi. Traditionally, these microorganisms were viewed in the lens of being solely in a parasitic relationship with the host. However, technological advancements have provided us with a better understanding of our co-existence with the microbial community, referred to as the microbiota. For example, the development of next generation sequencing of 16S rRNA has helped identify the presence of 2,000 bacterial genomes per cm^2 surface in the lower respiratory tract, previously-thought to be a sterile anatomical site (46, 47).

The symbiotic relationship between host and microbial species can be either commensal, mutualistic, or parasitic. In a commensal relationship, the microorganism benefits while the host is not affected whereas in a mutualistic relationship, both the host and the microorganism benefit. In a healthy individual, the microbiota consists of both commensal and mutualistic relationships between the microorganisms. Antimicrobial byproducts such as pseudomonic acid A (also known as Mupirocin) from *Pseudomonas aeruginosa*, an opportunistic pathogen in the skin microbiota, protect us from *Staphylococcal* and *Streptococcal* infections (48). Additionally, *P. aeruginosa* co-exists with fungal species while suppressing their growth on our skin (49,50). The intestinal microbiota, including *E.coli* species, protects us from virulent pathogens by inhibiting colonization, producing antimicrobial peptides, and competing for nutrients (51). Furthermore, they produce nutrients such as vitamin K and short-chain fatty acids (52). The third kind of relationship, parasitism, is traditionally viewed as an infection, where the microorganisms benefits at the cost of harming the host. Usually this involves the more virulent pathogens and initiates inflammation. However, the diversity and size of the microbiota, location of colonization,

previous exposure, environment, age and immune status of the host are all important players in creating this dynamic relationship (53).

During infection, iron plays a dual role: on one hand it is required by the host to produce ROS, and on the other hand it is utilized by the microorganisms for survival and pathogenicity. This creates competition within leukocytes and microorganism populations, as well between them, for iron. Upon activation of leukocytes by PAMPs, leukocytes employ various antimicrobial mechanisms including iron-dependent ROS production (e.g. hydrogen peroxide and hypochlorous acid (39) through oxidative bursts to degrade invading pathogens thus limiting their spread. When oxidative burst mechanisms are impaired, such as in chronic granulomatous disease, patients suffer from ineffective pathogen clearance, resulting in recurring bacterial and fungal infections (55). Additionally, this ROS impairment decreases the cross-presentation of antigens to CD8+ T cells, a step that is critical in regulating the adaptive immune response (56).

Pro-inflammatory mediators such as IL-6 induce the release of hepcidin antimicrobial hormone which promotes intracellular iron retention. This response, known as hypoferremia, is a well-known example of nutritional immunity, which occurs as an attempt to starve the bacteria (57). To facilitate this response, innate immune proteins lactoferrin and lipocalin 2 (siderocalin), bind to iron with high affinity and interfere with pathogenic iron uptake at the infection site (58,59). This also contributes to selective pressure amongst different microbial species to develop more competitive iron acquisition mechanisms.

Microorganisms, particularly bacteria, have developed complex and diverse acquisitions mechanisms to gain an advantage in the battle for iron. Presence of iron allows bacterial proliferation while iron scarcity inhibits their growth (60–62). Iron deficiency induces a stress response on bacteria which triggers the activation of mechanisms including siderophore release (endogenous and exogenous microbial iron chelators), and iron uptake systems from heme, ferrous and host iron-binding proteins. Gram negative bacteria, including *E. coli* within the gut microbiota, release enterobactin which chelates ferric iron

(63). The highly adaptive *P. aeruginosa* releases extracellular siderophore pyoverdine (high iron affinity) and pyochelin (energy efficient) into the environment (64). It can also uptake xenosiderophores such as enterobactin via two different receptors, PfeA and PirA (65). *Yersinia pestis*, the causative agent in the Black Death plague, utilizes its potent iron chelator yersiniabactin to "steal" iron from host lactoferrin resulting in reduced iron availability for innate defence within the host (66). *Neisseria meningitidis*, the bacteria responsible for meningitis and meningococcemia competes for iron with host-iron binding proteins hemoglobin, transferrin, and lactoferrin (67,68). Altogether, this evidence highlights iron's requirement for bacterial physiology and pathogenicity. Two well-known examples of oxidative stress contributing to pathophysiology of medical conditions are sepsis and cystic fibrosis (CF).

1.3.1. Sepsis

Sepsis is a life-threatening clinical syndrome where dysregulated host response leads to organ dysfunction during infection (69). The dysregulation of the systemic immune response, ranging from hyperactivation to immunosuppression, is emphasized as the cause of its pathophysiology. Sepsis has a high hospital mortality of >10 % and even as high as >40 % during its more severe form, septic shock (69). Given the challenges around diagnosis and treatment of sepsis, the impact of this syndrome is under-documented. A recent analysis estimated that there were 48.9 millions of cases globally with a mortality rate of 19.7 % in 2017 (70). Sepsis remains as the main cause of death in surgical intensive care units of hospitals (71). The global financial burden of sepsis on the healthcare system is high; in the US alone, sepsis-induced healthcare costs reach >$24 billion annually (72). This includes the long-term care and rehabilitation services that are needed for the chronic consequences present after leaving the hospital. Although everyone is susceptible to sepsis, factors such as comorbidities (i.e. hypertension, auto-immune diseases, and chronic renal failure), age, sex, socio-demographic index, and immune status increase the risk of acquiring sepsis (70, 73–75).

The most common sites of infection in sepsis are the lower respiratory tract, bloodstream, abdomen, and urinary tract (76, 77). Sepsis can present itself as a heterogenous set of

symptoms as it depends on the unique interaction between the pathogen and, most importantly, the host's response. Given the rapid progression of this life-threatening condition, timely diagnosis and treatment are key. As a way to screen for sepsis, a new tool the named sequential (sepsis-related) organ failure assessment (SOFA) score was developed. Although not entirely sepsis-specific, the score is a more comprehensive set of tests that can predict the likelihood of organ failure, sepsis, or septic shock development (78,79). It includes consideration of respiratory, coagulation, cardiovascular, central nervous system, and renal factors. The criteria for sepsis include suspected or documented infection, and a rapid increase in 2 or more SOFA points. Unfortunately, these tests can be time consuming and given the rapid progression of sepsis, faster testing tools are more effective at improving outcome. That is why the quick SOFA (qSOFA) tool was developed which can be used for screening at bed side. It includes altered mental status, systolic blood pressure of <100 mm Hg, and respiratory rate >22 breaths per min.

The complex pathophysiology of sepsis can be characterized by phases of hyperactivated, pro-inflammatory state (often in the beginning of the disease) and an immunocompromised state (often in late sepsis). It is important to note the co-existence of both pro- and anti-inflammatory mediators during this immune dysregulation. The hyperactivation state begins with the innate immune response; immune (macrophages, monocytes, neutrophils cells) and non-immune cells (endothelial and airway epithelial cells) detect the presence of PAMPs (such as endotoxin) and DAMPs (damaged cellular particles) by PRR. This triggers the release of pro-inflammatory mediators including cytokines (IL-1β, IL-6, TNF-α), histamine, caspases, and chemokines. These mediators will recruit leukocytes to the site of inflammation, upregulate endothelial adhesion molecules, and activate the immunovascular, coagulation, and complement systems. Since the immune response is dysregulated, there is an excess of these mediators, leading to a cytokine storm (80). ROS can increase this inflammation by further activating NF-κB pathways, creating more DAMPs through oxidative damage, thus sustaining the positive feedback loop of inflammation (81).

Coagulatory pathways are activated in parallel with inflammatory pathways (82). Platelets form blood clots to stop bleeding and minimize damage. In sepsis, this system is also dysregulated where hypercoagubility is present, potentially escalating to fatal disseminated intravascular coagulation (DIC). This is caused by multiple factors in the clotting process. There is an increase in platelet tissue factor (also known as factor III) release from endothelial cells and leukocytes, which initiates thrombin formation (83,84). Tissue factors are essential in this inflammation-induced thrombin formation, the downstream platelet activation and fibrin clot formation which can create local (micro-) hypoxia. In sepsis, the anti-coagulatory cascade is impaired as anti-coagulants protein C, protein S, and thrombomodulin are downregulated (82). Interestingly, proteins C and S are also shown to have anti-inflammatory properties by limiting leukocyte adhesion and inhibition of TNF-α, IL-1β, and IL-6 (85). Additionally, the breakdown of fibrin clot, known as fibrinolysis, is also reduced (86). Together, these changes lead to microvascular thrombosis.

ROS and other reactive species released by leukocytes and non-immune cells modulate the vasculature system by promoting vasodilation and hypotension. Furthermore, leukocytes release inflammatory mediators such as TNF-α, IFN-γ, and IL-1β which promote NO synthesis by inducible nitric oxide synthase (iNOS). In regulated inflammation, this is an adaptive response to increase blood flow to the site of inflammation and facilitate leukocyte recruitment. However, in sepsis iNOS is hyperactivated, through degradation of cytoplasmic IKB and subsequent P65 translocation to the nucleus, leading to excess NO production, resulting in hypotension and vasodilation (87, 88).

This vasodilation compromises the structural integrity, impacting barrier function, and permeability of the endothelial cells. Together with the oxidative stress, the glycocalyx protective layer is damaged, which affects the cellular junctions (alteration to cadherin and tight junctions) (89). Fluid leakage into the interstitial space and tissue edema can have major systemic consequences. Within the gastrointestinal system, the mucosal lining is critical as the intestine is home to millions of microbes including gut microbiota. If this barrier is disrupted, microorganisms can translocate, activate the immune system, and even enter the bloodstream (causing a “second hit” of sepsis). Additionally, there can be damages

induced by digestive enzymes that leave the lumen. Within the respiratory system, this can impact the alveolar-endothelial barrier, leading to fluid leakage into the alveoli, reduced alveoli oxygen saturation, and the induction of acute respiratory distress syndrome (ARDS). ARDS is associated with hospital mortality of patients with sepsis, independently from the overall severity of the illness (90). Many other organs are susceptible to barrier disruptions such as the brain (septic encephalopathy), and the kidneys (acute kidney injury). Together, vasodilation, edema, and capillary leakage cause blood shunting and reduced oxygen delivery to some tissues and organs.

Given that oxygen delivery is critical, hemodynamic factors such as mean arterial pressure and cardiac output are targeted for improving systemic oxygenation. Although both of these values are reduced in sepsis-induced cardiomyopathy, their improvement may fail to restore tissue and organ oxygen levels (91). Turns out this reduced cardiovascular performance is attributed to mitochondrial dysfunction in the myocardial cells (92). This inability to consume oxygen and generate ATP is referred to as cytopathic hypoxia (93), and can lead to organ failure. In sepsis, mitochondrial dysfunction is one of the driving forces of oxidative stress and anaerobic metabolism leading to organ failure (94,95).

Mitochondria conduct the ETC in the inner mitochondrial membrane as part of oxidative phosphorylation to yield ATP through a series of redox reactions. Oxygen is the final electron acceptor, as monitored by its consumption, which is why more than 90 % of body's oxygen consumption is within this organelle (94). In inflammation, oxygen demand is higher as leukocytes increase their oxygen demand linearly as they release ROS to combat the infection (96). Superoxide and NO are able to interrupt the ETC process by inhibiting complexes, thus reducing ATP generation (97). In a study conducted by Brealey et al., skeletal muscle biopsies from critically-ill patients with sepsis revealed lower ATP concentration in non-surviving patients (98). This lack of ATP and oxygen forces the cells to switch to anaerobic metabolism to maintain their energy supply, resulting in metabolic acidosis.

Taken together, the hypoperfusion, capillary leakage, dysregulation in coagulation, and mitochondrial malfunctions, lead to organ failure. Oxidative stress is an underlying player in most of these factors. Thus, studies have shown exhausted antioxidant capacity to be associated with organ failure, which correlates with the acute physiology and chronic health evaluation II (APACHE II) score (99). If two or more organs are experiencing progressive dysfunction in sepsis, it will be referred to as multiple organ dysfunction syndrome (MODS). When assessing for MODS, microcirculatory measurements of arterioles, capillaries, and venules, have shown to be more indicative of organ failure occurrence and outcome than macrocirculatory parameters. Altered microcirculation and redistribution of blood serves as a prognostic parameter for survival in patients with sepsis, where patients with altered microcirculation have higher mortality rates as assessed by microscopy and tissue oxygenation (100,101).

The compensatory anti-inflammatory response that follows the early hyperactivated immune state does not often restore immunological balance. Immune dysregulation is still observed as leukocytes have a pathologically attenuated response to PAMPs through reduced cytokine production as well as a lower response to chemotaxis ("immune paralysis"). In the adaptive branch of immunity, the CD8+ and CD4+ T cells populations in patients with sepsis decline as a result of their impaired function and increased apoptosis (102). This leaves the patients vulnerable to secondary infections and long-term consequences. Lymphopenia has been postulated to serve as a biomarker since its levels in sepsis can serve as a prognostic factor in 28-day and 1-year mortality (103).

Iron regulation plays a key role in susceptibility to infections as patients with hemochromatosis have higher risks of infection (104). Given the iron dysregulation in sepsis, hemochromatosis can impact the survival and outcome significantly. Higher non-transferrin bound iron levels in chemotherapy patients were associated with a higher risk of Gram-negative infection and sepsis (105). In a study by Tacke et al., critically ill patients with sepsis had higher ferritin and hepcidin levels, and lower serum iron and transferrin levels (106). In another study, higher serum iron levels were associated with a step-wise increase in 90-day mortality (107). Experimentally, HFE knockout mice, which experience

dysregulated iron homeostasis, had twice as high mortality rate in a cecal ligation and puncture (CLP) model of abdominal sepsis when they were on a high iron diet (108). This can be compared to critically ill patients who have disruptions of iron homeostasis due to mmultiple blood transfusions (109). Regarding ROS production, which is iron-dependent, patients with sepsis have an increased level of ROS as indicated by lipid peroxidation (110) and lowered antioxidant status (111). In survivors, the antioxidant potential is higher than in non-surviving septic patients whose antioxidant levels never recovered (112, 113). Many different antioxidants levels are reduced in sepsis including vitamin C (114) and thus, there has been evidence to support antioxidant therapies (115).

Current treatment consists of evidence-based treatment care bundles such as early goal directed therapy (EGDT), to bring various physiological parameters to the baseline levels in a time-sensitive manner. It is also important to identify high risk groups early on and to personalize the target goal. The most recent Surviving Sepsis Campaign guidelines in 2018 created a 1-hour bundle that is to be achieved for patients suspected of having sepsis or septic shock (116). This includes broad spectrum antibiotic administration (ideally after obtaining culture and swabs), fluid resuscitation and use of vasopressors to address hypotension within one hour of their admission. As part of supportive therapy, other therapies such as corticosteroids, insulin, analgesics and antipyretics are administered if needed. Delivery of the EGDT or the sepsis resuscitation bundle within the first six hours reduced 28-day mortality in sepsis patients, an effect that diminished with improvement in general treatment protocols (117, 118).

In order to develop and test potential treatments, various experimental models of sepsis are utilized. Mice are the most common animals studied due to their availability, access to genetically-modifiable mice and specific reagents, cost, and previous research knowledge obtained in their species (119). Rats are also utilized, and their advantages are similar to mice. Bigger animals such as pigs and sheep allow more frequent blood sample collection, remove some technical and instrumentations issues, and have closer physiological and biological readouts to humans. However, there are ethical, financial, and zootechnical issues that make them less likely to be used in studies (119). Despite the anatomical and

physiological disparities, murine models continue to be the most commonly used animal models of sepsis and are regarded as great pre-clinical and proof-of-concept models.

The experimental sepsis models are inspired by the most common sites of infection (lower respiratory tract, bloodstream, abdomen, and urinary tract). In endotoxemia model, bacterial components such as LPS can be injected intravenously (IV) to induce systemic inflammation and study the acute hyper inflammatory response observed in sepsis (120). Its advantages are that it is easy to perform, it is reproducible, and the toxin amount can be controlled (120). Abdominal sepsis models are commonly used which include fecal slurry, CLP, CASP. In the fecal slurry model, a standardized amount of fecal matter in suspension is injected intra-peritoneally (121). Although this allows control over the amount of inflammatory trigger and is only moderately invasive, it does not mimic the heterogeneity observed in human sepsis pathophysiology and progression. To overcome this limitation, CLP and colon ascendens stent peritonitis (CASP) models can be utilized. In CLP, the cecum is ligated and punctured whereas in CASP, a stent is placed into the ascending colon to allow fecal matter leakage. Both of these models mimic the clinical progression of sepsis in humans; the experimental leakage of fecal matter into the abdominal cavity simulates events that occur following trauma, surgery, and peritonitis (122). Though the CLP model was regarded as the "gold standard model", it poses the risk of the puncture being blocked (e.g., by coagulation or adhesion). This makes CASP model superior as the stent is sutured in place to allow continuous leakage. Pneumonia-induced sepsis is an extra-abdominal cause of sepsis, which can be experimentally replicated with intranasal or intratracheal administration of LPS or bacteria (123, 124). In urosepsis models, bacterial injection into the bladder can help shed a light on UTI-induced sepsis (125). When it comes to inoculation, the strain and the number of bacteria can affect the severity and rate of sepsis progression. Even more complex sepsis models exist where two-hit insults are utilized such as abdominal infection followed by bacterial-instilled pneumonia to mimic the development of hospital acquired infections (after trauma or abdominal surgery) (126).

In addition to using the appropriate model(s), it is important to have standardized treatments and guidelines in place to improve the translation of experimental findings from the bench to the bedside. As such, at the Wiggers-Bernard Conference in Vienna, 2017, a series of recommendations and considerations were proposed as "best practices" for animal models of sepsis (127–129). These guidelines, minimum quality threshold in pre-clinical sepsis studies (MQTiPSS), include study design, humane modeling, types of infections, organ dysfunction, fluid resuscitation, and antimicrobial therapy endpoints. In an attempt to reduce the gap between murine and human sepsis treatment conditions, animal ICU models can be used to assess preclinical investigation in more relevant population (adult and aged mice and rats with chronic morbidities) to make the treatments more comparable and reflect clinical setting (119). Miniature size of equipment in ICU such as ventilators would serve to support the animal, in addition to the fluid resuscitation, antibiotics administration, vasopressor support, and hemodynamic monitoring. Though conducting every experimental sepsis study in miniature ICUs may not be feasible yet, it proposes a solution to narrowing the gap between murine and human sepsis studies.

There is no FDA approved treatment for the immune dysregulation in sepsis available yet. Earlier interventions, i.e. effective treatment concepts of the early hyperactivation immune state, are always preferred as to attenuate cumulative damage and worsened outcome due to the prolonged course of the disease. Having a pharmacological approach that targets both the immune dysfunction (pathologically increased ROS production) as well as the infection (iron-dependent bacterial growth) is the goal. Given the dual role that iron plays in both pathways, studying iron chelation offers an exciting and promising potential for sepsis therapy.

1.3.2. Cystic Fibrosis

CF is an autosomal recessive genetic disease affecting the cystic fibrosis transmembrane conductance regulator (CFTR) channel. CF is the most fatal genetic disease amongst the Caucasian population. According to the Canadian Cystic Fibrosis Registry, one in every 3,600 children are born with CF and more than 4,300 patients are receiving treatments

nationwide. The CF population in Canada has increased by 37.5 % in the last 2 decades (130). This is attributed to the improvements in quality of life and the increased median age of survival (over 50 years).

CFTR is the only cAMP-activated channel within the ATP binding cassette (ABC) superfamily of transporters and it is expressed on the apical membrane of epithelial cells. It is responsible for transporting various anions, largely chloride ion. There are six major classes of CFTR mutations which result in either a partial or total loss of function of this channel (131). Of these mutations, deletion of the amino acid phenylalanine at the 508th position (ΔF508) from the second class, is the most common mutation in patients with CF (131). The severity of the disease varies from one person to another, though its hallmarks, chronic inflammation and recurrent infections, are present in all the patients. Given the physiological importance of CFTR in epithelial cells of exocrine tissues, its defect causes a multi-system disorder. Examples include gastrointestinal enzymatic deficiency which interferes with fat and protein digestion (132). This can result in malnutrition, element deficiencies, and weight loss. CF patients can also develop CF-related diabetes due to impaired insulin secretion by the pancreas (133). Nevertheless, the current leading cause of death is lung disease, where progressive damage reduces its function (134).

The pathophysiology of CF begins with the impaired CFTR channel, which is responsible for trans-epithelial transport of chloride (to the apical side) as well as other anions including glutathione, bicarbonate, and thiocyanate. This channel is important in regulating ion and water absorption across the epithelium and thus it interacts closely with the epithelial sodium channel (ENaC; 132). In normal airways, CFTR and ENaC coordinate to balance fluid secretion and absorption. In CF, the loss of CFTR activity is linked to hyperactivity of ENaC, resulting in a higher absorption of sodium from the airways (135). Since water follows sodium, the airway surface liquid (ASL) diminishes and the airway becomes dehydrated.

CFTR mutation also leads to mucous hypersecretion, narrowing the airway which is referred to as mucous plugging (136). Ciliary dysfunction is also present as cilia mobility

is restricted by the thick mucus layer. Given the thickness and viscosity of the CF mucous layer of ASL, antimicrobial secretions such as lactoferrin, lysozyme, surfactant proteins A and D into the airways become compromised. Altogether, these defects impair the elimination of inhaled pathogens and foreign substances from the upper respiratory tract, known as mucociliary clearance (MCC; 38). This creates the ideal niche for pathogens and opportunistic bacteria to colonize and create biofilms.

While infections exacerbate the clinical symptoms, baseline dysregulation of inflammatory processes have been shown to contribute to CF pathology. It is hard to assess the inflammatory and infection aspects of CF independently, but there is evidence to link CFTR mutations to constitutive activation of pro-inflammatory signaling pathways, even in the absence of infection (137). In addition to NF-κB, other important intracellular signaling proteins are also induced including AP-1, P38 and MAP kinases (138). These pathways activate NADPH oxidase and contribute to ROS accumulation. In CF, there are higher concentrations of pro-inflammatory mediators such as IL-1β and TNF-α, while there are reduced levels of anti-inflammatory mediators such as IL-10 (139).

Neutrophil-driven inflammation contributes significantly to the pathology and lung damage observed in CF. Upon the activation of pro-inflammatory signaling cascades such as NF-κB pathway, IL-8 (a neutrophil chemokine) is released. This causes neutrophil recruitment to the site of inflammation. These neutrophils employ their potent innate defence mechanisms such as ROS production, antimicrobial protease release, and even initiate neutrophilic extracellular traps (NETs) which releases their DNA (140). The MAPK signaling cascade of neutrophils can be further activated, releasing more IL-8 and feeding the vicious cycle of neutrophil-induced damage. Infections further induce IL-8 release and neutrophil recruitment to the site of inflammation. Despite the accumulation of neutrophils, pathogen clearance efficacy is decreased as a CFTR defect reduces their phagocytic ability (141). Long term presence of neutrophils, such as in chronic diseases like CF, leads to lung injury and bronchiectasis (142–144).

Bicarbonate is an important buffer for maintaining physiological pH through the CFTR channel for trans-epithelial transport. Reduced levels of bicarbonate in CFTR-expressing tissues causes acidification (145). This lower pH prevents activation of important pH-sensitive proteins including SPLUNC1, an inhibitor of ENaC (146), which also possesses antimicrobial and antibiofilm properties (147–150). This acidic environment also reduces the antimicrobial activity of β-defensin and LL-37 cathelicidin against *P. aeruginosa and S. aureus*, compromising the innate immunity (151).

During an infection, there is a heightened, yet ineffective, innate response which leads to infection persistence (152). CFTR deficiency reduces PAMP recognition which is a critical step in initiating the inflammatory response. These cells have reduced TLR-4 expression which impedes the expression of anti-microbial and anti-inflammatory mediators in response to toxins such as LPS (153). As TLR-4 signaling is needed for resolution of pulmonary inflammation in lung injury, its downregulation in CF promotes immunosuppression and fibrosis (154). CFTR mutation reduces TLR-mediated immunity which interferes with the startup of appropriate signaling cascades through MYD88 and TRIFF pathways (155–157). This interferes with recognition and response to the pathogens.

Given the compromised innate immunity of CF patients, bacteria colonize the airways. These bacteria are mostly commensal pathogens such as *P. aeruginosa*, *S. aureus*, and *Burkholderia cenocepacia*, which have evolved mechanisms to evade the immune system (158). *P. aeruginosa* can shift to biofilm colonization, disguise itself in alginate coats to scavenge hypochlorite, and prevent its phagocytosis (159). Impaired clearance leads to recurrent infections and chronic inflammation causing airway remodeling, bronchiectasis, and emphysema (160, 161).

Oxidative stress and iron dysregulation contribute to the pathogenesis of CF, similar to sepsis (36). In healthy tissues, antioxidants would neutralize the ROS present. A CFTR defect directly affects the oxidative status as it is responsible for transporting glutathione and thiocyanate antioxidants. Although ROS is utilized for its antimicrobial effects, its level as studied by oxidation markers, does not decrease despite infection resolution in the lungs

of CF patients (36). The bronchial ciliated and type II alveolar epithelial cells further increase the oxidative stress by producing ROS through their apical NADPH oxidases: DUOX1 and DUOX 2 (162). Together, the epithelial dysfunction and higher pro-inflammatory signaling leads to excessive polymorphonuclear cells activation and subsequently ROS release within the airways (163). This supports the pathologic impact (such as chronic airway damage) of ROS in CF instead of its usual immunoregulatory role. It has been shown that increased iron and iron-related proteins levels are present in bronchoalveolar lavage fluid, macrophages, and explanted lungs of CF children patients (164). Further contributing to the increase of *P. aeruginosa* growth and biofilm formation in the airways, bronchial epithelial cells with ΔF508-CFTR mutations have increased iron release from their apical membrane. Interestingly, iron chelation was able to reduce this biofilm formation (165).

Despite the advancements in treatments and care for CF patients, there is no definitive cure yet. Patients with CF take a cocktail of medications on a daily basis to address the systemic effects of a CFTR defect. The main types of drugs taken to directly target the CFTR function are potentiators, which increase the function of CFTR channels, and correctors, which enhance the trafficking of the CFTR protein to the apical membrane. The most recent FDA-approved treatment for CF patients of 12 years and older, is a triple therapy of Elexacaftor-Tezacaftor-Ivacaftor (166). This CFTR-modulator therapy is approved for patients with at least one copy of the ΔF508 mutation, which includes 90 % of patients with CF. Additional drugs to address the symptoms of CF are anti-inflammatory drugs (corticosteroids), antibiotics (azithromycin), antioxidants (N-acetyl cysteine), anti-proteases, and hyperosmolar agents (167). With the rise of multi-drug resistant bacteria in CF airways and given that biofilms further reduce this antibiotic susceptibility, there is pressure to find alternative ways to treat the infection. Iron removal can increase antibiotic activity and thus be used as an adjuvant. Additionally, iron chelation has potential for being a therapeutic agent in CF as it can reduce inflammation by modulating oxidative stress.

1.4. Iron chelators

There is a growing body of evidence showing iron dysregulation and ROS overproduction during immune system-driven pathologies. Since iron is critical in catalyzing ROS production and its levels are important in survival and immune defence, modulating its levels may provide therapeutic potential.

Iron chelators have been introduced clinically to treat patients with iron overload conditions. This includes hemochromatosis, where hepcidin function is impaired, and in thalassemia, where a defect in hemoglobin production reduces erythropoiesis and thus frequent blood transfusions are needed. There are currently three FDA-approved iron chelators: desferasirox (DFX), deferoxamine (DFO), and deferiprone (DFP). They each have their own biological and chemical properties (Table 1).

Desferasirox (Exjade®) is a tridentate iron chelator and was the first oral medication approved for chronic iron overload induced by long term blood transfusion. Two molecules of DFX bind to a single molecule of Fe^{3+} to create an intracellular complex (168). It is predominantly excreted via feces (84 %); it is also eliminated via the kidney (8 %). It has a long half-life of 8-16 hours which provides the advantage of less frequent dosing, resulting in increased patient compliance with treatments (169). Unfortunately, due to its significant risk and side effects, it is listed as the second-ranked drug on the "most frequent suspected drugs reported in patients' deaths" list (170,171). These risks include GI hemorrhage, kidney and liver failure.

Deferoxamine (Desferal®) is a siderophore that has the ability to bind both extracellular aluminum and iron. A single molecule of DFO binds to a Fe^{3+} iron and forms a stable complex. Due to its low lipophilicity, it cannot be administered orally and is instead administered intramuscularly (if patients are not in shock) and slowly intravascularly (if patients are in shock or experiencing cardiovascular collapse) (172). It has a bi-phasic half-life: of 1-hour rapid phase followed by 6 hours slow phase and it is eliminated renally (173). DFO is a derived from *Streptomyces pilosus* bacteria and thus is associated with the risk of supplying the iron to the bacteria during an infection. The most common adverse reactions

	Desferasirox (DFX)	Deferiprone (DFP)	Deferoxamine (DFO)	DIBI (Under Study)
Route of administration	Oral	Oral	Subcutaneous or intravenous	Intravenous
Plasma half life	8-16 hours	< 2 hours	30 minutes	< 2 hours
Iron binding ratio	2 DFX: 1 Fe (tridentate)	3 DFP: 1 Fe (bidentate)	1 DFO: 1 Fe (hexadentate)	1 DIBI: 3 Fe (copolymer with nine hydroxypyridinone)
Plasma excretion	Fecal	Urine	Urine, fecal	Urine
Iron III molecular complex	Uncharged (extracellular complex in clinical studies; intracellular complex in laboratory studies)	Uncharged (intracellular complex)	Charged (extracellular complex)	Charged (extracellular complex; capable of mobilizing intracellular iron)
Advantage(s) in inflammation and infection context	*More efficient at iron binding than DFP or DFO	*Synthetic *Deprives iron from an intracellular pathogen	Most extensively studied	*Strong iron chelation; holds iron in a non-redox active state *broad spectrum antimicrobial *Synthetic origin *Toxicity profile
Disadvantage(s) in inflammation and infection context	*Long half-life thus challenging to monitor for guiding therapy *Holds iron in a redox-active state	*Neutropenia and agranulocytosis *Holds iron in a redox-active state	Siderophore origin; promotes microbial growth	Relatively limited studies

Table 1. Comparison of the different iron chelators included in this study.

associated with DFO use are hypersensitivity reactions, GI events (diarrhea, nausea, ulcer, and disturbances), hearing loss, and eye problems (174). Deferiprone (Ferriprox®) is an orally-administered bidentate iron chelator. Three molecules of DFP are needed to chelate a single molecule of intracellular iron. It has a half-life of 2-3 hours and is excreted through urine. Although it can bind to other metals (zinc, copper, aluminum), it has a higher affinity for iron. Most common side effects are GI disruptions and long term uses leads to progressive hepatic fibrosis in patients with thalassemia (175). Neutropenia and agranulocytosis are also reported which increases the risk of infections (176). There are experimental studies that combine iron chelators to utilize multiple properties. For example, DFP and DFO are used together to mobilize intracellular and extracellular iron, respectively (177). Given the toxicity profile of these FDA-approved drugs, there is a need for novel iron chelators with less toxicity.

DIBI is a synthetic and water-soluble iron chelator developed by Chelation Partners Inc. (Halifax, NS, Canada). DIBI has high affinity and selectivity for iron. It is made up of a polyvinylpyrrolidone (PVP) backbone with MAHMP chelating agents where one molecule of DIBI binds to three molecules of extracellular iron. This chelator is under study to better understand its biological and chemical properties as it is being prepared for clinical trial. DIBI has shown to hold iron in a non-redox active state. DIBI has been tested by using the Organization for Economic Cooperation and Development (OECD)-prescribed oral and systemic toxicity in rats which showed no observable adverse effects as assessed by 14-day repeated dosing of DIBI doses of 1,000 mg/kg/day (oral) and 500 mg/ kg/day (IV) (178). To introduce iron chelation as a treatment in (hyper-)inflammation and infection, there are important criteria to consider: 1) the ideal chelator must not supply iron to pathogens, 2) its affinity for iron must be higher than leukocytes to effectively reduce ROS levels, and 3) it must hold iron in a redox-inactive state (non-accessible iron). A shorter half-life is also preferred as to control its levels in the body more closely. Although DIBI has shown some of these qualities, its therapeutic effect on systemic inflammation remains unexplored.

1.5. Hypotheses

This research investigated the effect of iron chelation in inflammation and infection. Iron plays a pivotal role in innate immunity by catalyzing ROS production and it is required by bacteria for survival and growth. We hypothesized that iron chelation attenuates excess inflammation, by reducing leukocyte-endothelial interactions, reducing inflammatory mediator release, and limiting infection by restricting bacterial growth.

1.6 Study objectives

The aim of this research was to provide experimental evidence for the potential of iron chelation in modulating the inflammatory response and reducing infection. The first objective was to analyze the effects of iron chelation in inflammation. First, as a proof of principle, we wanted to study the impact of the novel, highly specific iron chelator, DIBI on intracellular iron levels in neutrophils by calcein acetoxymethyl ester assay. Neutrophils are the first cells to arrive at the site of inflammation and they utilize iron to generate ROS. Thus, they were the ideal cells to assess their response to iron chelation. Next, we wanted to study the impact of different iron chelators in clinical inflammation to assess potential anti-inflammatory properties. As an example for systemic inflammation, we used the endotoxemia model of sepsis (induced by LPS administration) to evaluate iron chelation efficacy at alleviating the immune (hyper-)activation. We studied leukocyte-endothelial interactions and changes to capillary perfusion using intravital microscopy, analyzed plasma inflammatory mediator levels, and evaluated histological damages in the intestine.

The second objective was to study the impact of iron chelation in infection. We utilized the colon ascendens stent peritonitis (CASP) model, which closely mimics the clinical course of abdominal infection. A stent was placed into the ascending colon to allow fecal matter leakage into the sterile abdominal cavity. This model allowed us to assess the anti-bacterial effects of iron chelators, in addition to evaluating their anti-inflammatory properties. We analyzed leukocyte-endothelial interactions, capillary perfusion, plasma inflammatory mediator levels, bacterial burden, and histological changes in the intestine. Next, we introduced an additional surgical step to control the source of infection, thus establishing

the CASP-intervention (CASP-I) model. We assessed DIBI's efficacy in combination with antibiotic treatment on mortality over 7 days. Intestinal damage and bacterial burden within the abdominal cavity were also measured.

The third objective was to assess the impact of iron chelation in infection (LPS challenge) with pre-existing inflammation. Thus, nasal epithelial cells with CF disease-causing mutations were selected due to their baseline cytokine production level. Changes to the inflammatory response were evaluated by measuring IL-6 and IL-8 levels. Additionally, the molecular mechanism following iron chelation in response to LPS challenge was evaluated by identifying nuclear factors involved in the signaling cascade such as phosphor (P)-STAT1, P-STAT3, and NF-κB-P65, using immunofluorescence.

CHAPTER 2: MATERIALS AND METHODS

2.1 Cellular experiments

2.1.1 Flow cytometry-based measurement of the labile intracellular iron pool

2.1.1.1 Neutrophil isolation

Wildtype male C57BL/6 mice (8-10 weeks old; 20-30 grams) were sacrificed via cervical dislocation. EasySep™ Buffer (Stemcell Technologies, Vancouver, BC, Canada), containing 2 % fetal bovine serum (FBS) and 1mM EDTA in Dulbecco's phosphate-buffered saline (PBS), was used to suspend the cells throughout the neutrophil isolation procedure. Cells were flushed and filtered from bone marrow (tibia and femur) using 26-gauge needle. The cells were then centrifuged at 300xg for 10 minutes in preparation for neutrophil-isolation. For the neutrophil isolation, instructions were followed from the EasySep™ Mouse Neutrophil Enrichment Kit (Stemcell Technologies). Briefly, isolated cells were suspended in the Easy Sep Buffer ($1x10^8$ cells/mL), and were incubated in rat serum (50 µL/mL) and Enrichment Cocktail (combination of monoclonal antibodies in 0.1 % bovine serum albumin; 50 µL/mL) for 15 minutes at 4 °C. The cells were then washed, resuspended, and were incubated in Biotin Selection Cocktail (combination of monoclonal antibodies in PBS; 50 µL/mL) for 15 minutes at 4°C. Next, Magnetic Particles (a suspension of magnetic particles in Tris-buffered saline; 150 µL/mL) were added and were incubated for 10 minutes 4 °C. The cell suspension was placed into EasySep™ magnet (Stemcell Technologies) for 3 minutes at room temperature. By inverting the magnet, single cell suspensions of neutrophils were yielded through negative selection. The neutrophils were 85 % pure and viable as sorted by fluorescence-activated cell sorting (FACS) according to manufacturer's supplied information manual. The neutrophils were used immediately for experiments.

2.1.1.2 Neutrophil culture and stimulation

The freshly-isolated neutrophils were cultured on 6-well plates (250,000 cells in 2 mL medium/well). The medium consisted of RPMI supplemented with 5 % FBS, 1 % L-glut, 1 % penicillin and streptomycin, and 0.5 % HEPES. The cells were stimulated with LPS (100 ng/mL), with or without DIBI (25 µM or 200 µM) in pre-warmed medium for 4 hours.

After this incubation time, the cells were harvested using TrypLE Express (Gibco) and were then centrifuged. After removing the supernatant, the cell pellets were ready for staining.

2.1.1.3 CA-AM staining for labile iron pool and FACS analysis

Calcein acetoxymethyl (CA-AM; Millipore Sigma) is hydrolyzed within viable cells' cytoplasm to fluorescent calcein. This calcein is quenched in a stoichiometric fashion following binding to intracellular iron (179). Though calcein can also chelate magnesium and calcium, under physiological pH chelation of these elements are considered minimal. Thus, the fluorescence intensity measured within the neutrophils were assumed to be due to chelation and quenching of iron only. As calcein is light sensitive, it was prepared freshly each time and all the steps were conducted in the dark. Various doses of calcein (0.5, 0.37, 0.30, 0.15 μM) were studied to find the optimum working stock in regard to fluorescent range and detection sensitivity. Working stock of 0.15 μM CA-AM was selected and made in pre-warmed serum-free RPMI. The treated cells were incubated in media and calcein for 30 minutes in the dark. Negative control (non-stained) cells were included for each treatment group to control for baseline fluorescence. The cells were washed (with PBS) and centrifuged at 300xg for 10 minutes. The cells were resuspended in 0.5 mL of PBS and were now ready for FACS analysis.

Fluorescence of CA-AM-labeled neutrophils was measured using a FACSCanto II flow cytometer (BD Biosciences, Mississauga, ON) equipped with BD CellQuest™ software. Appropriate unstained control cells were used. A minimum of 1×10^4 cells was collected for flow cytometric analysis. Cells were gated on the live cell population on FSC-H versus SSC-H plot and linked to relevant CA-AM histogram acquisition plots. The threshold was set to 5000 on FSC-H for all assays. FCS Express Version 7 was used to analyze the data (De Novo software, Los Angeles, CA, USA).

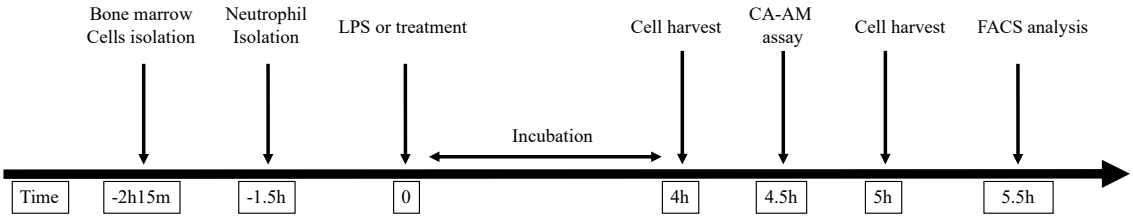

Figure 4. Experimental timeline for calcein acetoxymethyl (CA-AM) intracellular iron measurements.

Table 2. Experimental groups for calcein acetoxymethyl (CA-AM) intracellular iron measurements.

Model	Groups	Intervention
CA-AM assay	1- Control	Media
	2- DIBI 25	DIBI (25 μM)
	3- DIBI 200	DIBI (200 μM)
	4- LPS	LPS (100 ng/mL)
	5- LPS+DIBI 25	LPS (100 ng/mL) + DIBI (25 μM)
	6- LPS+DIBI 200	LPS (100 ng/mL) + DIBI (200 μM)

*All groups included a non-stained control

2.1.2 Modulation of inflammatory profile of cystic fibrosis with iron chelation

2.1.2.1 CF and Calu-3 cell cultures

CF nasal epithelial cell line (CF15), homozygous for the Δ508 mutation in the CFTR gene was generated as previously described (180). For cell culture, the CF15 cells were grown in Dulbecco's Modified Eagle's Medium supplemented with 10 % FBS; 0.088 % transferrin, 0.088 % triiodo-L-thyronine, 0.0088 % epithelial growth factor; 1.76 % hydrocortisone; 0.044 % insulin, 0.088 % epinephrine; and 0.176 % adenine. The cells were grown until they reached confluence in T25 flasks (Corning, Corning, NY) at 37 ℃ in a 5 % CO_2 atmosphere. Calu-3 human airway epithelial cells were cultured until confluence and tight junction (TJ) formation using the above procedure at 5 % CO2 at 37 ℃ in Calu-3 media (84.8 % MEM; 0.848 % Penicillin-Streptomycin (1 %); 12.7 % FBS; 0.848 % non-essential amino acids; and 0.848 % (1%) sodium pyruvate). Cell culture medium and supplements were purchased from GIBCO (Burlington, ON, Canada) and Sigma Aldrich (St. Louis, MO). Upon confluency, the cells were detached with 0.1 % trypsin-EDTA and were seeded into transwells (24 mm diameter with 0.4 μM diameter pores; Corning Life Sciences, Acton, Mass.) with both apical and basolateral compartments filled with 2 mL of the described culture media. After one-week, and the formation of CF15 tight monolayers, the apical medium was removed. The monolayers were then maintained under air-liquid interface conditions to achieve polarization and differentiation. Following the removal of the apical medium, the medium in the basolateral compartment was changed every two days until the cells achieved a dry apical surface and were deemed ready for stimulation.

2.1.2.2 Cell stimulation

Following cell polarization and TJ formation, cell transwells were designated as either control (medium), stimulation with bacterial toxin (LPS), co-treatment with DIBI (LPS + DIBI) or DIBI alone (DIBI). Stimulation with LPS (from *Escherichia coli*, serotype O26:B6; Sigma-Aldrich, Oakville, ON) was performed in fresh phenol-red free medium at concentrations of 100, 200, or 300 ng/mL for bidirectional stimulations of the CF15 cells. Once optimal LPS stimulation conditions were established (200 ng/mL dose for 24 hours), the experimental groups were tested: control (medium only), LPS (200 ng/mL), LPS + DIBI

(25, 50, 100 or 200 μM), DIBI only (25, 50, 100 or 200 μM). The appropriate stimulation medium was applied to both the apical and basolateral surfaces at volumes of 0.5 mL and 2.5 mL, respectively. The cells were left to incubate for 24 hours in a 37 ℃ and 5 % CO_2 environment before cell harvesting.

2.1.2.3 Cell harvesting

Bovine serum albumin and Bradford Dye Reagent were purchased from BioRad (Hercules, CA). Following the incubation period, apical and basolateral cell media were collected for determination of cytokine production. Cell supernatant was aliquoted and stored at -80 ℃ for later analysis. The adherent monolayers of cells were harvested by washing the cells twice with ice-cold PBS, scraping, and centrifuging the cell materials at 13000xg for 20 minutes. Cell pellets were then collected and lysed on ice for 45 minutes using a RIPA lysis buffer supplemented with a protease inhibitor solution as previously described (181). Lysates were centrifuged at 13000xg for 20 minutes to eliminate cell debris. The supernatant was collected and frozen at -80 ℃ for later analysis of protein concentration.

2.1.2.4 Determination of Cytokine Secretions by ELISA

According to the manufacturer's instructions, commercially available enzyme-linked immunosorbent assay (ELISA) kits were used to measure the IL-6 and IL-8 secretions into the apical and basolateral cell culture supernatants. Monoclonal human IL-6 and IL-8 antibodies (catalogue numbers 88-7066-88 and 88-8086-88, respectively; Invitrogen, Carlsbad, CA) were used. The cytokine secretions were normalized to the protein concentration of the lysed cells, as measured via the Bradford Colorimetric Assay (BCA). The treatments revealed minimal changes in the total protein concentrations of the groups as assessed by BCA.

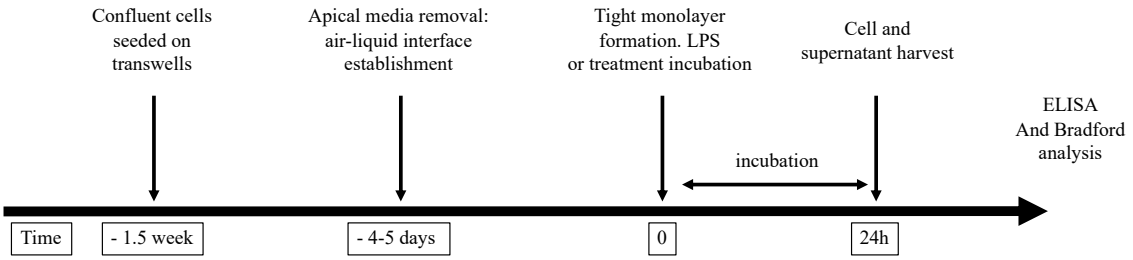

Figure 5. Experimental timeline for CF15 cytokine secretion.

Table 3. Experimental groups for CF15 cytokine secretion.

Model	Groups	Intervention
Cytokine secretion in Transwell-culture	Control	Media
	DIBI 25	DIBI (25 μM)
	DIBI 50	DIBI (50 μM)
	DIBI 100	DIBI (100 μM)
	DIBI 200	DIBI (200 μM)
	LPS	LPS (200 ng/mL)
	LPS+DIBI 25	LPS (200 ng/mL) + DIBI (25 μM)
	LPS+DIBI 50	LPS (200 ng/mL) + DIBI (50 μM)
	LPS+DIBI 100	LPS (200 ng/mL) + DIBI (100 μM)
	LPS+DIBI 200	LPS (200 ng/mL) + DIBI (200 μM)

2.1.2.5 Immunofluorescence

The CF15 cells were grown on sterile glass coverslips at low density at 37 ℃ in a 5 % CO_2 atmosphere. The cells were cultured for 24 hours in the appropriate culture medium (DMEM supplemented with 10 % FBS; 0.088% transferrin, 0.088 % T3, 0.0088 % epithelial growth factor; 1.76 % hydrocortisone; 0.044 % insulin, 0.088 % epinephrine; and 0.176 % adenine), containing LPS (200 ng/mL) with or without DIBI (25 μM or 200 μM). The treatment groups were as following: Control (medium alone), LPS (200 ng/mL), LPS + DIBI 25 μM, LPS + DIBI 200 μM, DIBI 25 μM, and DIBI 200 μM. The medium was removed, and the cells were washed four times with PBS. They were then fixed with 2 % paraformaldehyde (in PBS) for 20 minutes, and permeabilized with permeabilization buffer (0.1 % TritonX-100, 2 % BSA in PBS) for 45 minutes. The cells were then incubated overnight in single unstained primary antibody diluted in 0.1 % TritonX-100, 0.2 % BSA at 4°C: NF-κB anti-P65 antibody (1:150, sc-8008, Santa Cruz Biotechnology Inc., Dallas, Texas, US), anti- P-STAT1 antibody (1:75, 33-3400, Thermo Fisher Scientific, Waltham, Massachusetts, US), or anti- P-STAT3 antibody (1:100, PA5-17876, Thermo Fisher Scientific).

Next day, the cells were washed with PBS, 0.1 % TritonX-100 three times for 10 minutes (to remove primary antibody), and incubated in Alexa Fluor® 488-conjugated donkey anti-mouse IgG (1:250, code 715-545-150, Jackson ImmunoResearch Laboratories, Inc., Pennsylvania, United States) for 1 hour. The secondary antibody was diluted in 0.1 % TritonX-100, 0.2 % BSA. Every step following and including the 1-hour incubation in the secondary antibody were conducted in the dark. The cells were washed, the coverslips were removed from the dishes, mounted on a glass microscopy slide with DAPI-containing mounting media, sealed with nail polish, and allowed to dry at room temperature (20 min) before storage at −20 °C. Slides were viewed using a Zeiss Axio Imager Z2 W/Monochrome camera at the Dalhousie Cellular & Digital Imaging Facility of the Faculty of Medicine. The images were captured at 100X objective under oil immersion using the Zeiss blue software. Negative controls were performed by omitting the primary antibody.

2.1.2.6 NF-κB P65 Scoring

For measuring P65 target, a total of 30 individual cells were randomly selected for each treatment. The images were captured using 100x total magnification. The degree of target activation was assessed by an arbitrary score: 1= no perinuclear/nuclear signal with signal in the cytosol; 2= some perinuclear signal, no intra-nuclear signal, with signal in the cytosol; 3= perinuclear, and some intra-nuclear signal, with signal in the cytosol; 4= very strong perinuclear signal, strong nuclear signal, with signal in the cytosol (Figure 6).

2.1.2.7 P-STAT1 and P-STAT3 Scoring

For measuring P-STAT1 and P-STAT3 targets, a total of 15 individual cells were randomly selected for each treatment and target. The images were captured using 100x total magnification and they were converted to TIF format. The images were set to greyscale and then every cell was delineated at the cell membrane, and the area integrated density (product of area and Mean Gray value) as well as five measurements of the surrounding background of each cell were calculated using Image J software. The corrected total cell fluorescence (CTCF) was calculated as previously described (182): integrated density − (area of selected cell × mean density of background).

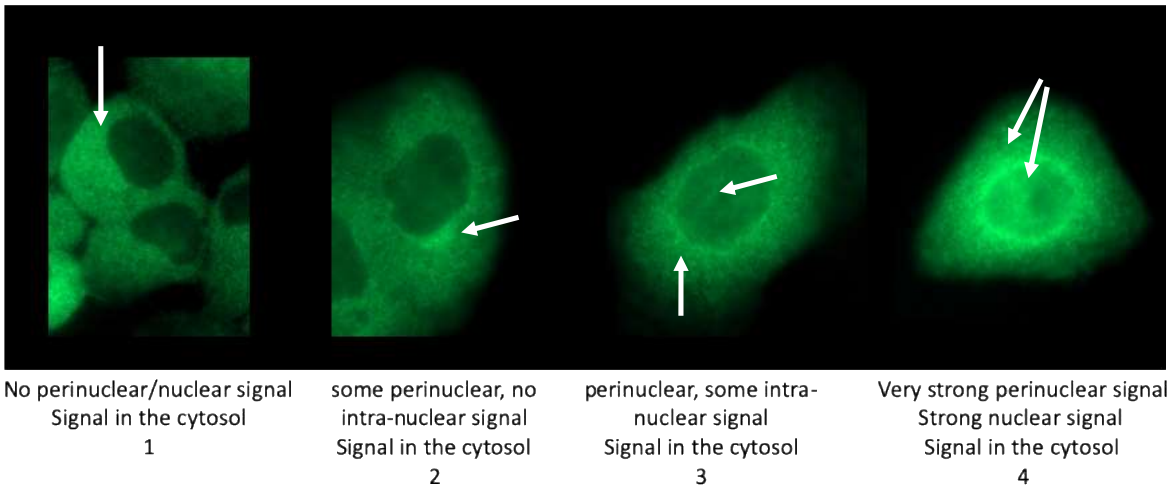

Figure 6. NF-κB P65 scoring in treated CF15 cells.

P65 target (green) in CF15 cells treated with LPS 200 ng/mL and DIBI 25 or 200 µM for 24 hours captured by 100X objective. Scoring system developed in Chappe Laboratory to assess activation and nuclear translocation of the P65 in treatment groups.

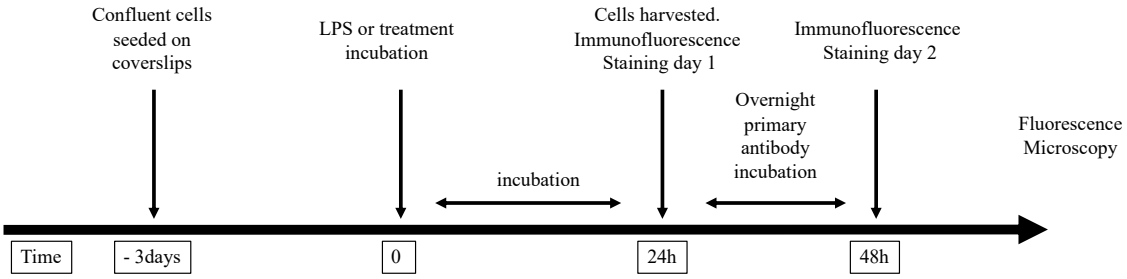

Figure 7. Experimental timeline for CF15 immunofluorescence.

Table 4. Experimental groups for CF15 immunofluorescence.

Model	Groups	Intervention
Immunofluorescence	Control	Media
	DIBI 25	DIBI (25 µM)
	DIBI 200	DIBI (200 µM)
	LPS	LPS (200 ng/mL)
	LPS+DIBI 25	LPS (200 ng/mL) + DIBI (25 µM)
	LPS+DIBI 200	LPS (200 ng/mL) + DIBI (200 µM)

2.2 Animal experiments

2.2.1 Ethics statement

The experimental procedures were approved by the University Committee on Laboratory Animals at Dalhousie University under protocols (17-070, 18-057, 18-090) and were performed in accordance with the guidelines and standards of the Canadian Council on Animal Care. As with the nature of collaboration in research, some data collection and analysis were conducted in external laboratories. These included Dr. David Hoskin's (neutrophil experiments and ELISA), Dr. Jean Marshall's (multiplex plasma analysis), and Dr. Morgan Langille's Laboratories (Microbiome analysis) within Dalhousie University's Faculty of Medicine.

2.2.2 Systemic inflammation model

Wildtype, male C57BL/6 mice (8-10 weeks old; 20-30 grams) were used for this model and were purchased from Charles River Laboratories International Inc. (Saint-Constant, QC, Canada) and they were housed in ventilated plastic cage racks in a pathogen free room (room tested for pathogens every three months). These mice were acclimated for one week in Carleton Animal Care Facility (CACF) of the Faculty of Medicine, Dalhousie University, Halifax, NS, Canada. They were housed in a 12-hour light/dark cycle in 21° Celsius room with supply of standard diet of rodent chow and filtered city water *ad libitum*.

2.2.2.1 Anesthesia and jugular vein catheterization

Mice were weighed and anesthetized by intraperitoneal (IP) injection of sodium pentobarbital (90 mg/kg, 54 mg/mL; Ceva Sainte Animale, Montreal, QC, Canada) that was diluted in 0.9 % sodium chloride (NaCl) saline (1:2 dilution factor). Anesthesia depth was assessed every 15 minutes by pedal withdrawal reflex. Additional sodium pentobarbital was given as needed (1:10 dilution). Once anesthetized, the mice were placed and taped in supine position over heating pad. Body temperature was measured continuously via automated rectal thermometer to maintain body temperature of 37 °C ±

0.5 °C and it was documented every 15 minutes (TCAT-2LV Controller; Physitemp Instruments Inc. New Jersey, USA).

A surgery was performed to catheterize the right jugular vein for IV administration of drugs and other substances. The catheter was prepared in advance of the surgery: a 30-gauge needle was inserted into a non-radiopaque polyethylene tubing (PE10, Clay Adams, Sparks, MD, USA) and secured with waterproof glue. The catheter was tested for obstructions/leakages prior to securing it in place. To begin, the abdominal and anterior-lateral neck area were shaved and disinfected. Next, a small incision was made in the right side of the neck to dissect the jugular vein (approximately 5-7 mm exposed region). Using a silk thread, the cranial end of the vein was tied off (to block perfusion of the vein). Using micro-dissecting scissors to make a cut in the vein, the catheter was inserted into the vein and pushed approximately 1 cm into the vessel. It was secured in place by knotting a silk thread around the catheter and both the inferior and superior ends of the vessel. Once the catheterization surgery was completed, the substances were administered IV through it. Each IV administration was followed by a 0.02 mL saline flush to ensure all solution was IV infused.

2.2.2.2 Experimental timeline

The timeline started with preparation of animals and anesthesia induction. Once the mouse was anesthetized, the right jugular vein was catheterized. Administration of LPS (from *Escherichia coli* at 5mg/kg; Sigma-Aldrich, Oakville, ON, Canada) marks the T=0 timepoint in the timeline. This LPS solution (1 mg/mL concentration using 0.9 % NaCl saline) was administered over few minutes. At T=15 minutes, treatment (one of the iron chelators) or vehicle (for control group) was IV administered. At T=1 hour 45 minutes, fluorochromes were injected. This was followed by laparotomy in preparation for intravital microscopy (IVM) of the intestine (T=2 hours). Once IVM was completed, blood and small intestine samples were collected for analysis (T=2 hours 45 minutes).

2.2.2.3 Experimental group

This model consisted of six experimental groups. Group 1, the control group, consisted of mice that underwent the same surgical and experimental interventions except for the administration of LPS. Instead, treatment vehicle (0.9 % NaCl saline) was administered. Group 2, LPS group, represents mice that received LPS (5 mg/kg) and thus had systemic inflammation but no treatment. The following groups represent treatment groups that received one of the iron chelators at T= 15 minutes. To ensure same iron chelation capacity, the dosages of the iron chelators were matched based on DIBI's iron-binding capacity (μmoles/Kg). First the clinically-approved iron chelators were studied. Groups 3, 4, 5, received LPS and DFX (2.25 mg/kg; Santa Cruz Biotechnology, Inc. Dallas, Texas, US), DFP (1.25 mg/kg; Sigma Aldrich, Missouri, US), and DFO (1.97 mg/kg; Sigma Aldrich, Missouri, US), respectively. Group 6, LPS+ DIBI, received DIBI treatment (10 mg/kg; provided by Chelation Partners Inc., Halifax, NS, Canada).

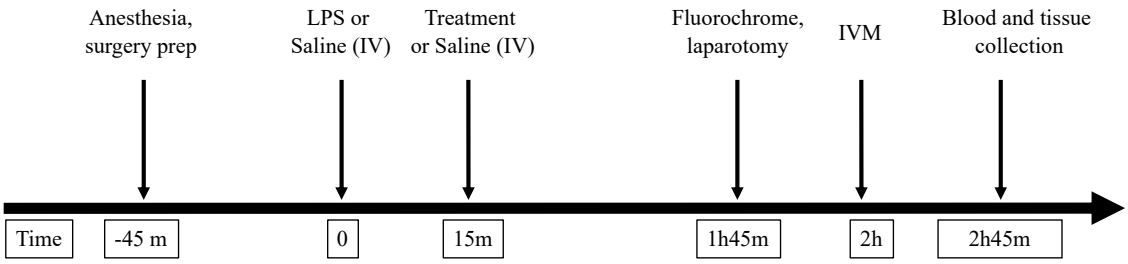

Figure 8. Experimental timeline for LPS-induced systemic inflammation model.

Table 5. Experimental groups for LPS-induced systemic inflammation model.

Model	Groups	Intervention
LPS-Induced Systemic Inflammation	1- Control	Saline IV
	2- LPS	LPS (5 mg/kg)+ IV
	3- LPS+ DFX	LPS (5 mg/kg) + DFX (2.25 mg/kg) IV
	4- LPS+DFP	LPS (5 mg/kg) + DFP (1.25 mg/kg) IV
	5- LPS+DFO	LPS (5 mg/kg) + DFO (1.97 mg/kg) IV
	6- LPS+DIBI	LPS (5 mg/kg) + DIBI (10 mg/kg) IV

2.2.3 Colon Ascendens Stent Peritonitis (CASP) model

Wildtype, male C57BL/6 mice (8-10 weeks old; 20-30 grams) were used for this model and were purchased from Charles River Laboratories International Inc. (Saint-Constant, QC, Canada) and they were housed in ventilated plastic cage racks in a pathogen free room (room tested for pathogens every three months). These mice were acclimated for one week in Carleton Animal Care Facility (CACF) of the Faculty of Medicine, Dalhousie University, Halifax, NS, Canada. They were housed in a 12-hour light/dark cycle in 21 °C room with supply of standard diet of rodent chow and filtered city water *ad libitum*.

2.2.3.1 Anesthesia and surgery

The CASP surgery was performed to induce fecal matter leakage into the abdominal cavity, causing peritonitis. Animals were anesthetized using 4 % isoflurane in oxygen (flowrate of 1 liter/hour). Depth of anesthesia was maintained by continuous inhalation of 2 % isoflurane in oxygen (flowrate 0.8 liter of oxygen/hour). Next, pre-emptive analgesia buprenorphine (short acting; 0.1 mg/kg, 0.03 mg/mL) was administered subcutaneously (SC) for post-operation pain relief and eye gel was applied.

The surgery was conducted aseptically and in accordance to Dalhousie University CACF guidelines. The abdominal region was shaved, cleaned with detergent (hibitane) and disinfectants (isopropyl alcohol 70 % solution followed by povidone-iodine). Laparotomy (midline incision) was then performed and the ascending colon was gently retracted and placed over a sterile gauze on the animal's body. A 20-gauge 1-1/4 catheter (Jelcro, Smiths Medical, Kent, UK) was securely placed at a 45° angle from the wall of ascending colon (1 cm distal to the ileocecal valve) using 7-0 polypropylene monofilament suture (3304H, Pronova ETHICON). After removing the needle, the catheter tube was cut to leave 2-3 mm of the stent projecting outside of the ascending colon. Using wet cotton-tipped applicators and gently palpating the cecum, feces filled the catheter and fecal matter entered the peritoneal cavity. To ensure the development of peritonitis (and ultimately sepsis), the stent was tightly sutured in the colon for continuous fecal matter leakage (over the next 8 hours). The ascending colon was positioned back into the abdominal cavity and the muscle layer

was sutured using 5/0 non-absorbable polypropylene monofilament (7740G, Prolene ETHICON). Before completing this suture, the treatment or vehicle (saline) was instilled over the abdominal cavity (IP). Sham surgery, for healthy control mice, was performed under the same conditions except for the catheter insertion into the ascending colon. In these animals, the catheter was sutured to the top of the outer layer of the ascending colon, with care to avoid perforation and leakage of any fecal into the abdominal cavity. All mice were given 0.5 mL saline SC for fluid replacement, kept in recovery area on heating pad 37 °C with rodent chow mash and water ad libitum. They were closely observed in the recovery room for the next six hours until it was time to be taken into the laboratory for the remainder of the experimental timeline.

2.2.3.2 Experimental Timeline

The experiment began with anesthesia induction and preparation of the mouse for CASP surgery (T= -45 minutes). During this preparation, buprenorphine was administered. Next, CASP surgery was performed to induce the peritonitis-induced sepsis. Administration of treatment/vehicle at the end of the surgery marked the T=0 timepoint. After surgery, the mice were placed in recovery area under observation as described previously. At T=6 hours 45 minutes, the mouse was anesthetized again with diluted dose of sodium pentobarbital (90 mg/kg; 54 mg/mL; 1:10 dilution in 0.9 % NaCl saline). At T= 7 hours and 30 minutes (which marked 30 minutes prior to IVM), fluorochromes (Fluorescein isothiocyanate (FITC) and Rhodamine-6G) were administered IV through tail-vein injection. Laparotomy was also performed at this time along the prior CASP surgical incision line (to reduce invasiveness). At T=7 hours 45 minutes, peritoneal lavage fluid (PLF) was collected for bacterial enumeration and microbiome analysis. IVM microscopy started at T=8 hours. Once IVM was completed, T=8 hours 45 minutes, blood and small intestine samples were collected and stored appropriately for further analysis.

2.2.3.3 Experimental groups

Six experimental groups were included in the CASP poly-bacterial model. Group 1, Sham group, served as the surgical and experimental control group. Sham animals underwent the same surgery except for the perforation of the ascending colon (absence of fecal matter

leakage). At T=0, Sham animals received vehicle as treatment (0.9 % NaCl saline). The remaining five groups had active bacterial leakage into the abdominal cavity. Group 2, CASP, represents mice that have infection but no treatment. Similar to sham, they received saline only at T=0. Groups 3 to 6 received one of the iron chelators as prophylactic treatment (T=0). To ensure same iron chelation capacity, the dosages of the iron chelators were matched based on DIBI's iron-binding capacity (μM/kg). Groups 3, 4, 5, included the clinically-approved iron chelators: CASP+ DFX (18 mg/kg), CASP+DFP (10 mg/kg), and CASP+DFO (15.76 mg/kg). Group 6, CASP+DIBI, received DIBI treatment (80mg/kg; provided by Chelation Partners Inc., Halifax, NS, Canada).

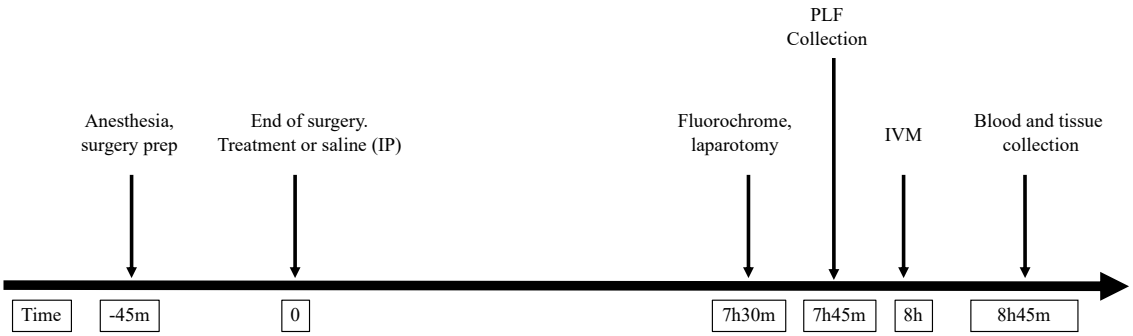

Figure 9. Experimental timeline for CASP model.

Table 6. Experimental groups for CASP model.

Model	Groups	Intervention
Colon Ascendens Stent Peritonitis (CASP)	1- Sham	Saline IP
	2- CASP	CASP (20-gauge stent)
	3- CASP+ DFX	CASP (20-gauge stent) + DFX (18 mg/kg) IP
	4- CASP+DFP	CASP (20-gauge stent) + DFP (10 mg/kg) IP
	5- CASP+DFO	CASP (20-gauge stent) + DFO (15.76 mg/kg) IP
	6- CASP+DIBI	CASP (20-gauge stent) + DIBI (80 mg/kg) IP

2.2.4 Colon Ascendens Stent Peritonitis with intervention (CASP-I)

Wildtype, male C57BL/6 mice (8-10 weeks old; 20-30 grams) were purchased from Charles River Laboratories International Inc. (Saint-Constant, QC, Canada) and they were housed in ventilated plastic cage racks in a pathogen free room (room tested for pathogens every three months). These mice were acclimated for one week in Carleton Animal Care Facility (CACF) of the Faculty of Medicine, Dalhousie University, Halifax, NS, Canada. They were housed in a 12-hour light/dark cycle in 21 °C room with supply of standard diet of rodent chow and filtered city water *ad libitum*.

2.2.4.1 Surgical intervention following CASP surgery

The CASP-I model was adapted from Traeger *et al*. (2010) where it is similar to the CASP surgery, but it is followed with an additional surgical intervention. This model mimics clinical protocol as the source of infection (catheter in the ascending colon) is surgically removed. And antibiotic, which is a standard treatment, is included in the study.

After recovery from the initial CASP surgery (as described in 2.2.3.1), the mice were monitored in the recovery room for 5 hours. They were then anesthetized with isoflurane and prepped (as described), for the second set of surgery: intervention surgery. Laparotomy was performed along the lines of the initial surgery. Once the abdominal cavity was exposed, PLF was collected. The catheter was then gently located and removed, and the hole was sutured with 7.0 size knots. The ascending colon was positioned back into the abdominal cavity and the muscle layer was sutured using 5/0 non-absorbable polypropylene monofilament (7740G, Prolene ETHICON). Before completing this suture, the second dose of treatment or vehicle was instilled over the abdominal cavity (IP). As described previously, the mice were sutured, abdominal layer closed and then mice were placed in the recovery area.

2.2.3.2 Experimental timeline

The experiment began with anesthesia induction and preparation of the mouse for the first surgery, CASP surgery (T= -45 min). CASP surgery was completed at T=0 timepoint.

Treatment/vehicle was administered IP at this time point as well. The mice were placed in the recovery area and monitored closely for few hours. At T=4 hour 30 minutes, the mice were anesthetized and prepped for the second surgery: intervention and removal of the catheter to eliminate the source of infection. Once the mouse was on the surgery table and laparotomy was performed, PLF was collected (T=4 hour 45 minutes). At T=5 hours, the second surgery was completed. It was also at this point when secondary dose of treatment or vehicle were administered IP. The mice were observed closely every 2 hours until 12 hours post-surgery. At each observation, the surface temperature and behavior of the mice were recorded. The behavioral scoring was based on murine sepsis score described by Shrum *et al*. ((183); Table 7). If the mice showed signs of distress or rapid decline in health, they were monitored more frequently even if the first 12 hours were passed. Ketoprofen was supplied at T=24 and 48 hours IP. The mice weight was recorded every 24 hours. Mice were euthanized if their MSS score reached 15, more than 15 % weight loss, or other animal welfare concerns were raised. All surviving mice were sacrificed on day 7 (T=168 hours).

Table 7. Murine sepsis score as described by Shrum et al (183).

Variable	Score and Description
Appearance	0- Smooth coat 1- Patches of piloerected hair 2- Majority of back piloerected 3- +/- piloerection, puffy mouse 4- +/- piloerection, emaciation
Level of consciousness	0- Active 1- Avoids upright standing 2- Slow but ambulant 3- Impaired movement when provoked, tremors 4- Stationary when provoked, possible tremor
Activity	0- Normal 1- Slightly suppressed 2- Stationary with occasional investigation 3- Stationary 4- Stationary with hind leg tremors
Response to stimulus	0- Immediate response 1- Slow or no response to sound, strong response to touch 2- No response to sound, moderate response to touch 3- No response to sound, mild response to touch (no locomotion)
Eyes	0- Open 1- Not fully open, possible secretions 2- Half closed, possible secretions 3- More than half closed, possible secretions 4- Closed or milky
Respiration rate	0- Normal 1- Decreased but not quantifiable 2- Moderately reduced and just quantifiable 3- Severely reduced and easily quantifiable (>0.5s) 4- Extremely reduced (>1s)
Respiration quality	0- Normal 1- Periods of laboured breathing 2- Laboured 3- Laboured with intermittent gasps

2.2.4.3 Experimental groups

Six experimental groups were included in the CASP-I model. Group 1, Sham-I group, served as the surgical and experimental control group. Sham-I animals underwent the same surgeries except for the perforation of the ascending colon (absence of fecal matter leakage). At T=0 hour and T=5 hours, Sham-I animals received vehicle as treatment (0.9 % NaCl saline) injected IP. The other five groups initially had active bacterial leakage into the abdominal cavity which was attended to by removing the catheter in the interventional surgery. Group 2, CASP-I, represents mice that had infection but no treatment. Similar to sham-I, they received only saline at T=0 hour and T=5 hours. Group 3, CASP-I+IMI, received single dose of imipenem antibiotic (IMI; 25 mg/kg; Ranbaxy Pharmaceuticals Canada Inc., Mississauga, ON, Canada) at T=0 hour. Group 4, CASP-I+DIBI, received a single dose of DIBI (80 mg/kg) at T=0 hour. Group 5, CASP-I+IMI+DIBI, received single dose of DIBI and imipenem at T=0 hour. Group 6, CASP+IMI+$DIBI_2$, received single dose of imipenem at T=0 hour and two individual doses of DIBI at T=0 hour and T=5 hours.

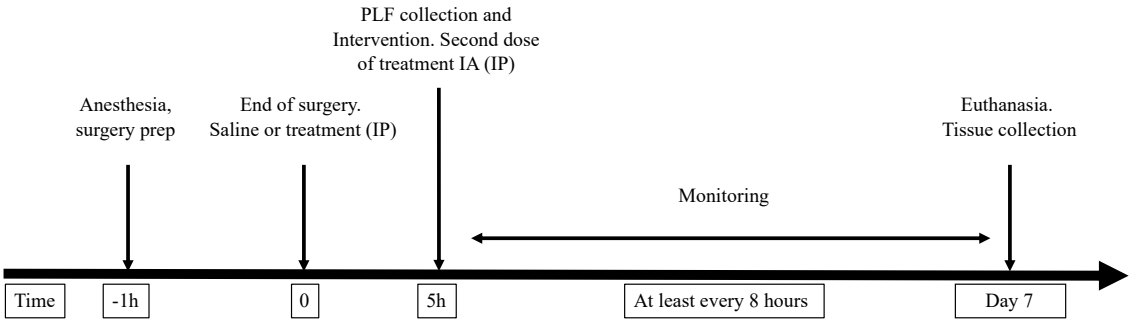

Figure 10. Experimental timeline for CASP-I model.

Table 8. Experimental timeline for CASP-I model.

Model	Groups	Intervention
Colon Ascendens Stent Peritonitis with Intervention (CASP-I)	1- Sham-I	Saline IP
	2- CASP-I	CASP-I (20-gauge)
	3- CASP-I+DIBI	CASP-I (20-gauge) + DIBI (80 mg/kg) IP
	4- CASP-I+IMI	CASP-I (20-gauge) + IMI (25 mg/kg) IP
	5- CASP-I+IMI+DIBI	CASP-I (20-gauge) + IMI (25 mg/kg) + DIBI (80 mg/kg) IP
	6- CASP-I+IMI+$DIBI_2$	CASP-I (20-gauge) + IMI (25 mg/kg) + DIBI (80 mg/kg twice) IP

2.2.5. Intravital microscopy (IVM)

2.2.5.1 Preparation before microscopy

Animals are anesthetized prior to fluorochrome administration (using sodium pentobarbital). Fluorochromes are administered 15 minutes before scheduled IVM time. Rhodamine-6G (1.5 mL/kg; Sigma-aldrich, ON, Canada) stains mitochondria of cells and thus helps with visualization of leukocytes. 5% flourescein isothiocyanate-bovine serum albumin (FITC-BSA; 1 mL/kg; Sigma Aldrich, Oakville, ON, Canada) visualizes microvasculature and perfusion as it remains in plasma. The stains were prepared using sterile saline at 0.05 % and 5 % concentrations, respectively. They were administered IV, through catheter in systemic-inflammation model and through the tail vein in the CASP model, 15 minutes prior to scheduled IVM time.

Next, laparotomy was performed by making a midline incision on a clean and shaven abdomen. The underlying abdominal tissue was cut at the linea alba, to minimize bleeding. Once the abdominal cavity was exposed, section of terminal ileum was carefully extracted. The mouse was positioned on its side and about 2 cm of terminal ileum was place on the mouse microscopic viewing stage. The exposed part of the intestine was perfused with warm saline (5 mL/hour) through the entire procedure (37 °C; 0.9 % NaCl). This was done to prevent the tissue from dying, being damaged, and to create a more physiologically comparable environment. Mouse body heat and temperature were also maintained as the IVM stage was placed over a heating pad.

2.2.5.2 Microscopy

IVM microscopy was performed by using an epifluorescence microscope (Leica DMLM, Wetzlar, Germany) and a light source (LEJ EBQ 100; Carl Zeiss, Jena, Germany). Four anatomical environments were studied in the exposed intestinal section: V1 collecting venules, V3 post-capillary venules, muscle layer, and mucosal layer. V1 collecting venules, were 70-100 μm in vessel diameter and were usually located next to an arteriole. V3 post-capillary venules were smaller, 25-45 μm in vessel diameter, and are not accompanied by an arteriole. Muscle layers consisted of circular and longitudinal arrangement of

microcirculation capillaries. Mucosal villi were viewed by using a cauterizer to gently separate the intestine lengthwise. For each anatomical site, six visual fields were selected randomly. Leukocyte-endothelial interactions in the V1 and V3 vessels (rolling and adhering leukocytes) and perfusion in muscle layer and mucosal villi (functional capillary density) were analyzed. These visual fields were recorded for 30 seconds (real-time); image capture of these IVM videos are presented in Figure 11. Using Volocity software (Perkin Elmer, Waltham, MA, USA), the videos were captured using a digital EM-CCD camera C9100-02 with AC-adapter A3472-07 (Hamamatsu, Herrsching, Germany). Once IVM was successfully completed, the mouse was euthanized via cardiac puncture and samples were collected. Video analysis was performed offline, blindly, using ImageJ software (version 2.0.0-rc-69/1.52p, National Institute of Health, USA).

2.2.5.3 Offline video analysis

For V1 and V3 analysis of leukocyte-endothelial interactions, the region of interest was determined based on the biggest area that was in focus for the entire video duration. Leukocyte adhesion was defined as leukocytes that remained immobile on the endothelial surface within the pre-measured area (under the assumption of cylindric area) for the full duration of the video (adhering cells/mm^2). Leukocyte rolling was defined as non-adherent leukocytes that moved through the vessel cross-section (number of rolling cells/minute). For muscle layer analysis of microcirculatory perfusion, the biggest rectangular cross section in focus was selected as the region of interest. Functional capillary density (FCD) was selected to define the microcirculatory perfusion: total length of all perfused vessels in the region of interest were divided by the total area selected (cm/cm^2). For the mucosal villi, 5-6 villus in focus were selected for analysis.

2.2.6 Blood & Plasma Collection

Under deep anesthesia, cardiac puncture was performed with a heparin-coated 25-gauge needle on 1 mL syringe (heparin: 1000 USP units/ml; Sandoz Canada Inc. Boucherville, QC, Canada). If blood was needed for bacterial enumeration, a small volume was stored separately for plating. Next, blood was centrifuged, plasma was removed, and stored at -80 °C for further analysis.

2.2.7 Plasma inflammatory mediators and adhesion molecules measurements

Plasma cytokine and chemokine levels were measured using a custom-made magnetic Bio-Plex Pro cytokine, chemokine, and growth factor assay from Bio-Rad (Mississauga, ON, Canada). This assay uses sandwich ELISA technique with magnetic beads to quantify the level of the following analytes: TNF-α, IL-1, IL-6, IFN-γ, IL-10, soluble intercellular adhesion molecule-1 (sICAM-1), and soluble P-selectin (sP-selectin). Samples were prepared in 3-fold dilutions and technical duplicates were included in the analysis. Briefly, 50 µL of detection antibody magnetic beads were added to each well of a flat-bottom 96-well plate. They were then washed with Bio-Plex Pro wash buffer. Prepared standards and samples were loaded on to the plate and allowed to incubate in the dark on the shaker at 300 revolutions per minute (RPM) for 1 hour. Following a wash step, Bio-Plex detection antibodies were loaded onto the plate and incubated in the dark on shaker for 30 minutes. After a wash step, Streptavidin-PE was added to wells for the final incubation on the shaker for 10 minutes in the dark. Following a final wash, the plate was loaded on the Bio-Rad 200 luminometer. Bio-Plex manager software was used to read plate. Using the standard curve from the kit, the analytes levels were calculated.

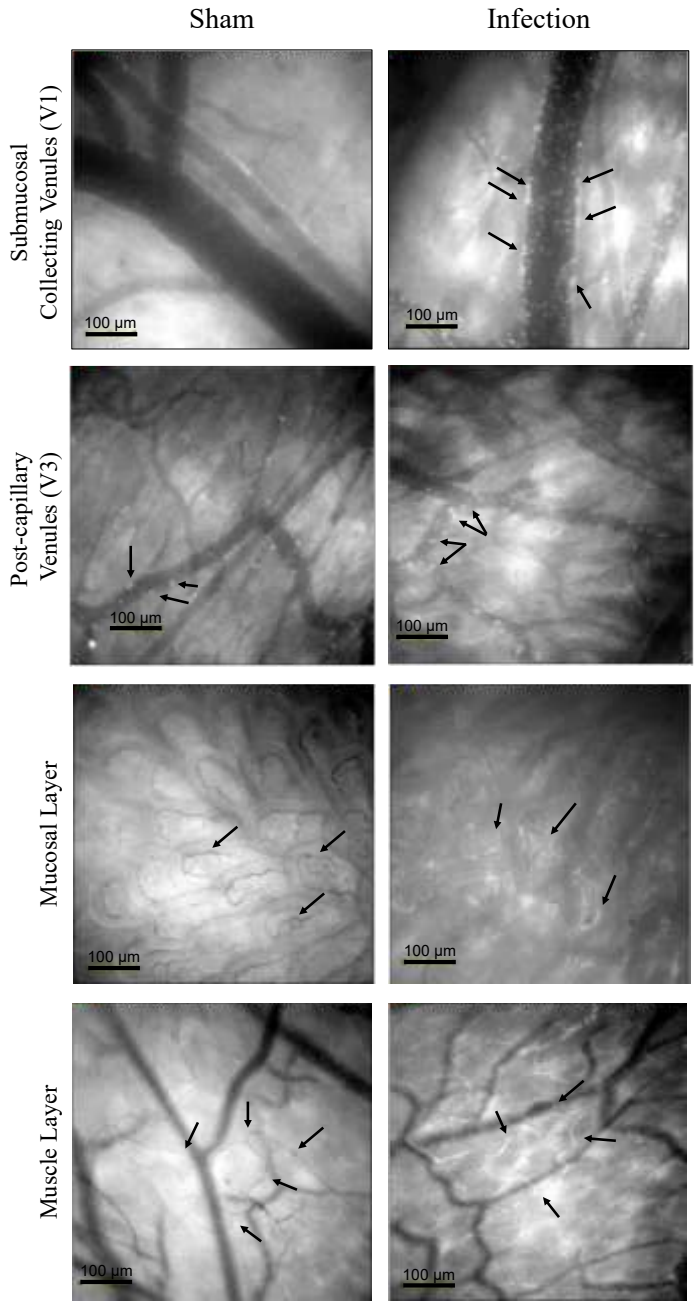

Figure 11. Image captures of intestinal intravital microscopy videos observed in control and experimental sepsis.

Within the submucosal collecting venules (V1) and post-capillary venules (V3) arrows indicate low number of rolling leukocytes in control animals, whereas high numbers of firmly adhering leukocytes are present in animals with sepsis. In the mucosal and muscle layers arrows indicate perfused capillaries (which appear as black lines) in control, and non-perfused capillaries (which appear as white lines) in sepsis.

2.2.8 Intestinal tissue collection and histology

After euthanasia, a section of terminal ileum was excised and fixed in 10 % phosphate-buffered formalin (EK Industries, Joliet, IL) for a minimum of 48 hours. This sample was incubated in 70 % ethanol prior to processing. Next, it was placed in paraffin blocks using automated tissue processor (Leica microsystems Inc., Richmond Hill, ON, Canada) and was sliced in 5 µm sections using microtome (Jung AG, Heidelberg, Germany). Using blinded histological staining, the samples were stained with hematoxylin and eosin (H&E) and evaluated by light microscopy. The degree of histological damage was assessed by a score developed by Chiu (184): 0= normal histology; 1= Subepithelial space at villus tips; 2= extension of sub epithelial space with moderate lifting, and epithelial cell loss and injury at the villus tip; 3= massive lifting down sides of villi, some denuded tips; and 4= denuded villi, dilated capillaries, and damage extending to more than one-half of villi; 5= disintegration of lamina propria. Histological assessment of intestinal samples obtained from this research are represented in Figure 12; the highest morphological damage observed was grade 3 damage.

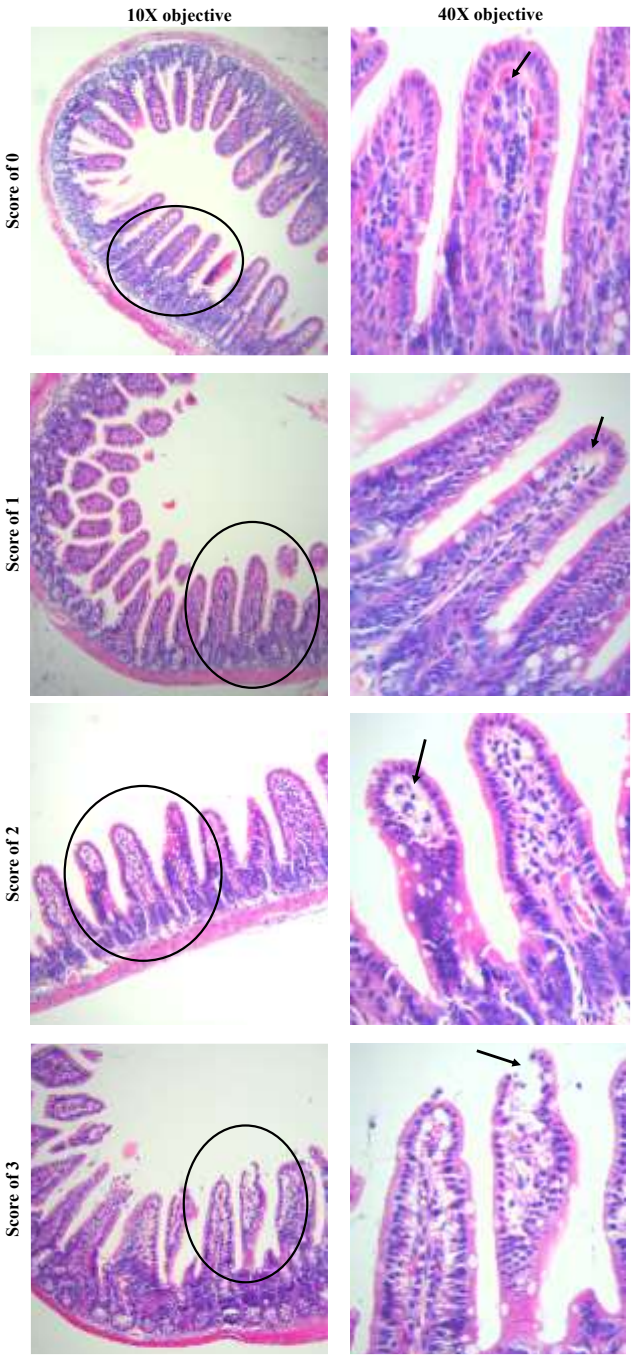

Figure 12. Histological representation of intestinal damage observed with Chiu Score.

The Chiu score was used to assess morphological damages in the experiments (184). Murine intestinal samples were fixed, embedded in paraffin, and stained with H&E. The images represent scores that were assigned to the representing tissue damage during infection. Score of 0= normal mucosal villi with intact epithelial cells; 1= Subepithelial space (Gruenhagen's space) at apex of villi; 2= extension of sub epithelial space; 3= massive lifting down sides of villi, some denuded tips.

2.2.9 Peritoneal lavage fluid (PLF)

2.2.8.1 PLF collection

PLF was collected by first performing laparotomy and instilling 2 mL of pre-warmed sterile saline into the abdominal cavity. The saline was gently mixed with the peritoneal fluid and content. Average of 1.5 mL volume of PLF was collected for bacterial enumeration and microbiome composition analysis.

2.2.9.2 PLF Microbiome Sequencing

PLF sample (500 µL) were used to assess the relative proportions of the bacteria. For microbiome profiling 16S Bacteria and Archaea Standard Operating Procedure was used, as described in detail by Comeau *et al.* (185). In short, 16S gene fragments were extracted and quantified from samples by PCR. The samples were analyzed in duplicates using two sets of forward and two sets of reverse primers at 1:1 and 1:10 dilutions, alongside four negative PCR controls. The duplicate PCRs were then combined in one plate and visually verified by running an E-gel. The amplicons were cleaned up and normalized using high-throughput Invitrogen SequelPrep 96-well plate kit. The samples along with negative control were pooled to create a library. The library was quantified by utilizing Invitrogen Qubit double-stranded DNA high-sensitivity fluorescence-based method and followed by Illumina MiSeq sequencing.

2.2.10 Bacterial Counting

Blood (CASP) and PLF (CASP and CASP-I) samples (50 µL) were used for bacterial enumeration. Aseptic technique and sterile tools were employed. For CASP experiments, sterile 1X PBS was used to make serial dilutions (1:1x10 to $1:1x10^6$) that were plated on tryptic soy agar plates (TSA; Millipore Sigma, Etobicoke, Ontario, Canada) using triplicate spot method. For CASP-I experiments, two sets of TSA plates and two sets of MacConkey plates (Millipore Sigma, Etobicoke, Ontario, Canada) were prepared. One set of TSA and MacConkey plates were incubated at 37 ^{o}C under aerobic conditions. The other set of TSA and MacConkey were incubated using anaerobic jar and GasPak (BD., Franklin Lakes, NJ,

USA) under anaerobic conditions. The plates were counted after 16-24 hours to determine the colony-forming units (CFU) per mL (CFU/mL). Row of spots were only enumerated when distinct and clear colonies were observed (~ 30 colonies per spot). CFU/mL were calculated by taking the mean value obtained from the triplicates spots and multiplying it by the dilution factor.

2.3. Statistical analysis

Data were analyzed using the GraphPad Prism 8 software (version 8.2.0 272; La Jolla, CA, USA). Normality distribution was confirmed by Kolmogorov-Smirnov test. Normally distributed data was analyzed using unpaired t tests, or one-way ANOVA followed by the Newman-Keuls test for comparison of three or more groups. Non-parametric data was analyzed using either the Mann-Whitney Test or the Kruskal-Wallis Test. Survival data was analyzed using the Mantel-Cox (Log Rank) test. Plasma, supernatant, and PLF samples analyses were performed in technical duplicates. The cytokine levels in CF supernatants were normalized to their protein content. Data was expressed as a mean value ± standard deviation (SD). Significance was assumed at $P<0.05$.

CHAPTER 3: RESULTS

3.1 Inflammation

To study the impact of iron chelation during inflammation, LPS was used to induce an immune response in *in vitro* and *in vivo*. Neutrophils were treated *in vitro* with DIBI to measure changes in their intracellular labile iron pool (ILIP). Mice were treated with one of the four iron chelators of interest to study whole-organism impact of iron chelation.

3.1.1 Measurement of ILIP in bone-marrow derived neutrophils

DIBI has been proven to lower oxidative stress in macrophages and neutrophils (186). Additionally, it was shown to lower ILIP in RAW 264.7 macrophage-like cell line (unpublished data from Hoskin Laboratory). However, neutrophils' response to DIBI regarding impact on ILIP was not investigated yet. Given the importance of these cells in innate immunity and acute inflammation, we were interested in observing changes in ILIP in response to DIBI. To study this, we performed CA-AM assay.

To set the experimental model, LPS 100 ng/mL dose was selected for stimulation of neutrophils as it has previously been shown to effectively activate TLR4 and induce a pro-inflammatory response, including increase in IL-6 secretion and respiratory burst (186–189). DIBI treatment dose of 200 μM had been tested previously *in vitro* in neutrophils and macrophages ((183) and unpublished data from Hoskin Laboratory), where DIBI reduced LPS-induced ROS, NO, and IL-6 levels. Thus DIBI 200 μM dose was selected for analysis *in vitro*. We hypothesized that DIBI (200 μM) can mobilize ILIP to the extracellular environment. In order to observe potential difference with lower degree of iron chelation, DIBI dose of 25 μM was also included in this study.

Bone marrow derived neutrophils were incubated in treatment (medium, LPS, DIBI, or LPS+DIBI) for four hours followed by CA-AM staining. CA-AM is hydrolyzed to florescent calcein, which in turn quenches iron, and fluorescence intensity (FI) is inversely correlated to the ILIP. FI was measured by flow cytometry. FI is inversely correlated to the ILIP.

Neutrophils treated with DIBI doses of 25 μM (D25) and 200 μM (D200) had no change in the mean FI levels from control level (Figure 13). Upon LPS-incubation of the neutrophils (LPS; 100 ng/mL), the FI levels remained unchanged from control level. Similarly, LPS incubation and DIBI 25 μM treatment (LD25) showed no significant changes in the FI. However, incubation of the neutrophils with LPS and DIBI 200 μM (LD200) increased the FI from LPS group; this finding was statistically significant when analysis was done using a two-tailed T test.

These results demonstrated that only when neutrophils are incubated in LPS and treated with the higher dose of DIBI (200 μM), the ILIP is reduced from control levels. This suggests that when extracellular iron is chelated in higher magnitude, intracellular iron is mobilized by neutrophils. Based on this finding, we were interested in studying neutrophils behaviour in LPS-induced inflammation in a whole organism such as mouse model.

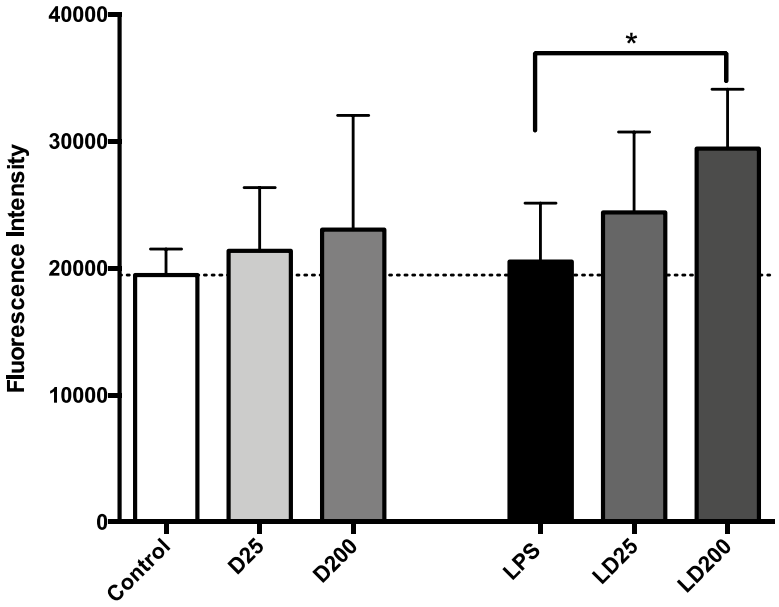

Figure 13. Assessment of intracellular labile iron pool in bone marrow derived neutrophils by CA-AM assay.

Neutrophils were isolated from bone marrow, treated with LPS (100 ng/mL), DIBI (25 or 200 μM), or media alone for four hours. At the end of the incubation, cells were harvested, and stained with 0.15 μM CA-AM for 30 minutes. Fluorescence intensity (FI) was measured via flow cytometry. The dashed line denotes FI of control (media-only) cells. Data is presented as arithmetic mean FI ± SD, (n=3-4 per group); * $p < 0.05$ compared to LPS-treated cells, as determined by a two-tailed T test. D25= DIBI 25 μM; D200= DIBI 200 μM; LPS= Lipopolysaccharide, 100 ng/mL; LD25= LPS and DIBI 25 μM; LD200= LPS and DIBI 200 μM.

3.1.2 Assessing immune activation in a LPS-induced model of systemic inflammation

We were interested to assess iron chelation's ability to alter immune activation *in vivo*. Mice received an IV administration of LPS (5 mg/kg) followed, 15 minutes later, by a treatment consisting of one of the iron chelators: DFX (2.25 mg/kg), DFP (1.25 mg/kg), DFO (1.97 mg/kg), or DIBI (10 mg/kg). IVM of the intestine was used to assess the treatment effect on leukocyte-endothelial interactions and capillary blood flow.

3.1.2.1 Leukocyte-endothelial interaction

During inflammation, rolling and adhesion are critical for successful transmigration of leukocytes to the site of inflammation. Pro-inflammatory mediators upregulate the expression of adhesion molecules on the surface of both immune and endothelial cells. Leukocyte adhesion was selected as the primary endpoint to measure as these firmly adhering leukocytes have completed 2 stages of the extravasation process.

In the control group, we observed a low number of adhering leukocytes in the V1 (collecting) venules (Figure 14, Part A). This low level of activation is most likely due to the invasive experimental procedure and local surgical stress that release inflammatory mediators and initiate an inflammatory response. As expected, when the mice were stimulated with LPS, there was a significant increase in the number of adhering leukocytes, indicating the presence of systemic inflammation. Treatment with DFP, DFO and DIBI were able to significantly reduce the LPS-induced leukocyte adhesion. Interestingly, DIBI treatment restored leukocyte adhesion to control levels. V3 (post-capillary) venules had a higher degree of basal leukocyte adhesion, as compared to V1 venules (Figure 14, Part B). LPS administration did not change the number of adhering leukocytes from control levels. However, treatment with DFX, DFP, and DFO increased leukocyte adherence significantly from control and LPS levels. On the other hand, DIBI treatment did not change the leukocyte adhesion from both control and LPS groups.

In summary, DFP, DFO, and DIBI were able to reduce leukocyte adhesion within the V1 venules. In V3 venules, all three classical iron chelation increased leukocyte adhesion

levels while DIBI treatment did not change the levels of leukocyte adhesion. These findings highlight iron chelation's impact on modulating the leukocyte-endothelial interactions.

Next, we were interested in iron chelation's effect on the preceding step in leukocyte extravasation: leukocyte rolling. In this stage, the leukocytes bind to vascular endothelium with low affinity and have a rotational motion on the endothelium surface. In V1 venules, the control group demonstrated a high number of rolling leukocytes (Figure 15, part A), which decreased significantly with LPS administration. The number of rolling leukocytes remained low and did not change with any of the iron chelation treatment. Similar results were observed in the V3 venules (Figure 15, part B). In summary, iron chelation was not able to restore the number of rolling leukocytes in LPS-stimulated mice to control levels. This suggests that iron chelators impact the leukocyte-endothelial interaction at the adhesion stage, and not at the rolling stage.

3.1.2.2 Capillary blood flow

Given the importance and sensitivity of microcirculatory changes in systemic inflammation and sepsis pathology, it was of interest to explore the effect of iron chelation on capillary perfusion.

Functional capillary density (FCD) of the muscle and the mucosal villi of the intestine were recorded. LPS-induced systemic inflammation significantly reduced FCD in both layers when compared to the control group (Figure 16, A and B). All iron chelation treatments (DFX, DFP, DFO, and DIBI), were able to significantly improve the FCD from LPS level. This observed FCD improvement highlights iron chelation's ability to restore FCD levels back to control levels, as there were no statistical differences between iron chelation treatment groups and control levels.

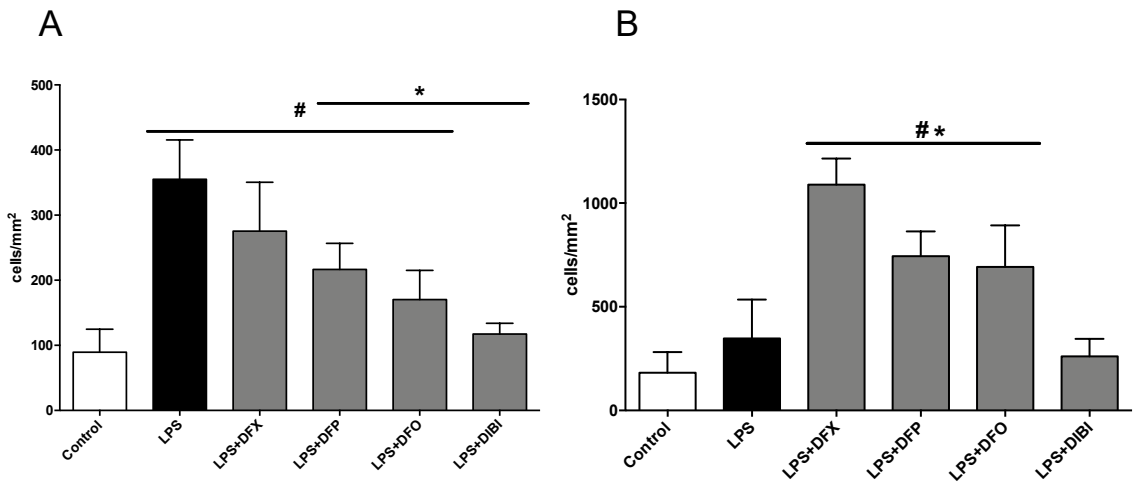

Figure 14. Effect of iron chelation on leukocyte adhesion in V1 and V3 venules in systemic inflammation.

Bar graphs represent firmly adherent leukocytes in the intestinal A) submucosal collecting venules, V1 and B) post-capillary venules, V3 (cells/mm^2) two hours after systemic administration of LPS (5 mg/kg). Treatment, one of the iron chelators, was administered 15 minutes following LPS administration: DFX (2.25 mg/kg), DFP (1.25 mg/kg), DFO (1.97 mg/kg), DIBI (10 mg/kg). Data represented as mean ± SD (n= 4-6 per group); # $p < 0.05$ compared to control group, * $p < 0.05$ compared to LPS group. DFP: Deferiprone; DFO: Deferoxamine; DFX: Desferasirox; LPS: Lipopolysaccharide.

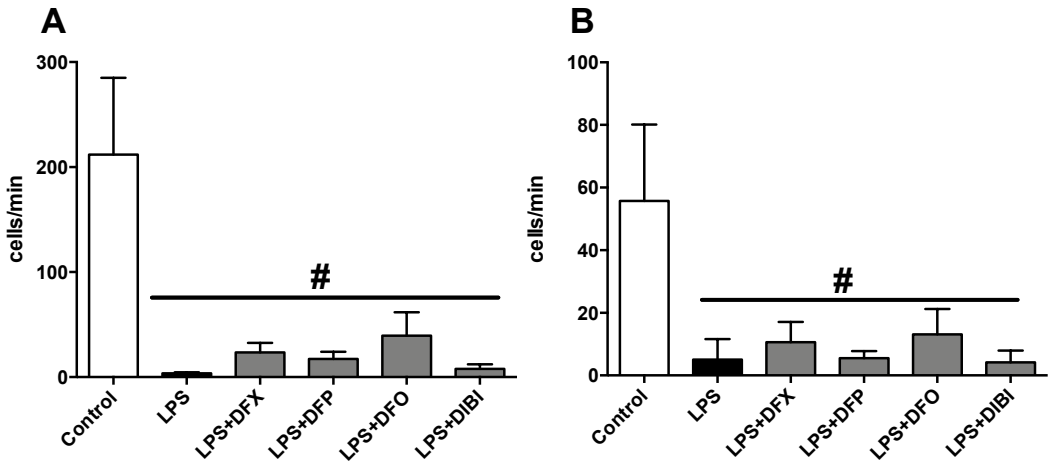

Figure 15. Effect of iron chelation on leukocyte rolling in V1 and V3 venules in systemic inflammation.

Bar graphs represent leukocyte rolling in the intestinal A) submucosal venules, V1 and B) post-capillary venules, V3 (cells/min) two hours after systemic administration of LPS (5 mg/kg). Treatment, one of the iron chelators, was administered 15 minutes following LPS administration: DFX (2.25 mg/kg), DFP (1.25 mg/kg), DFO (1.97 mg/kg), DIBI (10 mg/kg). Data represented as mean ± SD (n=4-7 per group); #$p < 0.05$ compared to control group. DFP: Deferiprone; DFO: Deferoxamine; DFX: Desferasirox; LPS: Lipopolysaccharide.

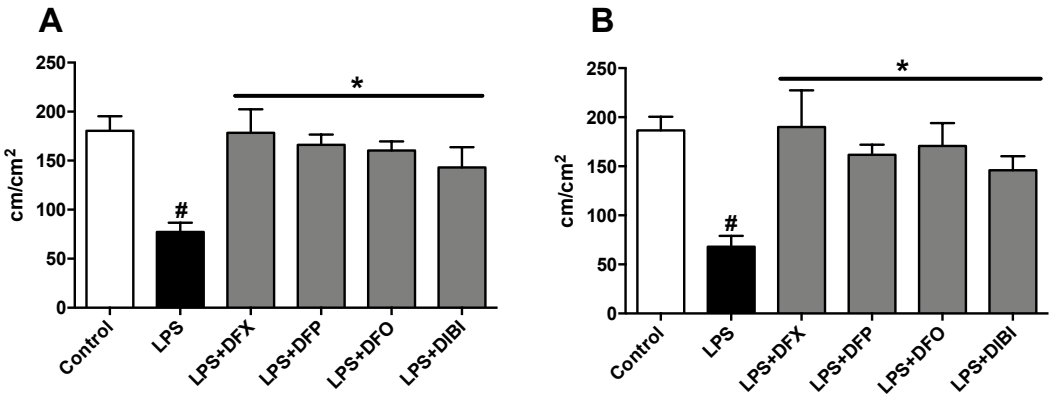

Figure 16. Effect of iron chelation on intestinal capillary blood flow in systemic inflammation.

Bar graphs represent the functional capillary density in the A) muscle and B) mucosal villi layer two hours after systemic administration of LPS (5 mg/kg). Functional capillary density was calculated as following: total length of all perfused vessels in the region of interest divided by the total area selected (cm/cm^2). Treatment, one of the iron chelators, was administered 15 minutes following LPS administration: DFX (2.25 mg/kg), DFP (1.25 mg/kg), DFO (1.97 mg/kg), DIBI (10 mg/kg). Data represented as mean ± SD (n= 4-8 per group); # $p < 0.05$ compared to control group, * $p < 0.05$ compared to LPS. DFP: Deferiprone; DFO: Deferoxamine; DFX: Desferasirox; LPS: Lipopolysaccharide.

3.1.2.3 Plasma inflammatory mediators

As a result of acute inflammatory response, immune and structural cells release cytokines and chemokines in the blood, which can induce surface protein and receptor expression. These proteins can be detected in the plasma. Therefore, to further explore the inflammatory mediators contributing to the LPS-induced systemic inflammatory response, plasma samples were collected two hours and 45 minutes after LPS administration. The plasma samples were analyzed by Bio-plex multiplex immunoassay.

TNF-α is one of the earliest pro-inflammatory cytokines to be released during an inflammatory response. This short living cytokine's level peaks early during the acute phase response. As expected, control animals had minimal TNF-α levels (Figure 17, part A), and LPS administration significantly increased TNF-α levels when compared to the control group. None of the treatment groups reduced the TNF-α release induced by LPS. On the contrary, DIBI treatment showed a higher release of TNF-α levels when compared to LPS-level as determined by a Student's t-test.

Similar to TNF-α secretion, IFN-γ levels rise early and rapidly during an inflammatory response. We observed no changes to IFN-γ levels in the LPS group, compared to the control group (Figure 17, part B). However, in the DFX, DFP, and DFO treatment groups, there was a significant increase in IFN-γ secretion when compared to both LPS and control levels. On the other hand, DIBI treatment did not show the same pattern of response and did not change the IFN-γ levels from the levels observed in the LPS group.

IL-1β is a pyrogenic cytokine that is produced by immune cells. During the inflammatory response, its levels are associated with increased inflammation severity (80). In this study, although not significantly different from the control group levels, IL-1β levels appeared to increase after LPS administration (Figure 17, part C). Iron chelation treatments showed different responses. However, there was no statistically significant change in IL-1β levels, as compared to LPS group.

IL-6 has pro- and anti-inflammatory effects, playing an important role in orchestrating the adaptive response and initiating the healing process in epithelial cells (190). Overall, IL-6 secretion showed a similar course to IFN-γ. IL-6 levels were minimal in the control group (Figure 17, part D), and LPS did not change the IL-6 levels from control. In DFX, DFP, and DFO treatments, there was a significant increase in IL-6 secretions compared to LPS group, meanwhile DIBI did not change the levels from LPS group.

Once an inflammatory response is initiated, it is important to activate the complementary anti-inflammatory pathways to assist the inflammation resolution and healing. IL-10, is an anti-inflammatory cytokine that plays a role in this process. In our model at the measured time point, there were no significant differences between control and LPS IL-10 levels (Figure 17, part E). DFX and DIBI treatments induced significantly higher IL-10 secretions when compared to control group, but not significantly different from the LPS group ($p= 0.12$).

As cited before, inflammatory mediators increase the expression of adhesion molecules. ICAM-1 is a surface glycoprotein expressed on endothelial cells. In our plasma samples, levels of soluble (s) ICAM-1 which were shed in the plasma were measured. In LPS group, there was only a non-significant increase in sICAM-1 levels compared to control (Figure 17, part F). However, in DFX, DFO, DFP treatments, there was a significant increase in sICAM-1 from the levels of both LPS and control groups. DIBI treatment was similar to control and LPS levels. P-selectin is expressed by endothelial cells to allow leukocytes to tether and begin rolling. There were no differences between the studied groups for soluble (s) P-selectin plasma levels (Figure 17, part G).

Overall, these results indicate that LPS did not statistically increase the level of the studied plasma mediators, except for TNF-α. Iron chelation treatments had variable effects on the secretion of the mediators: DIBI treatment had similar effect on inflammatory mediators release than LPS, except for TNF-α where DIBI increased its levels from LPS group. DFO, DFP, and DFX increased IFN-γ, IL-6, and sICAM-1 levels.

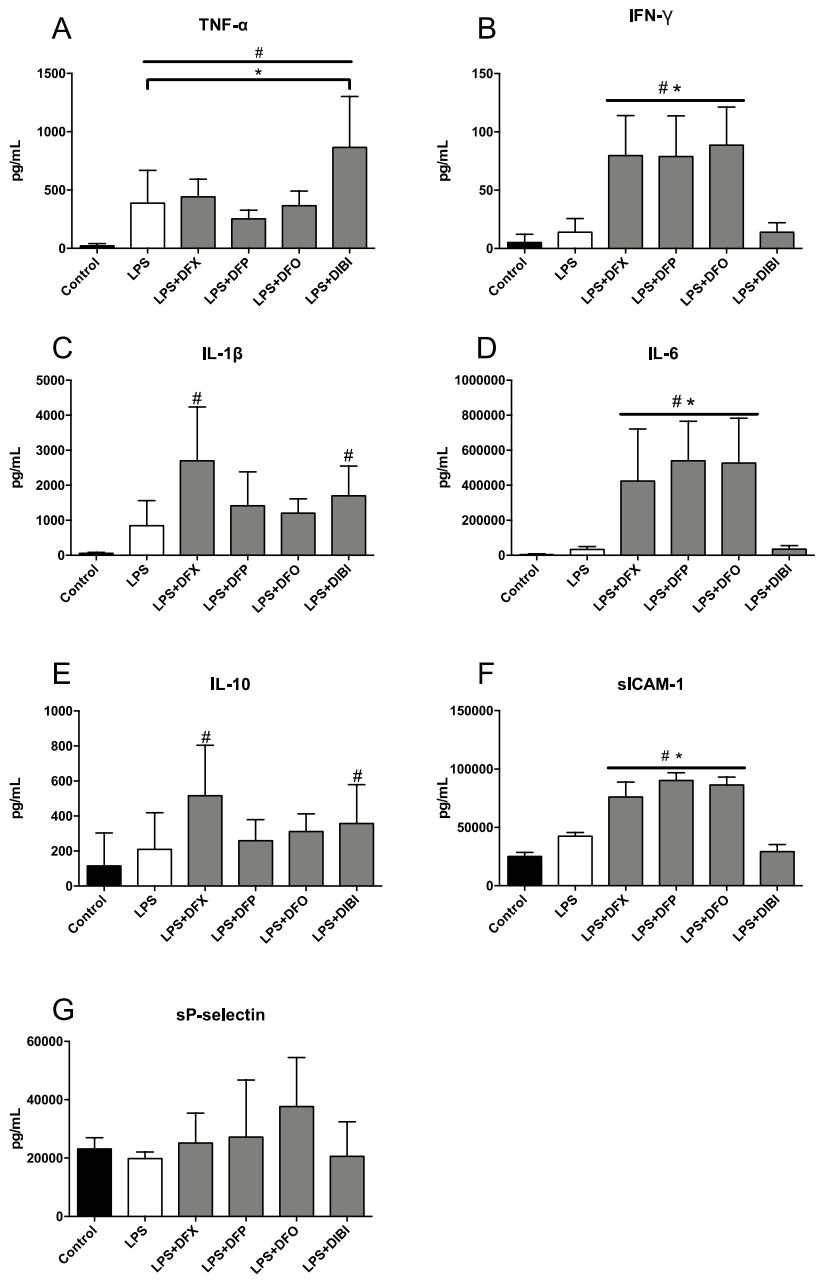

Figure 17. Effects of iron chelation on plasma inflammatory mediators in systemic inflammation.

Samples were taken 2 hours and 45 minutes after systemic LPS administration (5 mg/kg). Treatment, one of the iron chelators was administered 15 minutes following LPS administration: DFX (2.25 mg/kg), DFP (1.25 mg/kg), DFO (1.97 mg/kg), DIBI (10 mg/kg). Bar graphs represent mean cytokine values ± SD (n = 4-9 per group); # $p < 0.05$ compared to control group; * $p < 0.05$ compared to LPS. Deferiprone; DFO: Deferoxamine; DFX: Desferasirox; IFN: interferon; IL: interleukin; LPS: Lipopolysaccharide; TNF: tumor necrosis factor; sICAM-1: Soluble intercellular adhesion molecule-1; sP-selectin: soluble P-selectin.

3.1.2.4 Histology

In order to assess potential intestinal tissue damage, intestinal samples were collected two hours and 45 minutes after LPS-administration. The samples were processed for morphological damage by using the Chiu score as described in Figure 12.

There was variability amongst and within the treatment groups (Figure 18). Surprisingly, in control animals, there were mild histological damages present. LPS administration was not able to induce significant further intestinal damage during the observation time. None of the iron chelation treatments were able to modulate that change.

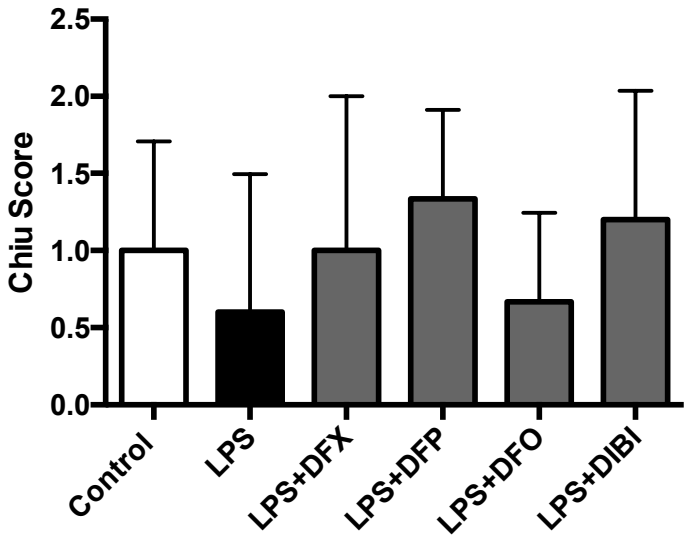

Figure 18. Effects of iron chelation on morphological changes within the intestinal mucosal tissues.

Samples were taken two hours and 45 minutes after systemic LPS administration (5 mg/kg). Treatment, one of the iron chelators was administered 15 minutes, following LPS administration: DFX (2.25 mg/kg), DFP (1.25 mg/kg), DFO (1.97 mg/kg), DIBI (10 mg/kg). Samples were collected post-mortem, fixed, and embedded in paraffin. Tissue sections were stained with H&E. Bar graphs represent mean Chiu score ± SD (n=3-5 animals). DFP: Deferiprone; DFO: Deferoxamine; DFX: Desferasirox; LPS: Lipopolysaccharide.

3.2 Infection

To understand how iron chelation impacts the inflammatory response during an infection, the CASP model was selected. In this dynamic model of poly-bacterial sepsis, fecal matter leakage into the abdominal cavity induces peritonitis. This model is highly regarded as a model of sepsis as it mimics the clinical progression of sepsis and the heterogeneity of infection severity as the amount of leakage is uncontrolled. Additionally, this model provides the opportunity to test the anti-bacterial properties of iron chelation. For this reason, the CASP model was selected to compare DIBI with the other iron chelators. The timeline of this model was adapted from a previous study (191) and the dosing strategy was based on dose-response studies (186). In the next model, CASP-I, an intervention surgery was performed after five hours to remove the infection source (stent in the ascending colon). Antibiotic therapy with imipenem was included to simulate standard clinical treatment.

3.2.1 Colon ascendens stent peritonitis (CASP)

In the CASP model, the inflammatory state of mice was assessed by observing leukocyte-endothelial interactions, effects on capillary blood flow, and measuring plasma levels of pro- and anti-inflammatory mediators. Additionally, peritoneal bacterial burden and composition was assessed by measuring bacterial growth in peritoneal lavage fluid (PLF), blood, and microbiome analysis. Histological assessment was performed to study the morphological changes in the small intestine.

3.2.1.1 Leukocyte-endothelial interaction

Since infection severity and inflammatory response are related, we were interested in studying the leukocyte-endothelial interactions by IVM of the intestine, performed eight hours after completion of CASP surgery.

Starting with our primary endpoint, leukocyte adhesion in V1 venules, the sham group, had a relatively low number of adhering leukocytes (Figure 19, part A). As expected, the number of adhering leukocytes significantly increased following CASP procedure: all

animals that underwent CASP surgery showed significantly increased numbers of adhering leukocytes compared to sham animals. Iron chelation treatment with DFP, DFO, and DIBI significantly lowered the number of adhering leukocytes, as observed when compared to untreated CASP animals. This result was consistent with what had been observed in the LPS-induced systemic inflammation model. DFX treatment was not effective in reducing the numbers of adherent leukocytes. In regard to the rolling leukocytes, highest numbers were observed in the sham group (Figure 19, part B). Consistent with previous observation in systemic inflammation, animals with sepsis had significantly lower numbers of rolling leukocytes than sham animals. However, there were no differences observed between untreated CASP and iron chelation treated CASP groups.

In the V3 venules, the numbers of adhering leukocytes in the sham group were relatively high as compared to the sham group in V1 vessels (Figure 20, part A). Induction of sepsis (CASP) caused a significant increase in the leukocyte adherence when compared to sham group, and none of the treatments with the iron chelators were able to cause a significant reversal on this leukocyte adherence increase. Sham animals present a high number of rolling leukocytes (Figure 20, part B) and these numbers are significantly decreased in the CASP group. Treatment with DFP, DFO, and DIBI did not improve leukocyte rolling levels, while DFX group showed no statistical difference to any of the other analysed groups.

These findings indicate that iron chelators DFO, DFP, and DIBI were able to alleviate the leukocyte-endothelial interactions at adhesion stage of V1 vessels. DFX treatment did not reduce CASP-induced leukocyte adhesion.

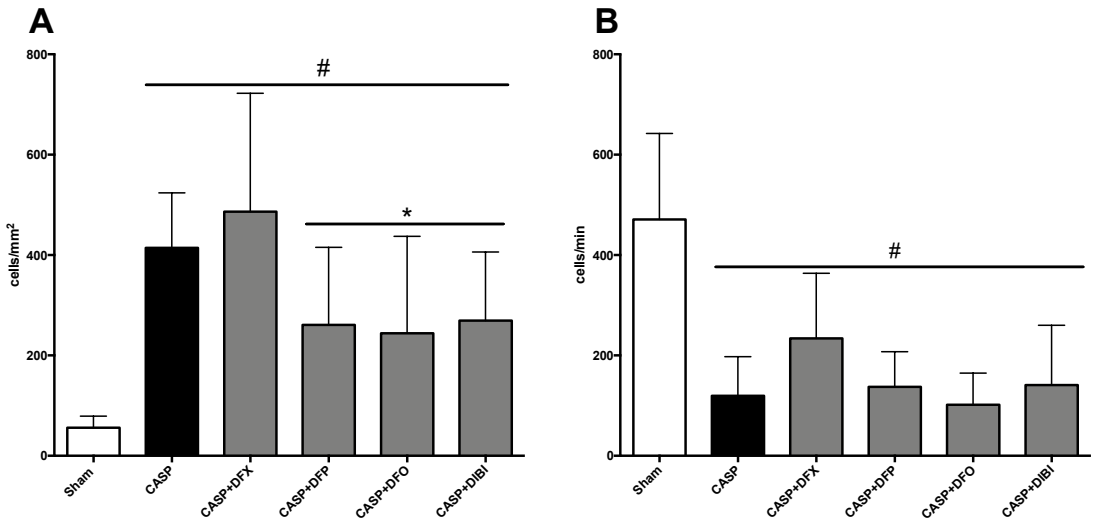

Figure 19. Effect of iron chelation on leukocyte adhesion and rolling in V1 vessels in poly-bacterial abdominal infection.

Bar graphs represent A) firmly adherent leukocytes (cells/mm^2) and B) rolling leukocytes (cells/min) in the intestinal submucosal collecting venules eight hours after CASP surgery. Treatment, one of the iron chelators, was administered at the end of the CASP surgery: DFO (15.76 mg/kg), DFP (10 mg/kg), DFX (18 mg/kg), DIBI (80 mg/kg). Data represented as mean ± SD (n= 5-7 per group); # $p < 0.05$ compared to sham group, *$p < 0.05$ compared to CASP group. CASP: Colon ascendens stent peritonitis; DFP: Deferiprone; DFO: Deferoxamine; DFX: Desferasirox.

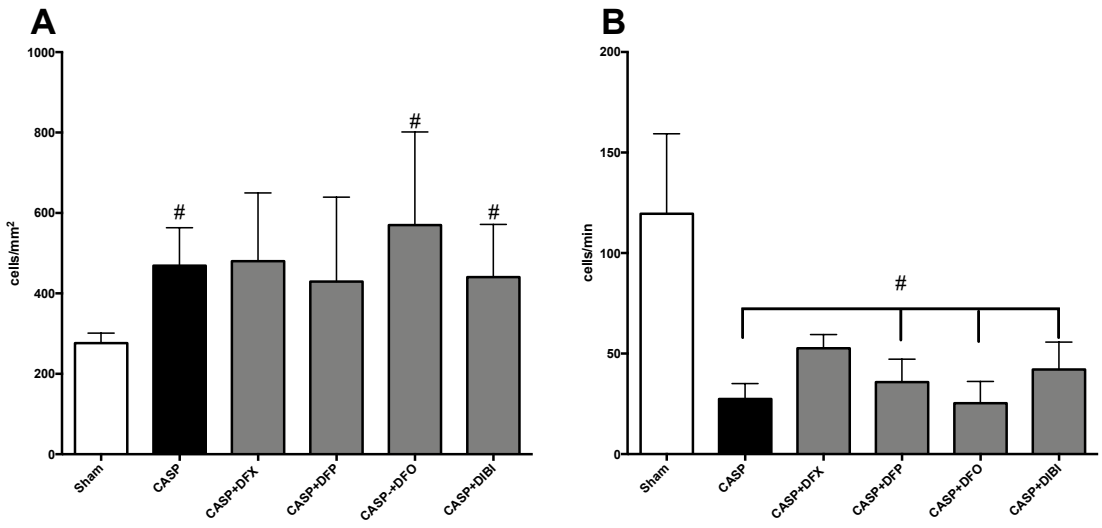

Figure 20. Effect of iron chelation on leukocyte adhesion and rolling in V3 vessels in poly-bacterial abdominal infection.

Bar graphs represent A) firmly adherent leukocytes and B) rolling leukocytes in the intestinal submucosal collecting venules (cells/mm^2) eight hours after CASP surgery. Treatment, one of the iron chelators, was administered at the end of the CASP surgery: DFO (15.76 mg/kg), DFP (10 mg/kg), DFX (18 mg/kg), DIBI (80 mg/kg). Data represented as mean ± SD (n= 3 per group); # $p < 0.05$ compared to sham group. CASP: Colon ascendens stent peritonitis; DFP: Deferiprone; DFO: Deferoxamine; DFX: Desferasirox.

3.2.1.2 Capillary blood flow

Given the importance and sensitivity of microcirculatory changes in infection, we were interested in observing the effect of iron chelation on capillary perfusion.

In both the muscle and mucosal layers, expectedly, the FCD was significantly reduced in CASP animals, when compared to the sham group (Figure 21, parts A and B). Iron chelation treatments did not change the FCD levels compared to CASP levels within the muscle layer (Figure 21, Part A). Within the mucosal layer, DFO and DIBI significantly reduced FCD from sham levels, similar to CASP (Figure 21, Part B). With DIBI and DFO treatments, the FCD remained reduced significantly from sham group. With DFX and DFP treatments, the FCD levels were similar to the sham group, indicating that DFX and DFP treatments inhibited the CASP-induced FCD reduction.

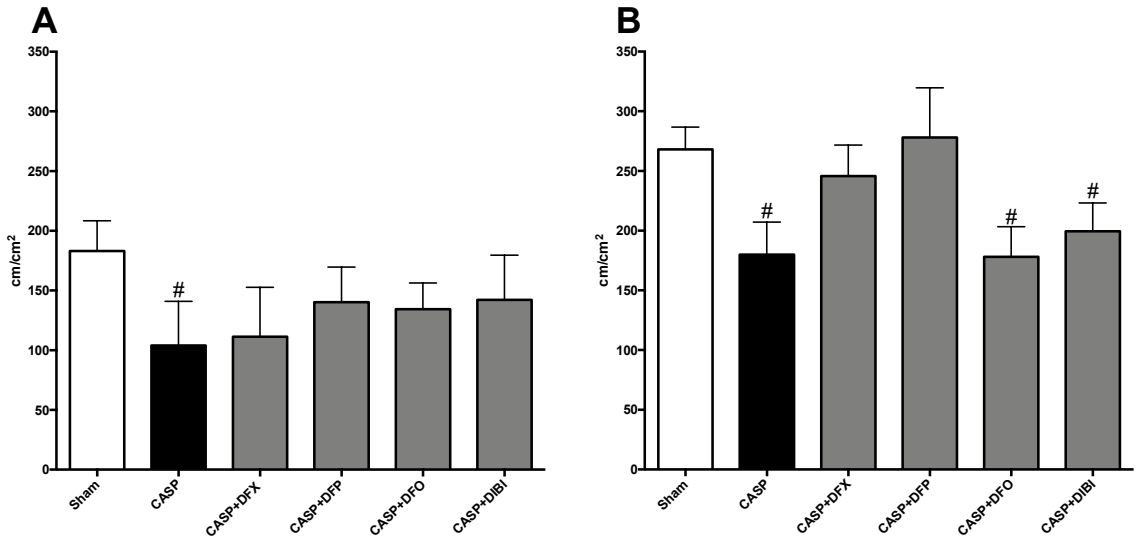

Figure 21. Effect of iron chelation on capillary blood flow in poly-bacterial abdominal infection.

Bar graphs functional capillary density (FCD) in the intestinal A) muscle and B) mucosal villi layers eight hours after CASP surgery. Functional capillary density was calculated as following: total length of all perfused vessels in the region of interest divided by the total area selected (cm/cm^2). Treatment, one of the iron chelators, was administered at the end of the CASP surgery: DFO (15.76 mg/kg), DFP (10 mg/kg), DFX (18 mg/kg), DIBI (80 mg/kg). Data represented as mean ± SD (n= 3-4 per group); # $p < 0.05$ compared to control group (sham). CASP: Colon ascendens stent peritonitis; DFP: Deferiprone; DFO: Deferoxamine; DFX: Desferasirox.

3.2.1.3 Plasma inflammatory mediators

Plasma samples were collected eight hours and 45 minutes after CASP surgery to study the effect of iron chelation on inflammatory mediators contributing to the poly-bacterial abdominal infection.

The immune response induced by CASP increased TNF-α levels significantly when compared to sham animals (Figure 22, part A). None of the iron chelation treatments were able to significantly reduce the CASP-induced TNF-α release, with DFX treatment causing an even higher increase in TNF-α levels than the CASP group itself. Levels of IFN-γ increased significantly in the CASP and, again, with DFX treatment, compared to sham levels (Figure 22, part B). Treatment with DFP, DFO, or DIBI did not change the secretion of IFN-γ from CASP levels.

Analysis of IL-1β levels mimicked the pattern seen for IFN-γ. IL-1β secretion was increased significantly in CASP group when compared to sham animals (Figure 22, part C). DFX, DFP, DFO, and DIBI treatments did not change the IL-1β secretion levels significantly from CASP levels. IL-6 level secretion was increased significantly in the CASP group from sham levels (Figure 22, part D). This CASP-induced IL-6 release was observed with DFX and DFO treatments. Meanwhile, none of the treatments changed IL-6 level significantly from CASP levels. IL-10 secretion was not different between sham and CASP groups (Figure 22, part E). All chelation treatments, except DFX, did not change IL-10 levels significantly from sham or CASP. Levels of sICAM-1 were significantly increased in all of the animals that underwent CASP surgery (Figure 22, part F), and none of the treatments with the iron chelators were able to reverse the induction caused by CASP. P-selectin levels in CASP group did not increase from sham to CASP levels (Figure 22, part G). Iron chelation treatment caused no significant effect.

In summary, CASP increased the level of the studied inflammatory mediators, as compared to sham level. Though there are visible trends seen with iron chelation treatment, none of these changes were statistically significant from CASP levels due to the large variability within the samples.

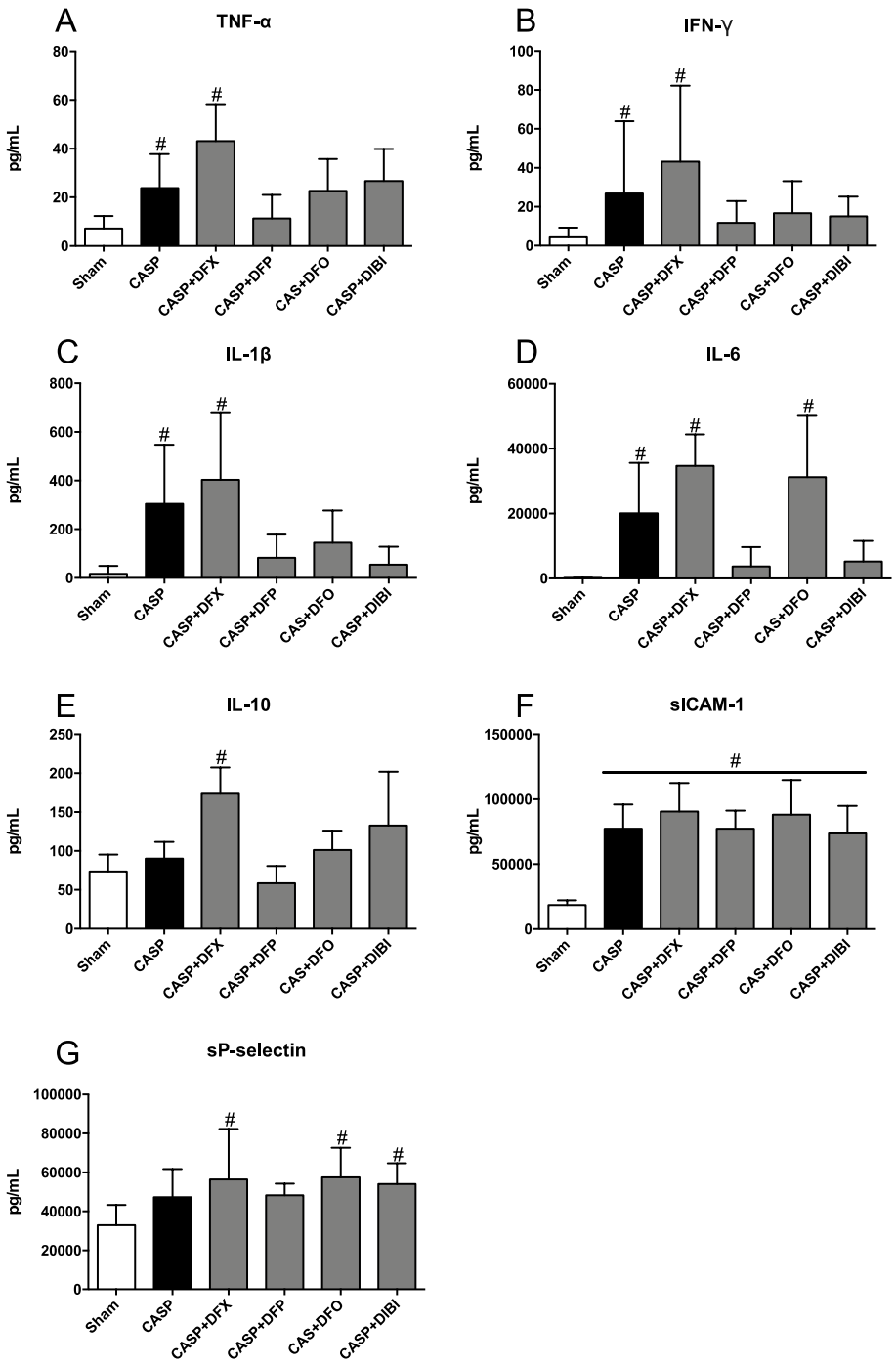

Figure 22. Effects of iron chelation on plasma inflammatory mediators in poly-bacterial abdominal infection.

Samples were taken eight hours and 45 minutes after CASP surgery. Treatment, one of the iron chelators, was administered at the end of the CASP surgery: DFO (15.76 mg/kg), DFP (10 mg/kg), DFX (18 mg/kg), DIBI (80 mg/kg). Bar graphs represent mean cytokine values ± SD (n = 3-7); # $p < 0.05$ compared to control (sham) group. CASP: Colon ascendens stent peritonitis; DFP: Deferiprone; DFO: Deferoxamine; DFX: Desferasirox.

3.2.1.4 Histology

In intestinal samples collected from sham animals, there were some histological damage present as determined by Chiu score (Figure 23). This damage was further increased (significantly) in CASP animals. DFX, DFP, and DFO treatments were able to significantly reduce this CASP-induced damage. There was no change observed with DIBI treatment, from CASP levels.

3.2.1.5 Bacteria Enumeration

To measure the bacterial burden and the impact of iron chelation treatment on bacterial growth, PLF and blood samples were collected and plated on tryptic soy agar (TSA) plates.

In both PLF and blood samples, similar results were obtained (Figure 24). Due to the CASP surgery and the ongoing bacterial leakage, the bacterial counts were increased significantly in the CASP group, as compared to sham animals. This increase in bacterial burden was also observed in the iron chelation treated CASP groups (CASP+ DFX/DFP/DFO/DIBI). None of the iron chelators significantly reduced the bacterial counts, though DFO and DIBI had the lowest mean bacterial burden.

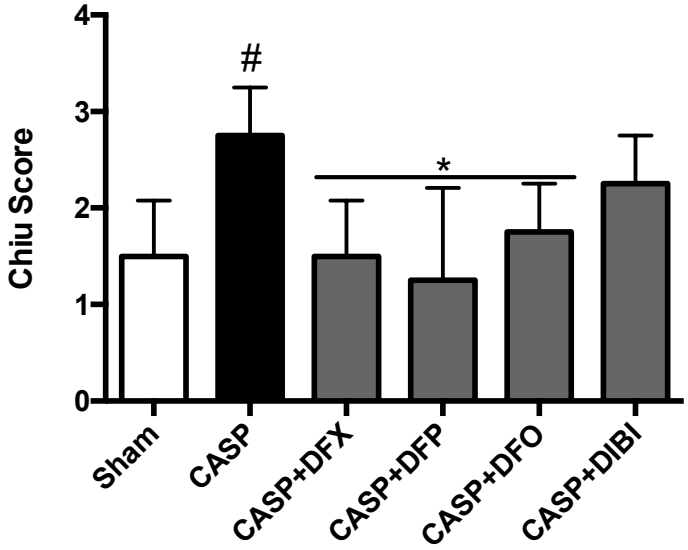

Figure 23. Effects of iron chelation on morphological changes within the intestinal mucosa in poly-bacterial abdominal infection.

Samples were taken eight hours and 45 minutes after CASP surgery. Treatment, one of the iron chelators, was administered at the end of the CASP surgery: DFO (15.76 mg/kg), DFP (10 mg/kg), DFX (18 mg/kg), DIBI (80 mg/kg). Samples were collected post-mortem, fixed, and embedded in paraffin. Tissue sections were stained with H&E. Bar graphs represent mean Chiu score ± SD (n=4 animals). # $p < 0.05$ compared to sham group, *$p < 0.05$ compared to CASP group. CASP: Colon ascendens stent peritonitis; DFP: Deferiprone; DFO: Deferoxamine; DFX: Desferasirox.

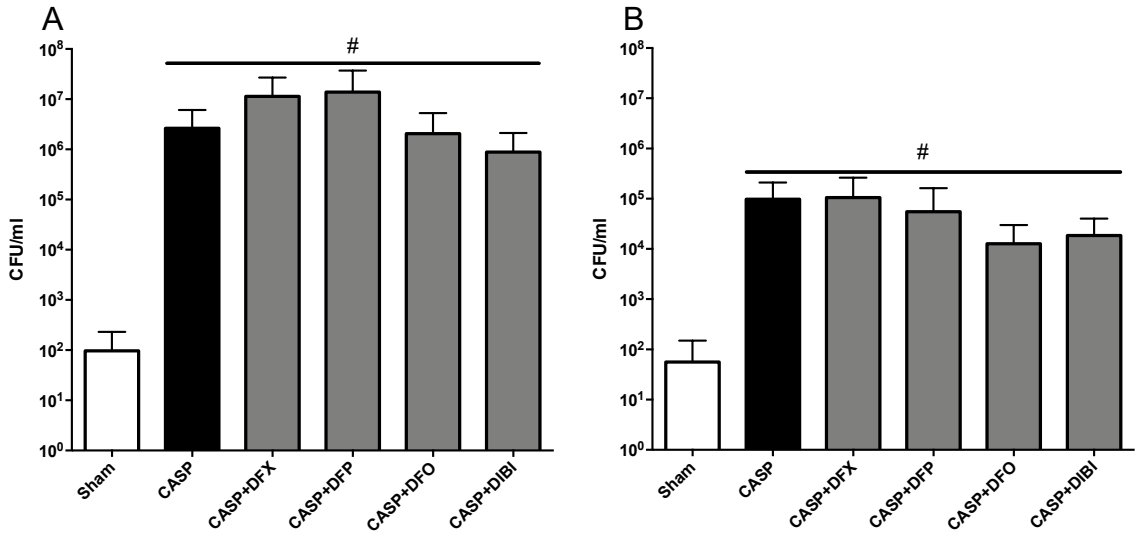

Figure 24. Effects of iron chelation on bacterial enumeration of peritoneal lavage fluid and blood in poly-bacterial abdominal infection.

Bacterial burden was measured by plating A) peritoneal lavage fluid collected at 7 hours and 45 minutes and B) blood collected at eight hours and 45 minutes after CASP surgery on tryptic soy agar plates. Treatment, one of the iron chelators, was administered at the end of the CASP surgery: DFO (15.76 mg/kg), DFP (10 mg/kg), DFX (18 mg/kg), DIBI (80 mg/kg). The bacterial colonies were counted 16-24 hours later (CFU/ml). Data are represented as mean ± SD (n=4-8 per group); # $p < 0.05$ compared to sham group. CASP: Colon ascendens stent peritonitis; DFP: Deferiprone; DFO: Deferoxamine; DFX: Desferasirox.

3.2.1.6 Microbiome sequencing

Following bacterial enumeration, we were interested in the composition of these bacteria within the PLF samples. The results provide a gateway into the relative bacterial distribution in their taxonomic sequencing. PLF samples from sham animals had low bacterial quantity and thus were not analyzed.

In the class taxonomic bacterial distribution of CASP samples (Figure 25, part A) Bacteroidia was the dominant class of bacteria (62.2 %), followed by Gammaproteobacteria (31.1 %), Clostridia (4.3 %), and Bacilli (1.8 %), together forming the majority of the composition. These four classes were the most common classes within the treatment groups as well, although their relative distributions were different. A deeper analysis into the family level of CASP bacterial distribution revealed *Bacteroidaceae* (55%) and *Enterobacteriaceae* (31%) to be the most common population of bacteria (Figure 25, part B).

DFX samples were composed of Bacteroidia (54.9 %), Gammaproteobacteria (29 %), Clostridia (9.1 %), Bacilli (5.5 %). The family distribution was similar to CASP with *Bacteroidaceae* (47%) and *Enterobacteriaceae* (29%) forming majority of the diversity. Streptococcaceae distribution was larger in DFX treated animals. DFP samples contained Bacteroidia (60.3 %), Gammaproteobacteria (20.7 %), Clostridia (13.7 %), and Bacilli (3.4 %). In addition to the common *Bacteroidaceae* (52%) and *Enterobacteriacea*e (21%), DFP treatment appears to have increase the distribution of bacteria from *Clostridiales* (10%) order. The family of this bacterial order was not specified by the analysis library.

PLF from DFO treated animals comprised of Bacteroidia (70.4 %), Clostridia (14.3 %), Gammaproteobacteria (8.5 %), and Bacilli (4.3 %) classes. DFO treated animals, interestingly, showed the lowest distribution of both *Gammaproteobacterial* class and Enterobacteriaceae family (8.5%). DFO treatment also resulted in the highest distribution of Bacteroidia (70.4 %) and *Bacteroidaceae* (62%) compared to the other samples. DFO treatment also increased the relative population of Clostridia class (14.3 %) significantly as

compared to CASP group. *Enterobacteriacea*e family (8.5 %) of bacteria were found in the smallest distribution within the DFO treated animals, as compared to all other groups.

DIBI treated samples were composed of Bacteroidia (66.3 %), Gammaproteobacteria (23.6 %), Clostridia (7.0 %), and Bacilli (1.1 %) classes. Deeper family analysis revealed *Bacteroidaceae* (55%), and *Enterobacteriacea*e (24 %) to be present. When compared to the other iron chelators, DIBI did not change the bacilli composition levels compared to CASP. It is important to note that the iron chelators, specially DFO, appeared to increase clostridia population relative to the other classes when compared to untreated CASP.

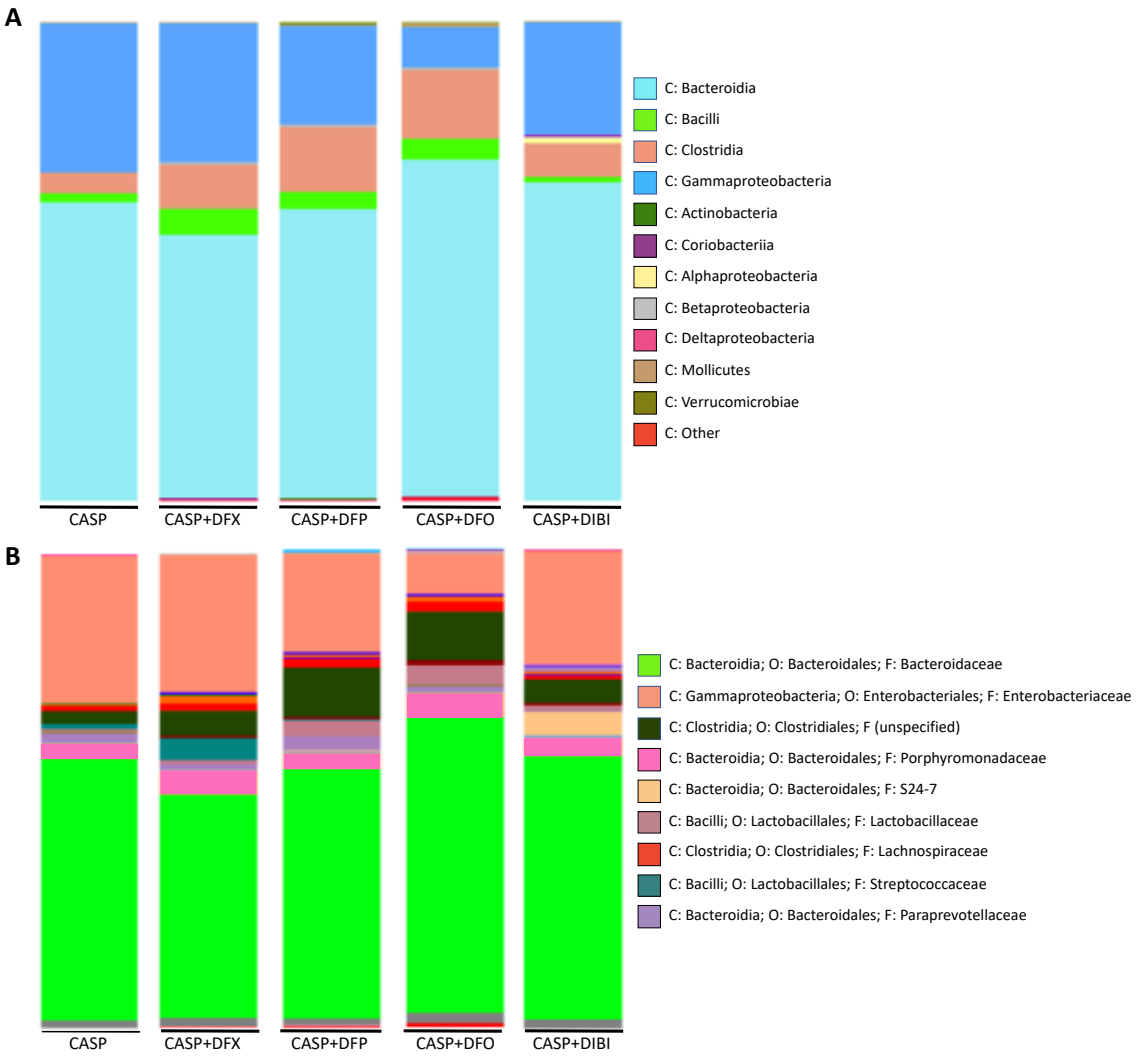

Figure 25. Taxonomic composition of peritoneal lavage fluid microbiome at class and family levels in poly-bacterial abdominal infection.

Grouped class (A), and family (B) bar graph plots of taxonomic composition of bacteria in peritoneal lavage fluid collected seven hours and 45 minutes after CASP surgery. Treatment, one of the iron chelators, was administered at the end of the CASP surgery: DFO (15.76 mg/kg), DFP (10 mg/kg), DFX (18 mg/kg), DIBI (80 mg/kg). Sham animals did not have enough microbial DNA for analysis. (n=4-5 per group). C: Class; CASP: Colon ascendens stent peritonitis; DFP: Deferiprone; DFO: Deferoxamine; DFX: Desferasirox; F: family; O: order.

3.2.2 Colon ascendens stent peritonitis with intervention (CASP-I)

In the CASP-I model, the effects of DIBI and imipenem, a broad-spectrum antibiotic from carbapenem class, on peritonitis were assessed by measuring survival time and health status of the mice using the murine sepsis score (MSS). Bacterial burden was determined by measuring both aerobic and anaerobic bacterial growth in the PLF samples. Histological assessment was performed to study the morphological tissue damage of the intestine.

3.2.2.1 Survival parameter

Mice from the sham-I surgery group all survived the total analysis time (n=5; T=168hr), indicating that surgery by itself was not responsible for death (Figure 26). Collectively, there were significant differences in survival time between the experimental conditions.

Untreated CASP-I mice (n=6) had rapid progression of sepsis and their health declined quickly, leading to their death within the first day of analysis. The group's average survival time was 14 hours post-surgery, the lowest survival time compared to all other groups studied. When DIBI treatment was added (CASP-I+DIBI; n=6), four animals (67% of the group) had similar survival to untreated CASP-I animals and died within the first day. The remaining two animals had 52.5 hours and 67 hours survival timings, giving the group an average survival of 29.7 hours.

CASP-I animals that received imipenem (CASP-I+IMI; n=6), showed an improved survival where two mice died within the first day (33.3 %) and one of the mice (16.7 %) survived until day 7. The average survival time for this group was 57.7 hours. To test the synergy of imipenem (IMI) and DIBI, both treatments were administered (CASP-I+IMI+DIBI; n=6). Although two mice died within the first day (33.3 %), the average survival of these mice was drastically increased to 82.57 hours. One mouse (16.7 %) survived to day 7. The final treatment group consisted of imipenem and double doses of DIBI (CASP-I+IMI+$DIBI_2$; n=6). Only one mouse died within the first day (16.7 %) and two mice survived to day seven. The average survival time was 94.375 hours. Interestingly, the combined medication groups were superior to DIBI treatment alone (CASP-I+DIBI) in improving survival outcome.

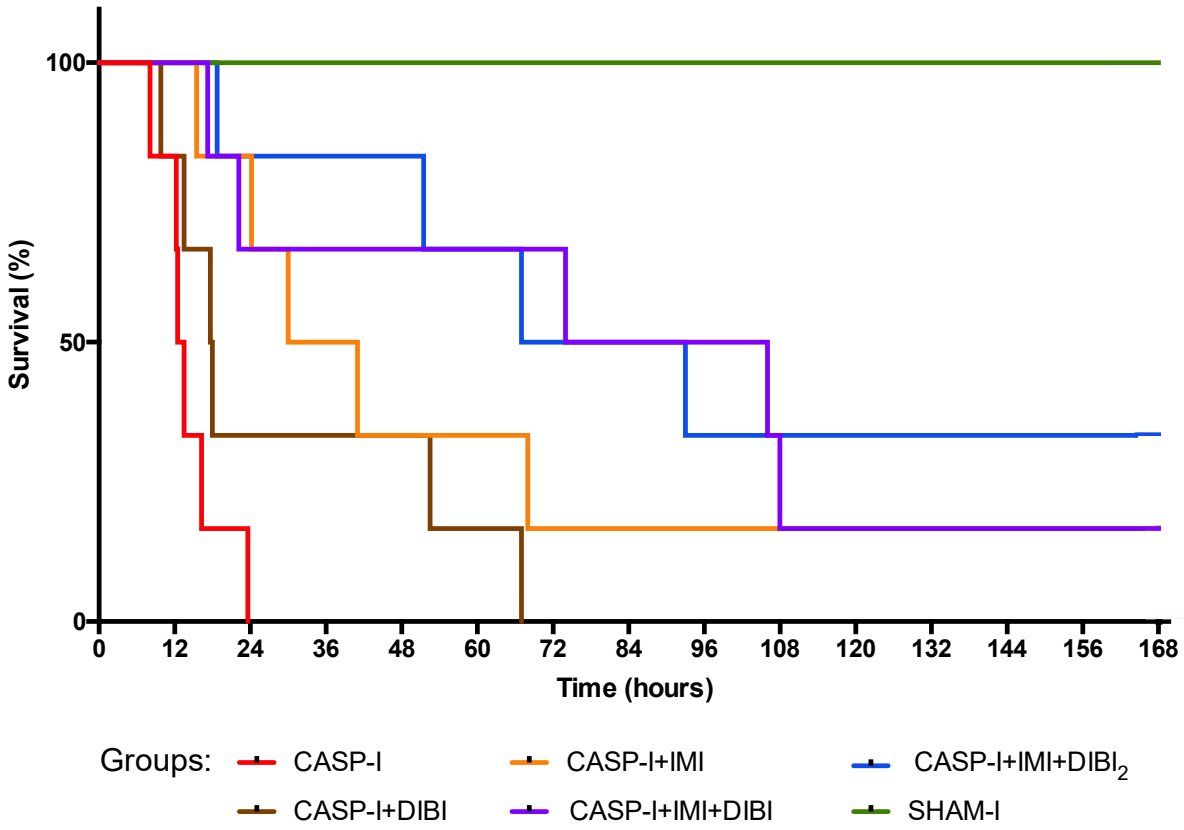

Figure 26. Survival proportions of CASP-I model.

The data represents the percent survival of surviving mice that received an intervention surgery at T=5 hours, to remove the stent and close the puncture. Sham-I (n= 5) and CASP-I (n=6) animals received saline at T=0 hour and T=5 hours. CASP+DIBI (n= 6) received DIBI (80 mg/kg) at T=0 hour followed by saline at T=5 hours. CASP-I+IMI (n= 6) received IMI (25 mg/kg) at T=0 hour followed by saline at T=5 hours. CASP-I+IMI+DIBI (n= 6) received IMI and DIBI at T=0 hour and saline at T=5 hours. CASP-I+IMI+$DIBI_2$ (n=6) received IMI and DIBI at T=0 hour and a second dose of DIBI at T=5 hour. CASP-I: Colon ascendens stent peritonitis with intervention at T=5 hours; DIBI: novel iron chelator; IMI: imipenem antibiotic.

3.2.2.2 Mean Murine Sepsis Score (MSS) Curves

To assess the health status, the mice were closely observed and their MSS was recorded every two hours until 12 hours post-surgery. Upon showing signs of distress or rapid decline in health, the mice were monitored more frequently even if the first 12 hours had passed. The MSS score is negatively correlated to the health status: if mice demonstrated a decline in their health and showed more severe sepsis symptoms, their MSS score was increased.

The mean MSS score from each group is presented in Figure 27. The untreated CASP-I animals had poor outcome, more severe sepsis symptoms, which resulted in a rapid increase of their MSS score. This led to the death of these animals. As mentioned previously, none of CASP-I mice were able to survive past day one. CASP-I+DIBI group had similar tendency of rapid increase in MSS score. Both of these groups had the highest mean MSS scores.

With imipenem treatment (CASP-I+IMI), the MSS score pattern was similar to CASP-I and CASP-I+DIBI early on. However, close to 22 hours, the score started to plateau. Despite peaking again later on (close to 37.5 hours), the MSS score did not rise as high as the untreated CASP-I and CASP-I+DIBI animals. Combination of DIBI and imipenem treatments (both CASP-I+IMI+DIBI and CASP-I+IMI+$DIBI_2$), initially increased the MSS score. However, close to 22 hours, the scores started to slowly decline. After 3 days, the MSS score became relatively stable. MSS score of CASP-I+IMI+DIBI animals remained close to 1 while the CASP-I+IMI+$DIBI_2$ group had an MSS score of zero until the mice were euthanized (168 hours).

It was interesting to observe that all treatment groups had an increase in their mean MSS scores initially. However, the rate of progression of clinical symptoms (as assed by MSS score) in the groups with worst survival outcome (CASP-I and CASP-I+DIBI) rapidly increased at 17 hours. The overall magnitude and progression rate of these scores were in agreement with the survival data obtained, highlighting the potential predictive role of MSS score for sepsis mortality.

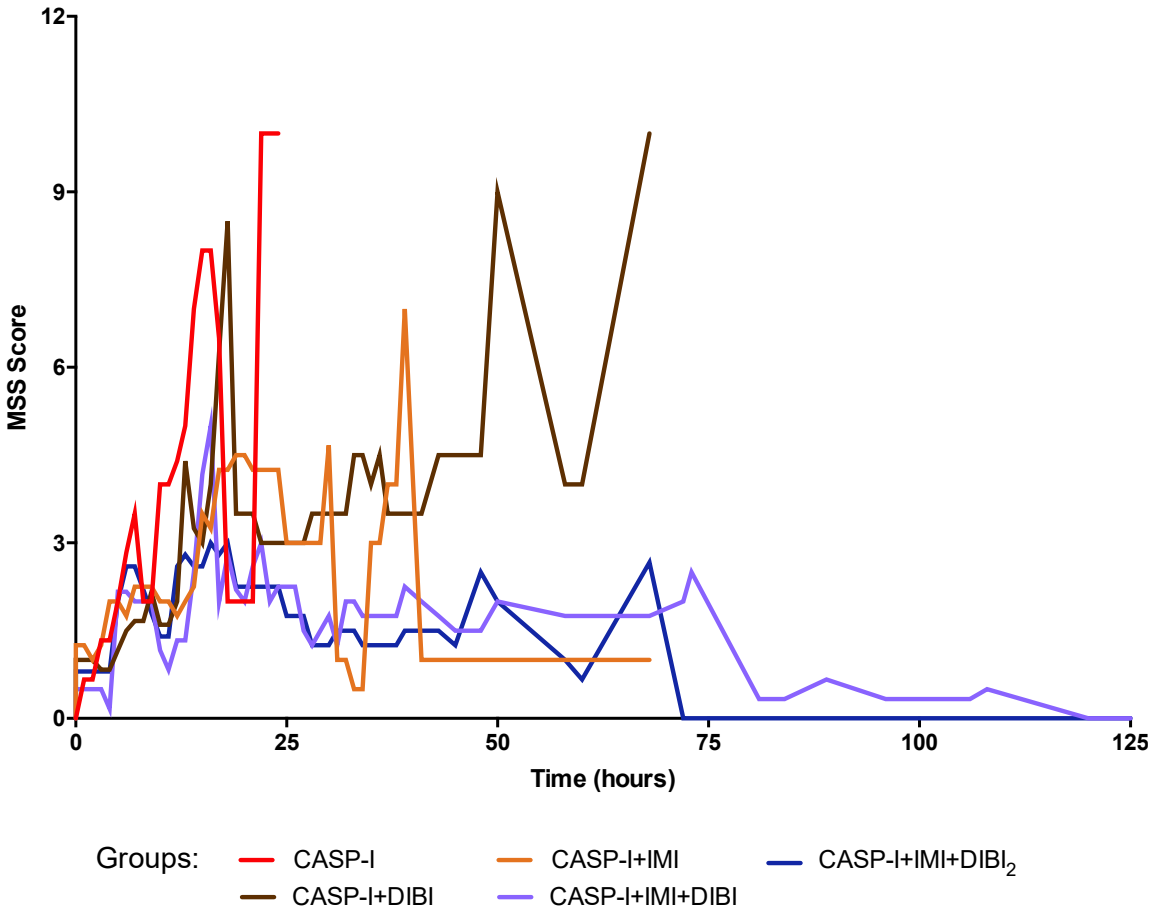

Figure 27. Mean MSS Score curves for CASP-I model.

The data represents mean murine sepsis scores (MSS) over time for the mice that received an intervention surgery at 5 hours, to remove the stent and close the puncture. CASP-I (n= 6) animals received saline at T=0 hour and T=5 hours. CASP+DIBI (n= 6) received DIBI (80 mg/kg) at T=0 hour followed by saline at T=5 hours. CASP-I+IMI (n= 6) received IMI (25 mg/kg) at T=0 hour followed by saline at T=5 hours. CASP-I+IMI+DIBI (n= 6) received IMI and DIBI at T=0 hour and saline at T=5 hours. CASP-I+IMI+$DIBI_2$ (n= 6) received IMI and DIBI at T=0 hour and a second dose of DIBI at T=5 hours. CASP-I: Colon ascendens stent peritonitis with intervention at T=5 hours; DIBI: novel iron chelator; IMI: imipenem antibiotic.

3.2.2.3 Bacterial enumeration

PLF samples were obtained at the end of the intervention surgery (T=5 hours) and were plated on various agars for bacterial enumeration. PLF samples were also collected post-mortem, though due to the high variability of the collection time, data is not shown.

Total aerobic bacterial burden was increased in the untreated CASP-I group from sham-I levels, as expected (Figure 28, part A). Single dose DIBI or IMI treatments did not change the bacterial burden from CASP-I levels. However, the bacterial burden appeared to be lower in both combination groups (CASP-I+IMI+DIBI and CASP-I+IMI+$DIBI_2$). To quantify the Gram-negative bacterial population, the PLF samples were plated on MacConkey agar. The number of Gram-negative bacteria increased significantly in CASP-I group from sham-I levels (Figure 28, part B). The bacterial burden did not change with imipenem, DIBI, or the combination treatment with single dose of DIBI (CASP-I+ IMI/DIBI/IMI+DIBI). Interestingly, repeating the DIBI dose in combination with imipenem significantly reduced the bacterial burden from CASP-I levels (CASP-I+IMI+$DIBI_2$; 99 % reduction).

Similar findings were observed by analyzing total anaerobic bacteria levels (Figure 28, part C). The total anaerobic bacteria levels were significantly increased in the CASP-I group. Even though there was no reduction in bacterial burden by DIBI, imipenem, and single dose DIBI (CASP-I+IMI+DIBI) treatments, repeating the DIBI dose in combination with imipenem (CASP-I+IMI+$DIBI_2$) effectively reduced the anaerobic bacterial burden caused by CASP-I (99 % reduction). The results highlight the additive effects of imipenem and double dose DIBI in reducing bacterial burden.

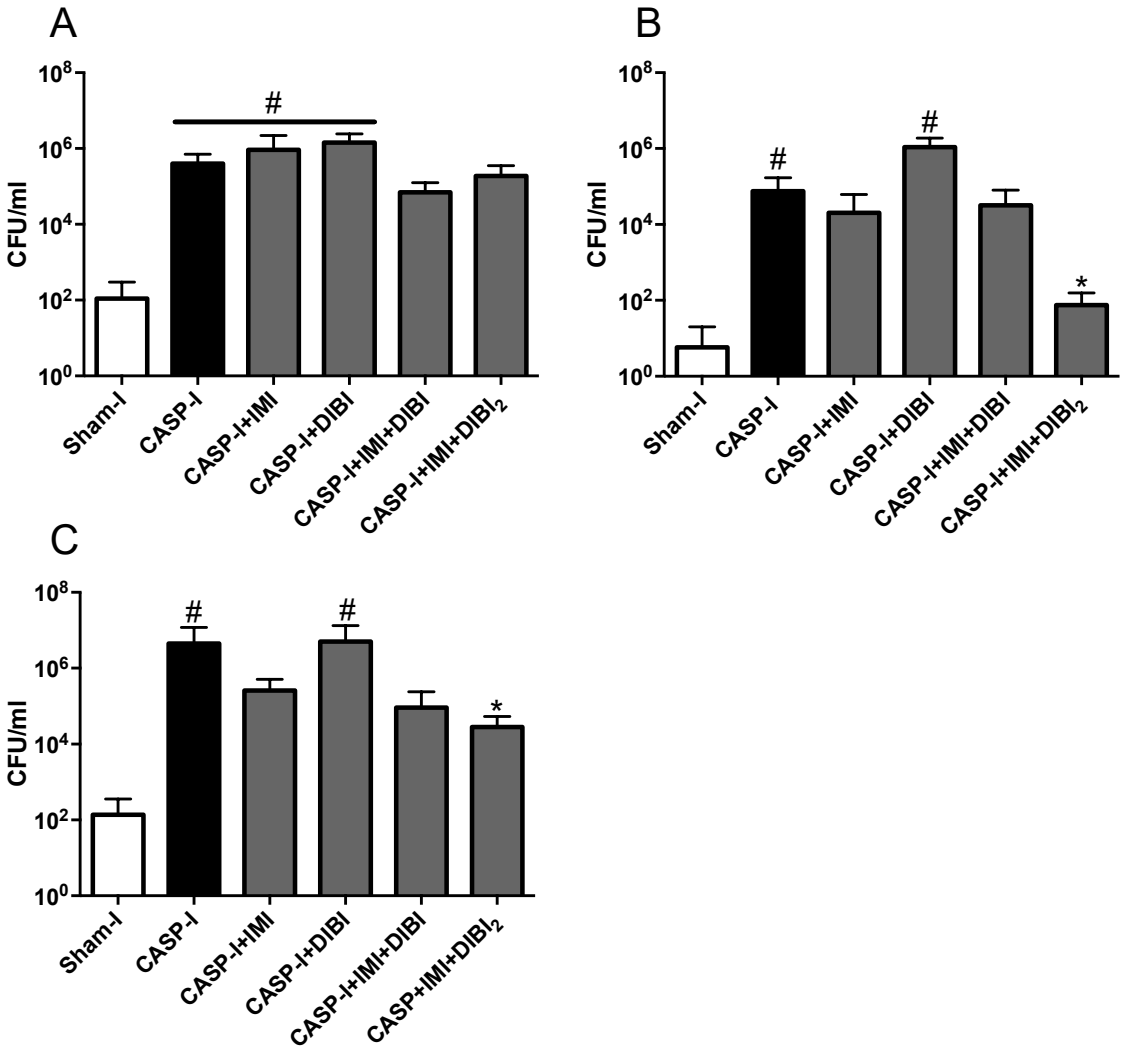

Figure 28. Bacterial burden in the PLF of CASP-I animals.

Total aerobic (part A), Gram-negative aerobic (B), and total anaerobic (C) bacterial burden was measured by plating peritoneal lavage fluid obtained at the time of intervention surgery T=5 hours, to remove the stent and close the puncture. Sham-I and CASP-I animals received saline at T=0 hour and T=5 hours. CASP+DIBI received DIBI (80 mg/kg) at T=0 hour followed by saline at T=5 hours. CASP-I+IMI received IMI (25 mg/kg) at T=0 hour followed by saline at T=5 hours. CASP-I+IMI+DIBI received IMI and DIBI at T=0 hour and saline at T=5 hours. CASP-I+IMI+$DIBI_2$ received IMI and DIBI at T=0 hour and a second dose of DIBI at T=5 hours. The samples were plated on TSA (parts A and C) or MacConkey agar (part B) plates and the bacterial colonies were counted 16 to 24 hours later (CFU/ml). Data are represented as mean ± SD (n=3-6 per group); # $p < 0.05$ vs Sham-I group; * $p<0.05$ vs CASP-I. CASP-I: Colon ascendens stent peritonitis with intervention at T=5 hours; DIBI: novel iron chelator; IMI: imipenem antibiotic.

3.2.2.4 Histology

Small intestine samples were collected from the mice post-mortem, which varied between the different animals and treatment groups. Upon morphological assessment, sham-I animals had no visible damages and thus had a Chiu score of zero (Figure 29). The untreated CASP-I animals had a higher average score than sham-I animals, but this difference was not significant. Within the treatment groups, though the average score means were different, there was no statistical difference from CASP-I levels. While interpreting these results, it is important to consider the collection timepoints of the samples. All CASP-I mice survival were limited to day 1 while some mice in double dose DIBI combination group (CASP-I+IMI+$DIBI_2$) survived until day 7. Determining whether the treatments were effective on modulating intestinal damage, depends on the time passed from the infection induction by CASP-I.

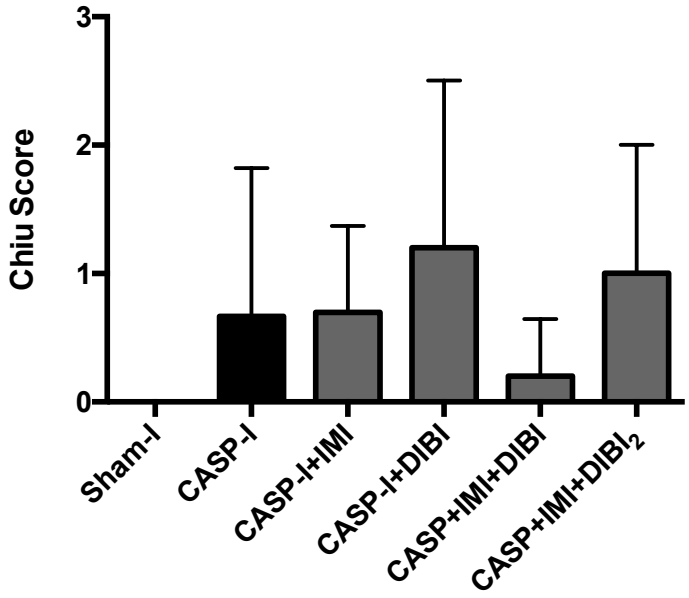

Figure 29. Morphological changes within the intestinal mucosa in CASP-I model.

The data represents histological assessment of mice that received an intervention surgery at T=5 hours, to remove the stent and close the puncture. Sham-I and CASP-I animals received saline at T=0 hour and T=5 hours. CASP+DIBI received DIBI (80 mg/kg) at T=0 hour followed by saline at T=5 hours. CASP-I+IMI received IMI (25 mg/kg) at T=0 hour followed by saline at T=5 hours. CASP-I+IMI+DIBI received IMI and DIBI at T=0 hour and saline at T=5 hours. CASP-I+IMI+$DIBI_2$ received IMI and DIBI at T=0 hour and a second dose of DIBI at T=5 hours. Samples were collected post-mortem, fixed, and embedded in paraffin. Tissue sections were stained with H&E. Bar graphs represent mean Chiu score ± SD (n=3-6 animals). CASP-I: Colon ascendens stent peritonitis with intervention at T=5 hours; DIBI: novel iron chelator; IMI: imipenem antibiotic.

3.3 Inflammation and Infection

CF is characterized by chronic inflammation and recurrent infections of the lungs. Within the airways of CF patients, the CFTR dysfunction impairs mucocilliary clearance resulting in ineffective pathogen clearance, which creates the ideal niche for bacteria to colonize. Additionally, CFTR defect has been shown to interfere with the leukocytes' activity such as neutrophil degranulation and macrophage phagocytosis, highlighting CFTR's impact on immune modulation. To test the effect of iron chelation in CF, a nasal epithelial cell line (CF15) homozygous for the Δ*F*508 mutation in the CFTR gene, was selected as an *in vitro* model of airway inflammation. Additionally, this model provided the opportunity to study the polarized response as the cells were grown on transwells and maintained epithelium in air liquid interface. Once the cells were confluent and formed a tight epithelium barrier, they were then treated with various doses of DIBI under basal or LPS-challenged conditions. Two additional doses of DIBI (50 and 100 μM), intermediate to the previously studied doses in neutrophils (25 and 200 μM), were included to conduct dose-response studies.

3.3.1 IL-6 and IL-8 release of CF15 cells in response to doses of DIBI

To understand the impact of iron chelation on CF15 cells at baseline conditions, the cells were incubated with DIBI at 25, 50, 100, 200 μM concentrations for 24 hours.

Control CF15 cells secreted an average of 196 pg/mL and 50 pg/mL IL-6 within apical and basolateral compartments, respectively (data not shown). These absolute values were used to measure relative changes induced by treatments from control levels. Cells incubated with lower DIBI doses (25 and 50 μM) showed a significant increase in apical IL-6 secretion from control levels (Figure 30, part A). On the contrary, DIBI doses of 100μM and 200μM did not stimulate IL-6 secretion in the apical compartment, maintaining the values close to the control levels. Similar to observation in the apical compartment, the basolateral IL-6 secretion was significantly increased when cells were incubated with DIBI 25 μM (Figure 30, part B). Meanwhile, DIBI 50, 100, and 200 μM did not induce basolateral IL-6 release, maintaining the control levels.

In regard to IL-8 secretion, a chemokine that attracts neutrophils to the inflamed site, control cells secreted an average of 64 pg/mL and 32 pg/mL IL-8 in the apical and basolateral compartments, respectively (data not shown). Interestingly, none of the treatments (DIBI 25, 50, 100, and 200 μM) induced significant changes from control levels in apical and basolateral compartments (Figure 31).

Having observed an increase in IL-6 levels with the lowest DIBI dose studied (25 μM), we were interested in whether this effect was observed during an inflammatory challenge. Thus next, the cells were stimulated with LPS and treated with DIBI.

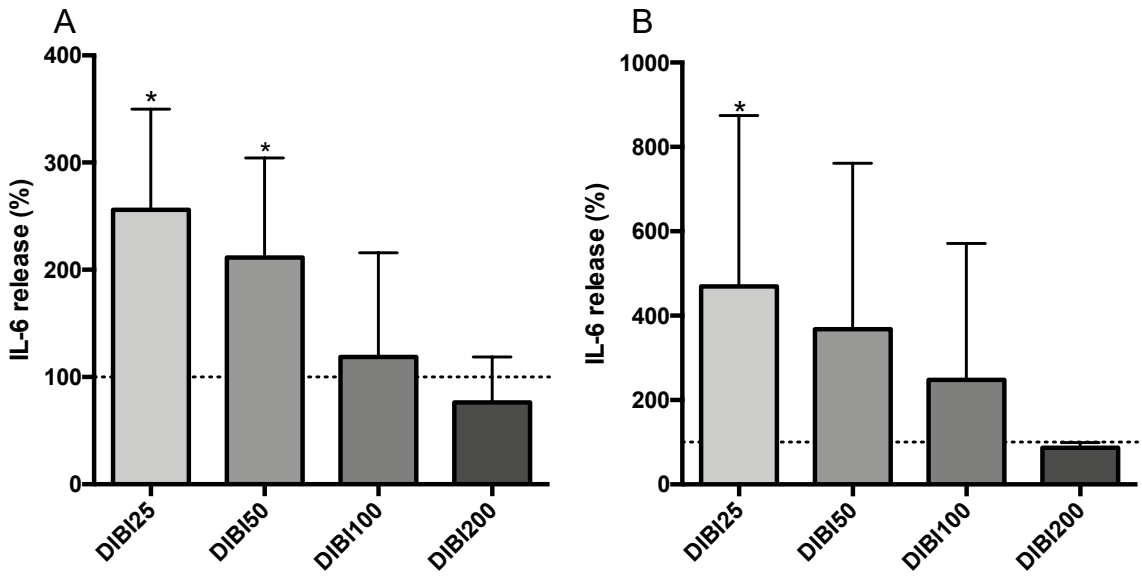

Figure 30. CF15 cells' IL-6 release in response to DIBI.

Apical (A) and basolateral (B) IL-6 secretions of polarized CF15 cells. CF15 cells were grown on transwells to establish an air-liquid interface. The cells were treated with DIBI (25, 50, 100, 200 μM) or medium alone for 24 hours. At the end of this incubation period, the supernatant was harvested for IL-6 analysis via ELISA, and cells were harvested for total protein concentrations measurement via Bradford assay. The IL-6 secretion amount was normalized to the protein concentration and the data represents the percentage change from control level (medium only). The dashed line denotes the IL-6 level of secretion in the control cells, corresponding to average values of 196 pg/mL and 50 pg/mL in apical and basolateral compartments, respectively. Data is presented as mean ± SD, (n=3-4 per group). *$P<0.05$ vs control. DIBI25: 25 μM; DIBI50: 50 μM; DIBI100: 100 μM; DIBI200: 200 μM.

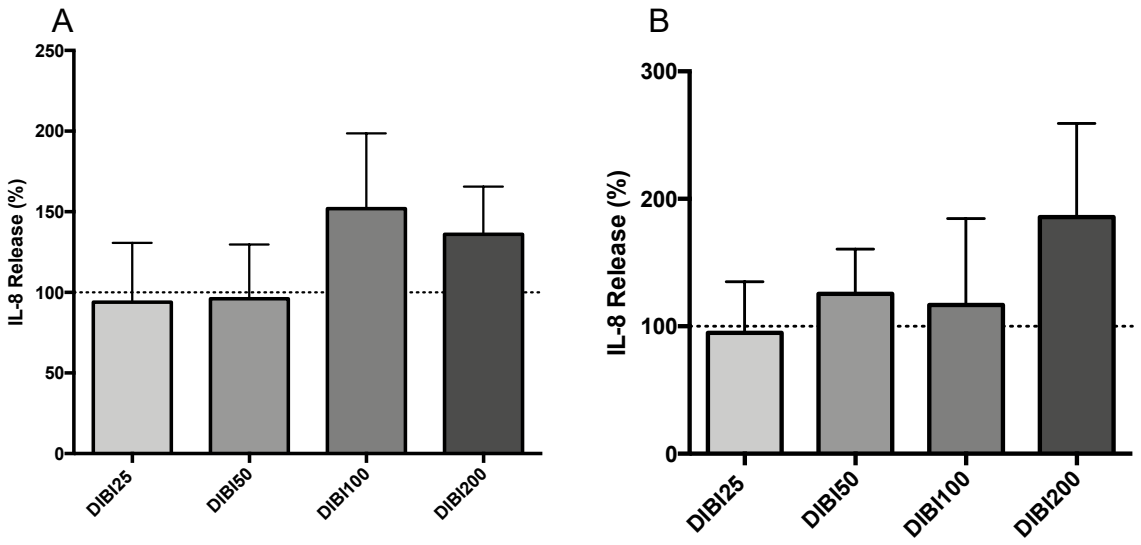

Figure 31. CF15 cells' IL-8 release in response to DIBI.

Apical (A) and basolateral (B) IL-8 secretions of polarized CF15 cells. CF15 cells were grown on transwells to establish an air-liquid interface. The cells were treated with DIBI (25, 50, 100, 200 μM) or medium alone for 24 hours. At the end of this incubation period, the supernatant was harvested for IL-8 analysis via ELISA, and cells were harvested for total protein concentrations measurement via Bradford assay. The IL-8 secretion amount was normalized to the protein concentration and the data represents the percentage change from control level (medium only). The dashed line denotes the IL-8 level of secretion in the control cells, corresponding to average values of 64 pg/mL and 32 pg/mL in apical and basolateral compartments, respectively. Data is presented as mean ± SD, (n=3-4 per group). *P<0.05 vs control. DIBI25: 25 μM; DIBI50: 50 μM; DIBI100: 100 μM; DIBI200: 200 μM.

3.3.2 IL-6 and IL-8 release of CF15 cells in response to LPS challenge

CF15 cells were stimulated with various doses of LPS (100, 200, 300 ng/mL) for 24 hours or 48 hours in order to generate an inflammatory environment. Compared to control levels, LPS dose of 200 ng/mL for 24 hours increased the IL-6 cytokine secretion the highest in both apical (Figure 32, part A), and basolateral (part B) compartments. Based on this result, all subsequent experiments in the CF15 cells were stimulated with 200 ng/mL of LPS for 24 hours.

LPS-stimulation increased IL-6 secretion in CF15 to 526.5 pg/mL and 99.5 pg/mL in to the apical and basolateral compartments, respectively (data not shown). This corresponded to an increase of 169 % and 99 % of IL-6 secretion in apical and basolateral compartments with LPS stimulation, respectively. Additionally, to better understand CF15 cells' inflammatory response, Calu-3 cells (human bronchial epithelial serous cells expressing the wildtype CFTR) were stimulated with the same dose of LPS (200 ng/mL) under the same conditions and IL-6 levels were measured. Apical IL-6 levels increased from 1464 pg/mL in control cells (media only) to 1725 pg/ml in LPS stimulated cells; within basolateral compartment IL-6 secretion increased from 380 pg/mL in control cells to 625.5 pg/mL in LPS-stimulated cells (data not shown). The Calu-3 cells response to LPS stimulation increased IL-6 release by 17% and 64% in apical and basolateral compartments, respectively. The LPS-induced IL-6 secretion was much more potent in CF15 cells as compared to Calu-3 cells.

Apical IL-6 secretion significantly increased in LPS-stimulated CF15 cells with DIBI treatments of 25 and 50 μM (LD25 and LD50), from LPS level (Figure 33, part A). LPS and DIBI 100 μM treatment (LD100) did not change the levels of IL-6 secretion from LPS. On the other hand, cells incubated in LPS and DIBI 200 μM (LD200), had significantly reduced IL-6 secretion compared from LPS level. On the basolateral compartment, LPS-induced cells treated with DIBI 25, 50, and 100 μM showed no changes in IL-6 secretion, though DIBI 200 μM reduced IL-6 basolateral secretion significantly (Figure 3, part B).

Cells incubated with 200 ng/mL of LPS showed an increased release of IL-8 to 79.5 pg/mL and 54 pg/mL on apical and basolateral compartments, respectively. LPS+ DIBI 25, 50, or 100 μM had no significant effect on IL-8 secretion in comparison to LPS only group in the apical compartment (Figure 34, part A). However, the highest dose of DIBI (200 μM) significantly reduced IL-8 secretion in the apical side; a similar response was observed in the basolateral compartment, where both DIBI 100 and 200 μM lowered IL-8 secretion significantly (Figure 34, part B).

Overall, the highest dose of DIBI studied (200 μM) did not induce IL-6 and IL-8 release in CF15 cells at basal condition. However, it lowered LPS-induced IL-6 and IL-8 secretion. Lowest studied dose of DIBI (25 μM) induced IL-6 secretion at basal condition. Additionally, it further increased LPS-induced IL-6 and IL-8 levels. To better understand DIBI's molecular mechanism and how it modulates the inflammatory pathways, a few signalling pathways were targeted for analysis via immunofluorescence.

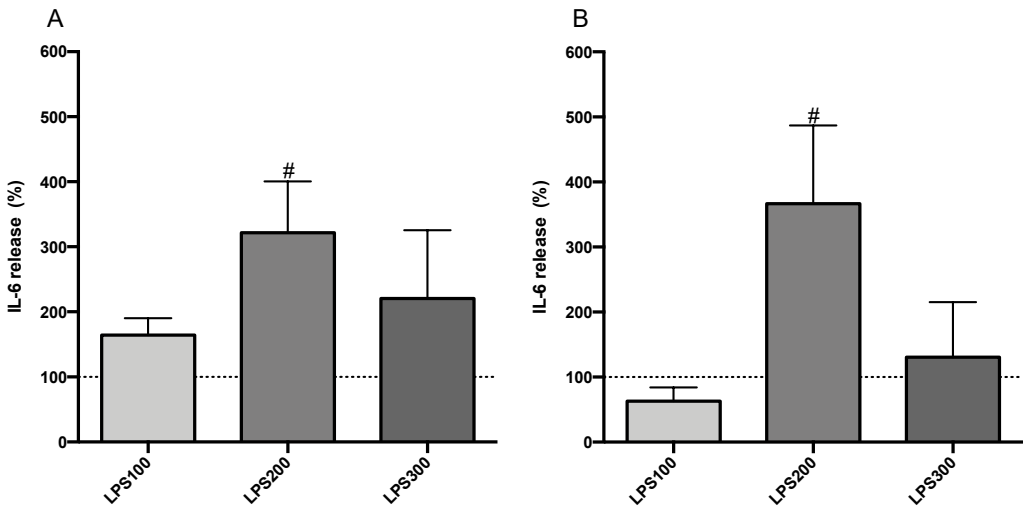

Figure 32. CF15 cells' response to LPS via IL-6 release.

Apical (A) and basolateral (B) IL-6 secretions of polarized CF15 cells. CF15 cells were grown on transwells to establish an air-liquid interface. The cells were stimulated with lipopolysaccharide (LPS) at 100, 200, or 300 ng/mL for 24 hours. At the end of this incubation period, the supernatant was collected for IL-6 analysis via ELISA, and cells were harvested for total protein concentrations measurement via Bradford assay. The IL-6 secretion amount was normalized to the protein concentration and the data represents the percentage change from control level (medium only). The dashed line denotes the IL-6 level of secretion in the control cells, corresponding to average values of 196 pg/mL and 50 pg/mL in apical and basolateral compartments, respectively. Data is presented as mean ± SD, (n=3-4 independent experiments per group). *P<0.05 vs control. LPS100: 100 ng/mL; LPS200: 200 ng/mL; LPS300: 300 ng/mL.

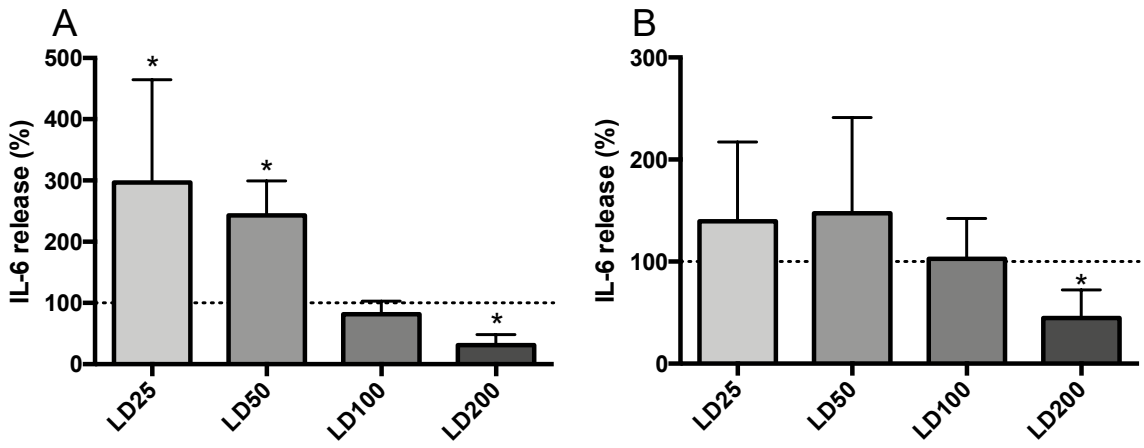

Figure 33. LPS-stimulated and DIBI treated CF15 cells response via IL-6 release.

Apical (A) and basolateral (B) IL-6 secretions of polarized CF15 cells. CF15 cells were grown on transwells to establish an air-liquid interface. The cells were challenged with lipopolysaccharide (LPS; 200 ng/mL) and treated with DIBI (25, 50, 100, 200 μM) or media alone for 24 hours. At the end of this incubation period, the supernatant was collected for IL-6 analysis via ELISA, and cells were harvested for total protein concentrations measurement via Bradford assay. The IL-6 secretion amount was normalized to the protein concentration and the data represents the percentage change from control level (medium only). The dashed line denotes the IL-6 level of secretion in the LPS cells, corresponding to average values of 526.5 pg/mL and 99.53 pg/mL in apical and basolateral compartments, respectively. Data is presented as mean ± SD, (n=3-4 independent experiments per group). *P<0.05 vs LPS. LD25: LPS+DIBI 25 μM; LD50: LPS+DIBI 50 μM; LD100: LPS+DIBI 100 μM; LD200: LPS+DIBI 200 μM.

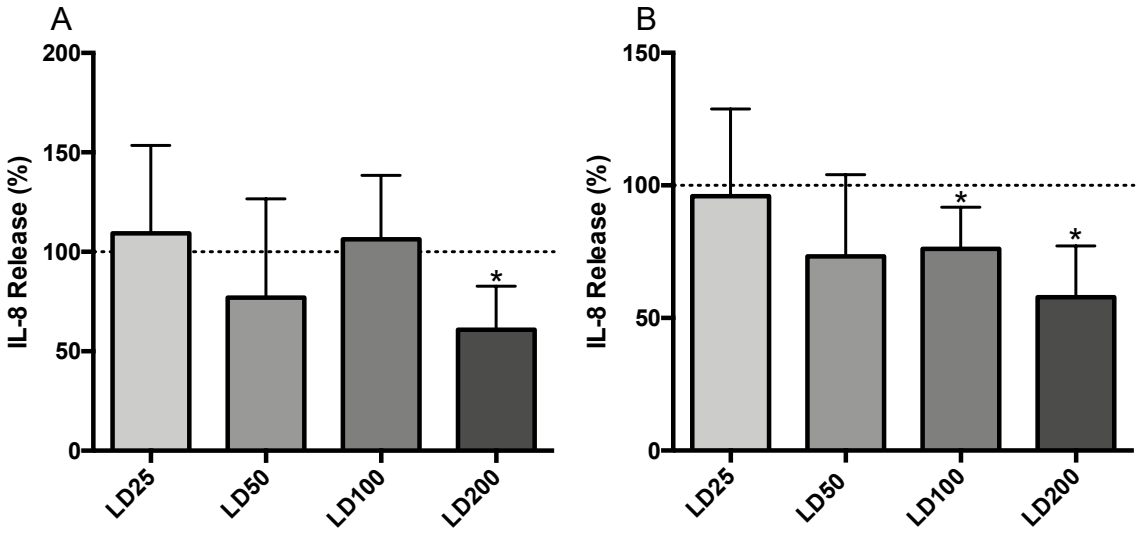

Figure 34. LPS-stimulated and DIBI treated CF15 cells response via IL-8 release.

Apical (A) and basolateral (B) IL-8 secretions of polarized CF15 cells. CF15 cells were grown on transwells to establish an air-liquid interface. The cells were challenged with lipopolysaccharide (LPS; 200 ng/mL) and treated with DIBI (25, 50, 100, 200 μM) or media alone for 24 hours. At the end of this incubation period, the supernatant was collected for IL-8 analysis via ELISA, and cells were harvested for total protein concentrations measurement via Bradford assay. The IL-8 secretion amount was normalized to the protein concentration and the data represents the percent change from control level (medium only). The dashed line denotes the IL-8 level of secretion in the LPS cells, corresponding to average values of 79.5 pg/mL and 54 pg/mL in apical and basolateral compartments, respectively. Data is presented as mean ± SD, (n=3-4 independent experiments per group). *P<0.05 vs LPS. LD25: LPS+DIBI 25 μM; LD50: LPS+DIBI 50 μM; LD100: LPS+DIBI 100 μM; LD200: LPS+DIBI 200 μM.

3.3.3 P65 analysis in CF15 cells

Given the importance of NF-κB pathway in inflammation and its hyperactivity in CF (192–194), we were interested to test whether DIBI's effects were mediated through this pathway. NF-κB signaling consists of a diverse and dynamic intracellular signaling network initiated with cytokine and PAMP binding to their respective receptors including IL-1β, TNF-α, and LPS. The NF-κB/Rel family complex resides in the cytosol as an inactive IKb complex. There are two signaling pathways: 1) canonical pathway, which is activated by inflammatory and pathogenic stimuli, and 2) non-canonical pathway, which is activated by developmental signals (195). During an infection, upon receptor activation with a pathogenic stimulus, IκBα is phosphorylated which releases P65-P50 heterodimer to translocate into the nucleus. Excess increase in p65 and subsequent activation of this pathway is observed in chronic diseases and contributes to inflammation. The complex binds to the promoter region of DNA to induce expression of cytokines, adhesion molecules, and chemokines.

The CF15 cells were fixed and immunostained with a P65 specific monoclonal antibody and revealed by a secondary antibody attached to a fluorescent tag. Only the lowest and highest DIBI doses that were studied (25 and 200 μM) were included. We developed a semi-quantitative score of P65 fluorescent signal to assess the level of NF-κB activation in response to LPS and LPS + DIBI treatments (see Figure 6 for score description).

Upon visual analysis, in the control group (medium only), there was strong P65 signal all around the nucleus and in the cytoplasm (Figures 35). Cells in the control condition had a median score of 1.5 (Figure 36). With DIBI 25 μM treatment (D25), there was an even more distinct signal in the peri-nuclear site and some signal was found inside the nucleus, indicating that P65 was activated and translocating to the nucleus. Cells within DIBI 25 μM group had a median score of 3, which was significantly higher than control score. In the DIBI 200 μM treatment group (D200), P65 signal was distributed around the nucleus with some signal inside the nucleus; these cells had a median score of 2 which was not statistically different from control group. Signal distribution with DIBI 200 μM appeared

similar to the control group, indicating that there was less NF-κB activation with DIBI 200 μM treatment compared to DIBI 25 μM.

With LPS administration, the P65 signal was mainly distributed at the perinuclear and intranuclear sites. LPS treated cells had a median score of 3, which was significantly higher than control cells' score. In the LPS + DIBI 25 μM treatment (LD25), there was an increase in P65 activation as shown by stronger perinuclear and intranuclear fluorescence and a median score of 4. Interestingly, LPS + DIBI 200 μM (LD200) P65 distribution pattern was different than with LPS alone as it appeared more spread into the cytoplasm. In the LPS + DIBI 200 μM treatment group, the P65 score was not different from LPS group, with a median of 3. These findings suggest that the effect of DIBI 25 μM is mediated through NF-κB-P65 signaling cascade, while DIBI 200 μM effect appeared to be mediated through effects on other nuclear transcription factors.

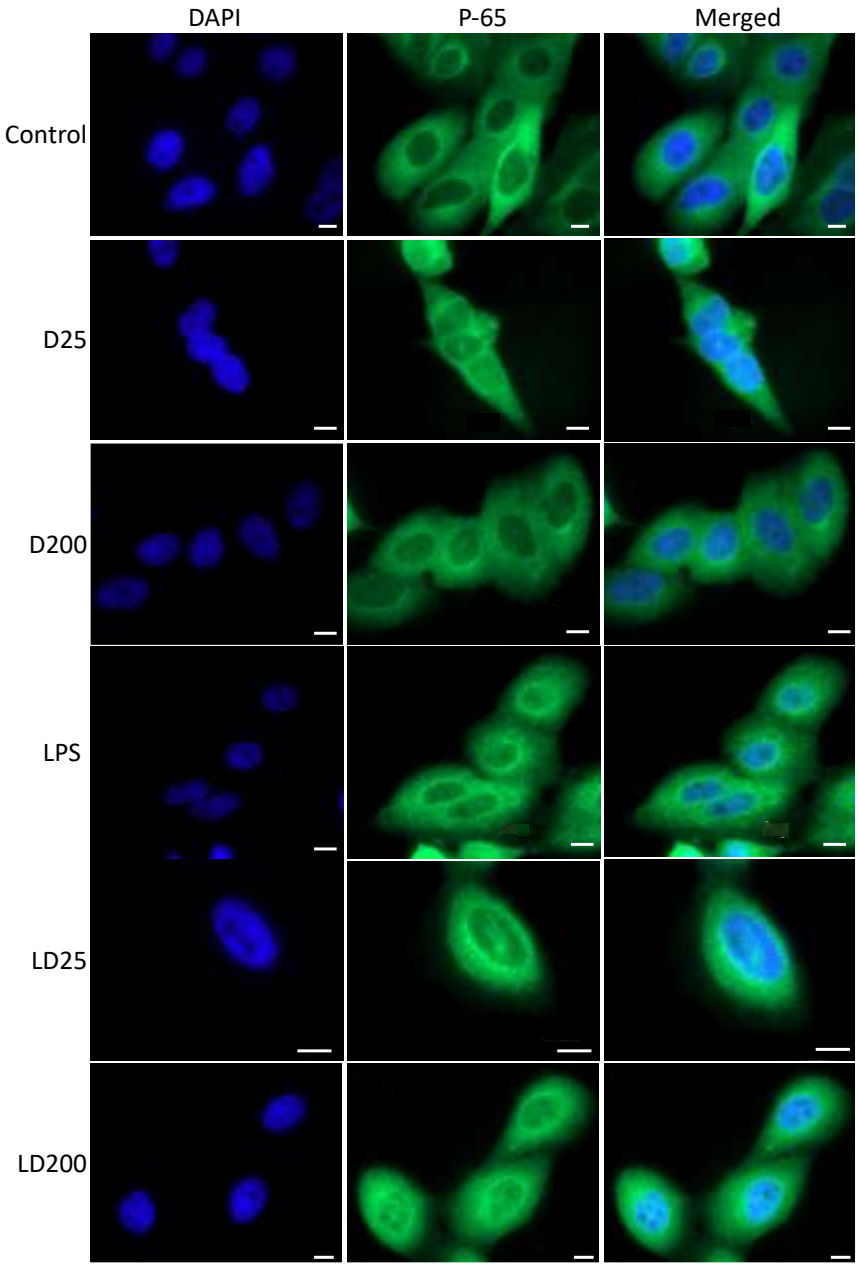

Figure 35. NF-κB P65 expression in treated CF15 cells.

Immunofluorescence images of CF15 cells. Cell nuclei were stained with DAPI (blue), and NF-κB anti-P65 primary antibody with Alexa Fluor® 488-conjugated secondary antibody (green). CF15 cells were treated with LPS (200 ng/mL), DIBI (25 and 200 μM), or LPS + DIBI as indicated for 24 hours. Images were captured with a fluorescence microscope with oil immersion under 100X objective. Scale bar = 10μm. D25: DIBI 25 μM; D200: DIBI200 μM ; LPS: Lipopolysaccharide; LD25: LPS + DIBI 25 μM; LD200: LPS+DIBI 200 μM.

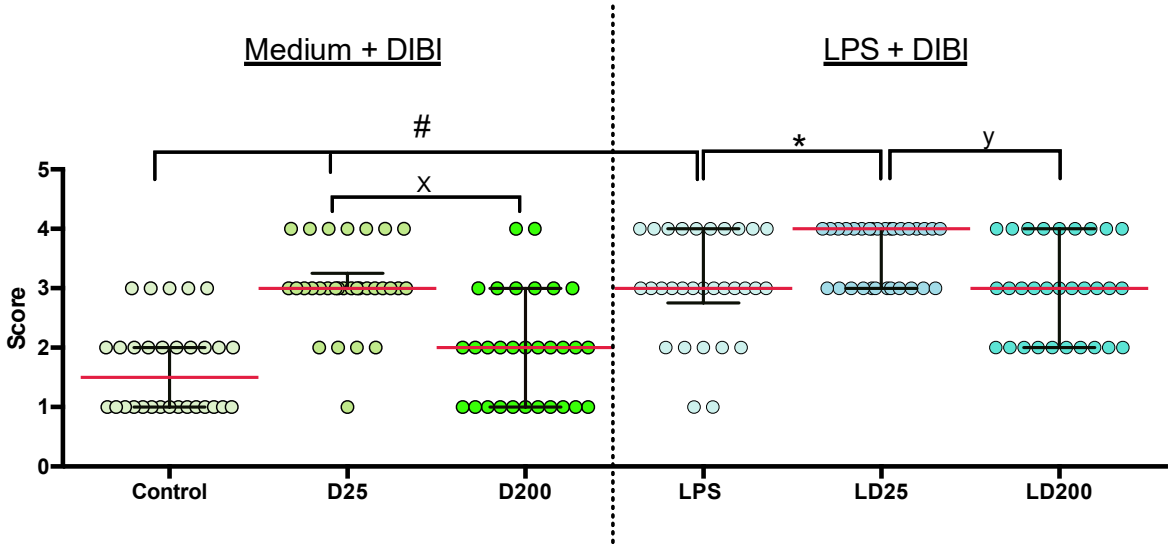

Figure 36. NF-$_K$B P65 fluorescence score of treated CF15 cells.

30 Cells were randomly selected from each treatment group and scored. The circles represent the distribution of these cells on the 1-4 scale. Data is presented as median + interquartile range; median is represented with a red line. # $p<0.05$ vs. Control, *$p<0.05$ vs. LPS; y $p<0.05$ vs LD25; x $p<0.05$ vs D200.

3.3.4 P-STAT1 and P-STAT3 analysis in CF15 cells

Next, we were interested in studying the Janus kinase (JAK)/ Signal transducer and activator of transcription (STAT) pathway, in particular STAT1 and STAT3. Previous data obtained in macrophages had shown DIBI to exert its effects by modulating STAT1 and STAT3 pathways (Hoskin laboratory unpublished data). STAT1 and STAT3 are nuclear transcription factors that are essential for maintaining homeostasis and are activated by a variety of signals.

Upon signaling through the JAK, JAK phosphorylates the cytoplasmic STATs (P-STAT) on its cytoplasmic domain. The P-STAT1 or P-STAT3 form a dimer which translocates into the nucleus and binds to the appropriate promotor region. STAT1 pathway is initiated most commonly by binding of the type I interferons (IFN-α or IFN-β) to their receptor. Upon phosphorylation, P-STAT1 dimer binds to the promoter region of interferon gamma activated sequence (GAS); or it forms a heterotrimeric transcription complex (IFN regulatory factor 9 (IRF9)) in the cytoplasm which then induces transcription of interferon stimulated response element (ISRE) in the nucleus. This results in gene expression of antiviral activity, cell proliferation, and survival regulation. P-STAT3 pathway is commonly activated by IL-6, epidermal growth factor (EGF), and IL-10. Its signaling is important for cell growth, recovery, and healing. Signaling by IL-6 induces the expression of acute response genes to induce a broad spectrum of adaptive and innate immune functions, whereas signaling by IL-10 induces the expression of anti-inflammatory genes. P-STAT3 has significant increase with tissue injury and inflammation.

To examine whether DIBI treatment was through STAT1/3 pathways, the CF15 cells were fixed and immunostained with P-STAT1 or P-STAT3 specific monoclonal antibodies and a secondary antibody attached to a fluorescent tag. The captured immunofluorescence images were scored for their corrected total cell fluorescence (CTCF). The increase in signaling indicates increase in the amount of phosphorylated form.

Starting with visual observation, P-STAT1 had similar pattern of distributions in all cells (Figure 37). To measure the signal distribution in the cells, we measured the corrected total

cell fluorescence (CTCF; Figure 38; (182). Surprisingly, the control cells (medium only) had the highest P-STAT1 activation with a CTCF of 100 ± 27.1. When DIBI was added to the medium as treatment in either in 25 μM dose (D25) or 200 μM dose (D200), the P-STAT1 activation was similar to control level with mean CTCF values of 77 ± 33.4 and 75 ± 24.5, respectively, p= 0.07. In the LPS incubated cell group, the mean CTCF was 86 ± 25.7, and the P-STAT1 activation level was not different from control levels. When DIBI treatment was added to the LPS-stimulated cells, there were no significant changes observed: LPS and DIBI dose of 25 μM (LD25) had a mean CTCF value of 75 ± 28.9 whereas LPS and DIBI dose of 200 μM (LD200) had a higher mean CTCF of 99 ± 37.8 Overall, the expression and distribution of P-STAT1 did not show a significant difference between the treatment groups, suggesting that DIBI (and LPS) do not exert their effects through P-STAT1 signalling pathway.

Visual observation of P-STAT3 target revealed that control group (medium only) had a dim fluorescence signal with a CTCF of 65 ± 22.0 (Figures 39 and 40). The cells treated with DIBI 25 μM (D25), had a slightly brighter green signal around the nucleus area as compared to control cells, with a mean CTCF of 76 ± 27.6. This difference between the control and DIBI 25 μM cells was not significant. When the cells were treated with DIBI 200 μM (D200), the signal was more activated with a mean CTCF of 105 ± 49.3 which was spread throughout the cell. This increase in P-STAT3 signal was significant from control level. Upon LPS stimulation, there was a strong P-STAT3 signal in the perinuclear area. This visual observation was consistent with the increase in the mean CTCF value of 94 ± 37.9. The LPS effect, signal localization in the perinuclear area, was weakened as the cells were treated with DIBI 25 μM (LD25). CTCF levels of LD25 cells were significantly lowered from LPS levels to 50 ± 28.5. On the contrary, the signal localization with DIBI 200 μM (LD200) was similar to LPS treated cells with a mean CTCF value of 84.3 ± 28.3.
Overall, these data suggest that in CF15 cells, DIBI treatment exerts its effects by modulating the NF-κB P65 and JAK/STAT3 pathways.

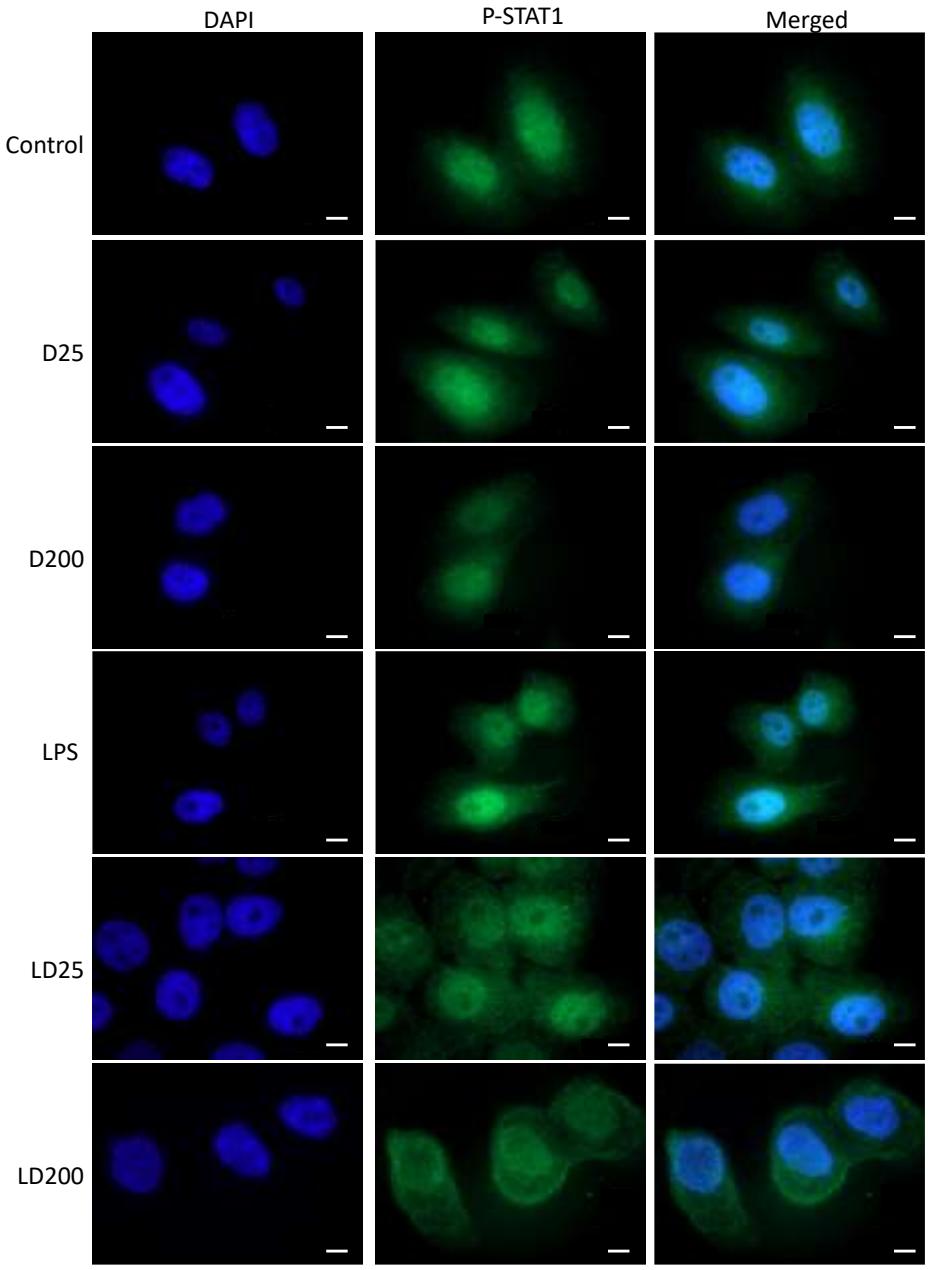

Figure 37. P-STAT1 expression in treated CF15 cells.

Immunofluorescence images of CF15 cells. Cell nuclei were stained with DAPI (blue), and P-STAT1 with anti- P-STAT1 primary antibody with Alexa Fluor® 488-conjugated secondary antibody (green). CF15 cells were treated with LPS (200 ng/mL), DIBI (25 and 200 μM), or LPS + DIBI as indicated for 24 hours. Images were captured with a fluorescence microscope with oil immersion under 100X objective. Scale bar = 10μm. D25: DIBI 25 μM; D200: DIBI200 μM; LPS: Lipopolysaccharide; LD25: LPS + DIBI 25 μM; LD200: LPS+DIBI 200 μM.

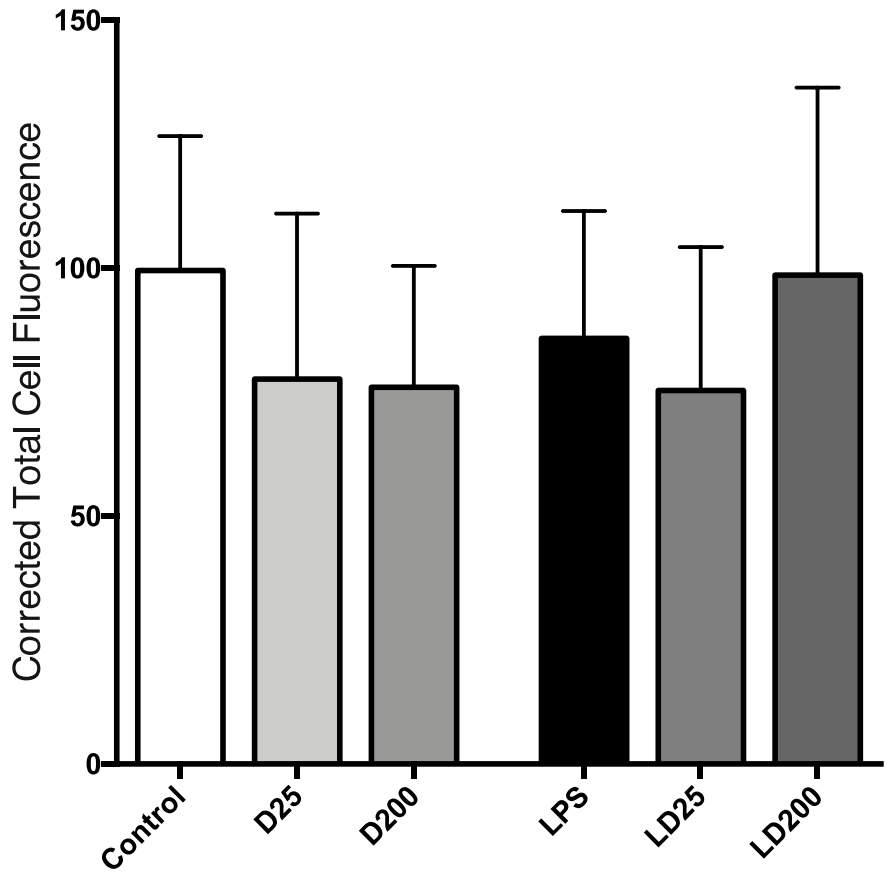

Figure 38. P-STAT1 fluorescence of treated CF15 cells.

Bar graphs represent the averages of the corrected total cell fluorescence (CTCF) for the P-STAT1 signal, measured in treated CF15 cells. 15 Cells were randomly selected from each treatment group and the CTCF was measured as follow: integrated density − (area of selected cell × mean density of background). Data is presented as mean ± SD.

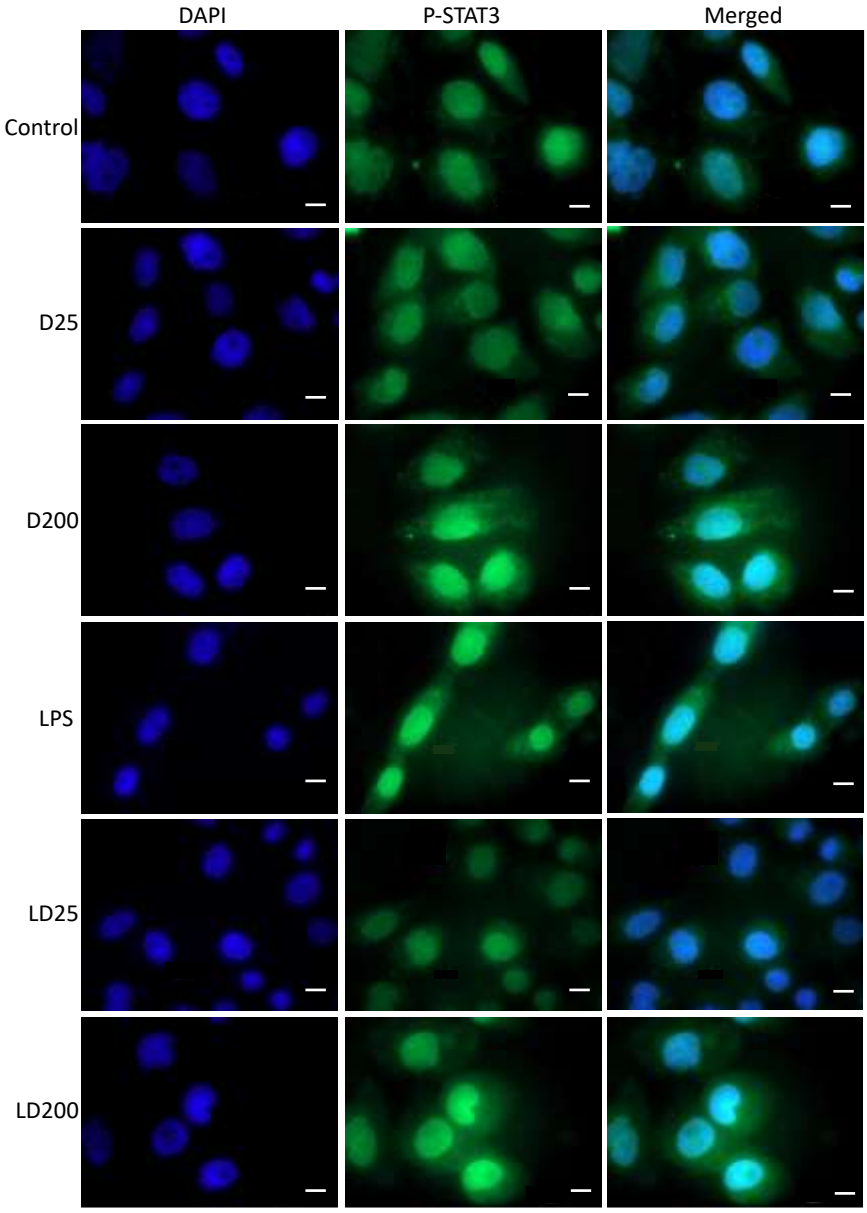

Figure 39. P-STAT3 expression in treated CF15 cells.

Immunofluorescence images of CF15 cells. Cell nuclei were stained with DAPI (blue), and P-STAT1 with anti- P-STAT1 primary unstained antibody with Alexa Fluor® 488-conjugated secondary antibody (green). CF15 cells were treated with LPS (200 ng/mL), DIBI (25 and 200 μM), or LPS + DIBI as indicated for 24 hours. Images were captured with a fluorescence microscope with oil immersion under 100X objective. Scale bar = 10μm. D25: DIBI 25 μM; D200: DIBI200 μM; LPS: Lipopolysaccharide; LD25: LPS + DIBI 25 μM; LD200: LPS+DIBI 200 μM.

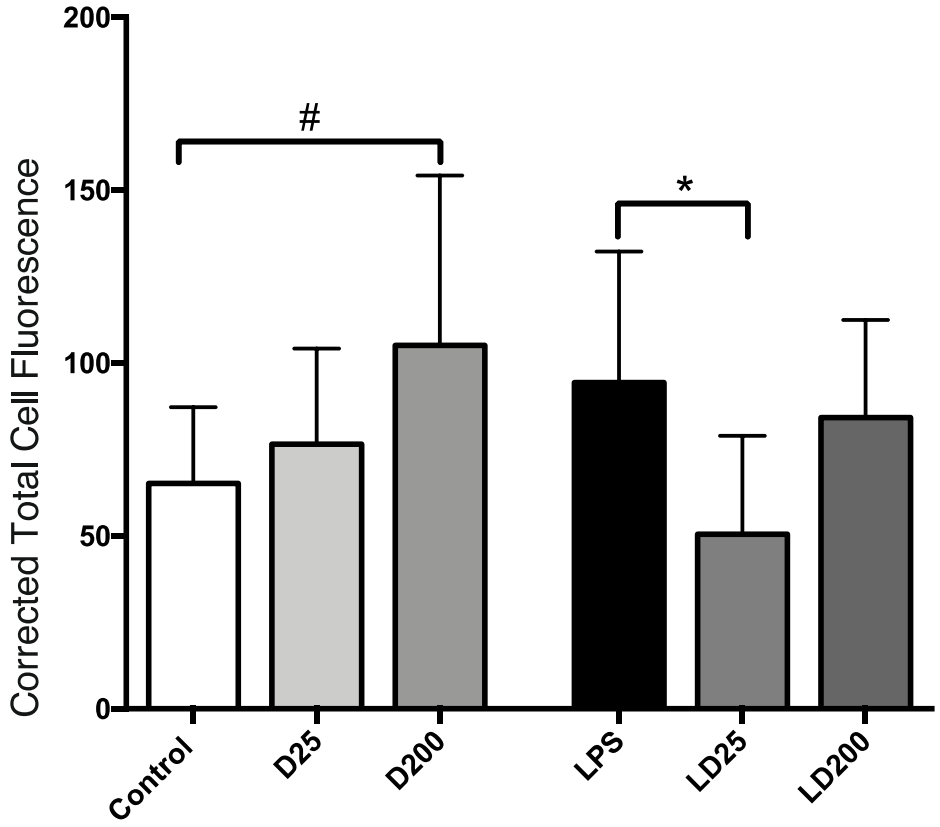

Figure 40. P-STAT3 fluorescence of treated CF15 cells.

Bar graphs represent the averages of the corrected total cell fluorescence (CTCF) for the P-STAT3 signal, measured in treated CF15 cells. 15 Cells were randomly selected from each treatment group and the CTCF was measured as follow: integrated density − (area of selected cell × mean density of background). Data is presented as mean ± SD. # $p<0.05$ vs. control, * $p<0.05$ vs. LPS.

CHAPTER 4: DISCUSSION

4.1 Iron chelation in inflammation

During systemic inflammation, iron is utilized to produce ROS. However, when the immune response is dysregulated, the overproduction of ROS leads to oxidative stress, damaging healthy tissues and further promoting the inflammatory cycle. Targeting ROS generation via iron chelators presents a novel therapeutic approach. And thus, we were determined to study iron chelation's impact on (hyper-activated) inflammation.

4.1.1 Neutrophil's cytosolic labile iron pool in response to iron chelation

Neutrophils are the most abundant leukocyte subpopulation in the circulation and together with monocytes the first to arrive at the site of inflammation. They have an array of potent weapons to eliminate pathogens and other sources of damage. As part of the innate immune system, their multi-factorial defense mechanisms include releasing powerful antimicrobial peptides (proteases and defensins), generating ROS within their phagolysosome as well as extracellularly, and creating NETs (140). Similar to other cells, neutrophils utilize iron for synthesising DNA and proteins, production of mitochondrial ATP, and for intracellular signalling.

Given that DIBI is a large polymer and most likely not able to penetrate cell membranes, we were interested in the effect of DIBI on mobilizing intracellular labile iron pool (ILIP) of neutrophils by extracellular iron chelation. Bone-marrow derived neutrophils were incubated with DIBI and challenged with LPS for four hours and underwent CA-AM assay to evaluate DIBI's effect on ILIP.

In our study, there were no changes in ILIP of neutrophils with DIBI treatments in basal condition (Figure 13). This was consistent with Greenshield *et al*.'s findings in DIBI treated MDA-MB-468 cancer cells where no changes in ILIP were observed at 4 hours of treatment (196). However, they observed reduction in ILIP with DIBI at 48 hours. We were not able to replicate this time-point in our study given the short life-span of neutrophils and lack of

biological relevance. Interestingly, addition of exogenous iron to MDA-MB-468 cells reversed the reduction observed in cell growth, confirming iron removal to be the mechanism of DIBI's observed effects (196). It is important to acknowledge the different metabolic profile of cancer cells as they have high iron requirement for their rapid growth, making them more sensitive to iron deprivation, as compared to neutrophils. Another possible explanation for the lack of change in ILIP with DIBI treatment under basal condition is the neutrophil iron storage profile. Neutrophils store a significant amount of their iron within their lysosomes due to autophagy as part of homeostasis, and the fusion of lysosomes with endosomes for ROS production (197). Lysosomes are rich in iron and are a significant contributors to the oxidative stress within the cell (198,199). CA-AM assay is limited in that it detects the cytosolic ILIP only as calcein is hydrophobic and it is almost all contained within the cytoplasm. Therefore, it does not access iron within the mitochondrial, endoplasmic reticulum, or importantly the lysosomal compartments (200). Even if higher concentrations of calcein are were used, the calcein within lysosomes would not quench iron due to the acidic environment. Thus, it is more appropriate to refer to the detected ILIP as cytosolic ILIP. In our model, there may have been changes in the total iron content of the neutrophils that was limited by the cytosolic ILIP detection. In future experiments, a method that measures the entire cellular iron content such as mass spectrometry might be more powerful for studying the total iron levels in neutrophils.

When the neutrophils were stimulated with LPS, higher doses of DIBI significantly reduced the cytosolic ILIP compared to LPS alone (Figure 13), implying that DIBI does successfully mobilize intracellular iron content in neutrophils exposed to LPS by extracellular chelation. It has been shown that iron deprivation can impair neutrophils' antimicrobial effector function including reduced ROS production, primary granule degranulation, phagocytosis, and NETs release (201). For example, DFO was also observed to inhibit ROS and NET generation (201). However, in the context of systemic inflammation, reduced ROS production by neutrophils should not be viewed as a detrimental side effect. In fact, it provides a novel approach to alleviating neutrophilic-inflammation as observed in hyper-inflammatory immune states (202).

4.1.2 Systemic inflammation

The endotoxemia model of systemic inflammation enabled us to study the acute hyper-inflammatory state of sepsis without the need of infectious conditions. This model has the advantage of administration of a reproducible amount of toxin in a controlled manner and it reproduces similar inflammatory pathway activation as clinical sepsis (120). The goal of this model was to evaluate the impact of iron chelation on systemic inflammation as found under conditions such as early sepsis. The administration of the LPS dose of 5 mg/kg with two hours observation time replicates the hyper-immune activation of sepsis, without inducing septic shock. The selected DIBI dose was chosen as it demonstrated the most anti-inflammatory capacity in a previous study (186). We evaluated this effect through IVM, cytokine measurements, and histology.

Part of the inflammatory response is releasing mediators to recruit leukocytes to the site of inflammation. Endothelial cells upregulate the expression of adhesion molecule receptors to enable the leukocyte-endothelial binding as they arrive through the blood stream to extravasate into the tissue. The stages consist of rolling, adhering, firmly adhering, and translocation into tissue. Since firm adhesion is the final and most critical step for consequent transmigration (Figure 3), we defined leukocyte adhesion in V1 collecting venules to be our primary parameter of assessing leukocyte activation. Given that the intestine is considered as a driving force in sepsis pathology and relatively easy to access surgically, it was selected as the organ of interest for IVM (203).

4.1.2.1 Leukocyte-endothelial interactions

Consistent with previous reports (204–206), LPS increased leukocyte adherence in V1 vessels. LPS activates TLR4 and a downstream inflammatory cascade that results in adhesion molecule upregulation (207). DFP, DFO, and DIBI treatments demonstrated anti-inflammatory properties as they reduced LPS-induced leukocyte adhesion (Figure 14, part A). This can be attributed to their ability to bind iron and subsequently reduce ROS levels, therefore interfering with the inflammatory cascade early on (208,209). In a comparable murine model of endotoxemia, similar results were obtained with iron chelation treatment where hyperactivation state of sepsis was attenuated and survival outcome was increased

(208,210). Though iron chelation treatments were dose matched for iron-binding capacity, DFX and DIBI had a substantial difference in their capacity to impact leukocyte adhesion. This can be explained by iron binding affinity and thermodynamic stability difference between these iron chelators. The iron binding affinity of DFX is intermediate, between DFP and DFO's (211), whereas DIBI has a higher affinity for iron as compared to both DFP and DFO (unpublished data by Holbein, Chelation Partners Inc.). Additionally, it is important for iron chelators to hold iron in a non-redox active state to prevent iron's participation in biological reactions. DFX has a weak metal-binding pyridinium group, which holds iron in a redox-active state (211); this is in contrast to DIBI which holds iron in a redox-inactive state (170, and unpublished data by Holbein, Chelation Partners Inc.). This finding highlights the importance of chemical and biological properties of iron chelators on their function.

In the V3 vessels, there was higher baseline adhesion of leukocytes in the control group which reduced the difference to the LPS-induced response (Figure 14, part B). The increased baseline adhesion can be explained by the different shear forces in the V3 post-capillary venules as compared to V1 venules. Due to the reduced blood flow in smaller venules, the shear forces are weaker, thus increasing the likelihood of leukocyte adherence. Surprisingly, the three classical iron chelators increased leukocyte adhesion in V3 venules compared to untreated LPS treated animals, whereas DIBI treatment did not show such an effect (Figure 14, part B). This finding can be explained by the lower levels of soluble ICAM measured in the plasma of DIBI treated animals (Figure 17, part F). ICAM is an adhesion protein expressed on endothelial cells upon inflammatory activation to facilitate the transmigration of leukocytes into tissues. DIBI's ability to reduce adhesion in both vessels demonstrates anti-inflammatory effects. This is in agreement with other studies where DIBI reduced the LPS-induced adhesion in capillary and post-capillary venules (213,214). DIBI binds to iron with higher affinity than the other iron chelators and it effectively reduces hydroxyl radical formation (186). This can reduce downstream inflammatory cascade activation as hydroxyl serves as a pro-inflammatory messenger. However, these observations can also be explained by considering other properties of these chelators aside from their iron binding capacity such as their biological, pharmacological,

and chemical profile. DIBI's backbone PVP molecule has a plasma volume expanding effect and acts like a colloid, which are known to have anti-inflammatory effects (215–218). Thus, DIBI's active backbone makes it more effective at modulating the immune response than just exerting iron-chelation effects. Reduction in leukocyte adhesion must be interpreted carefully as severe reduction can be harmful if it impedes adequate immune response and impairs pathogen clearance; this highlights the need for a model with active infection present.

The increase in leukocyte adhesion after an inflammatory stimulus is inversely correlated with a decrease in the number of rolling leukocytes. With LPS administration and inflammatory activation, the number of rolling leukocytes was decreased in both, V1 and V3 venules, and was not recovered to control level with any of the iron chelators treatments (Figure 15). Relevant to this stage of leukocyte activation is the adhesion molecule, P-selectin, expressed on activated endothelial cells. There were no changes observed in soluble P-selectin levels measured in the plasma. These results suggest that iron chelation does not modulate the rolling stage and instead exerts its effects at the adhering stage of leukocyte activation.

4.1.2.2 Capillary perfusion

The microcirculatory system includes vessels of <100μm diameters including arterioles, capillaries, and venules. This system is critical for oxygen and nutrient delivery to the tissues. The main cellular players are endothelial cells, smooth muscle cells, RBCs, leukocytes and platelets (219). In sepsis, disparities and mismatch exist between macro-hemodynamic and microcirculatory study observations, making the latter a more reliable prognostic factor for systemic inflammation and the development of organ failure. An example is shunt formation that reduces capillary perfusion and lowers oxygen saturation despite achieving normal systemic microcirculatory targets (220,221). Within a clinical setting, microcirculatory impairment can be assessed through intravital imaging of superficial, e.g. mucosal capillary perfusion such as the sublingual microcirculation. Sublingual microcirculation has been shown to parallel the changes in the intestine and kidneys of sepsis patients, thus being representative of various organ levels (222–224). Additionally,

there is a correlation between intestinal and sublingual microcirculation shown in sepsis patients after surgery (224). Microcirculatory changes can worsen the sepsis outcome and cause organ failure independent from systemic macrocirculatory parameters (225,226). Interestingly De Backer et al., have shown that microcirculatory alterations improve in sepsis survivors while they remain impaired in non-survivors (227).

In this work, in both the muscle and mucosa layers, the FCD was reduced with LPS administration (Figure 16). LPS is known to cause major impairment in capillary perfusion. Interestingly, all the iron chelators improved the FCD, which is viewed as a beneficial outcome (Figure 16). This improvement is consistent with previous findings, where DIBI restored the LPS-induced impairment of FCD in murine endotoxemia (124) and murine uveitis (125). In another study, metronidazole, which also reduces ROS production, improved the intestinal capillary perfusion of septic rats (228). Reduction in inflammatory mediators can impact microcirculation and induce FCD changes through multiple ways. Microcirculation is complex and during sepsis factors such as glycocalyx degradation, reduced RBC deformability, and endothelial dysfunction can impact the inflammatory status (101). We propose that iron chelation, through reduction of ROS-generating pathways and reduction of leukocyte-endothelial interactions, contribute to the observed FCD improvement.

4.1.2.3 Cytokines

As part of the inflammatory response, immune and non-immune cells detect DAMPs and PAMPs through their PRRs. Downstream effects lead to cytokine and chemokine release as well as adhesion molecules upregulation to orchestrate an effective response. In sepsis, the host immune response is highly activated resulting in excess pro-inflammatory (IL-1β, TNF-α, IFN- γ) and anti-inflammatory mediator (IL-10, IL-4, and TGF-β) release. This is described as cytokine storm, which is associated with increased mortality (229). Although this serves as a hallmark of sepsis, the gene expression, cytokine levels, and immune response is highly variable between patients with sepsis (230), making it difficult to diagnose and treat. We were interested in how iron chelation impacts the release of these cytokines in plasma.

TNF-α and IL-1β are pyrogenic cytokines and work synergistically to increase vascular permeability, activate coagulation, and potentiate inflammatory response (231). Both cytokines amplify the inflammatory cascade by activating macrophages to release pro-inflammatory mediators including ROS (232). Their peak plasma level is estimated to be 60-90 minutes post LPS administration (80), which is earlier than sample collection timepoint chosen for this study (3 hours post-LPS).

TNF-α, produced predominantly by macrophages, is an early regulator of immune response and thus it orchestrates the downstream cytokine cascade (233). Its functions consist of upregulating the expression of adhesion molecules on endothelial cells, and triggering ROS release in activated neutrophils, both of which promote inflammation (80). IL-1β is released, largely by macrophages, as a proprotein and is cleaved into its active form by caspase-1. It induces fever, activates coagulation, and enhances leukocyte chemotaxis and extravasation. Similar to TNF-α, it causes amplification of downstream pro-inflammatory response. In this study, LPS administration increased TNF-α and IL-1β plasma levels compared to control (234). Interestingly, DIBI and DFX further increased their levels compared to LPS (Figure 17, parts A and C). One possible explanation is that perhaps DIBI modulated the kinetics of TNF-α and IL-1β release. DIBI might delay the peak of these two early cytokines, therefore we measured higher levels at a later time point (204). This "slow down" of inflammation would also explain the lower leukocyte adhesion level observed in the V1 and V3 vessels.

IFN-γ is released in response to macrophage-derived cytokines (TNF-α) and is mainly produced by natural killer cells and T lymphocytes. It is found in high levels in serum of sepsis patients in the early, hyper-inflammatory phase, and has shown to have potential for treatment of immune-paralysis (235,236). Another important inflammatory mediator, IL-6, is released in response to LPS, IL-1β, and TNF-α and can conduct both pro- and anti-inflammatory effector functions. It induces the acute phase response and it connects the innate and adaptive arms via activation of T and B lymphocytes. IL-6 elevation in sepsis patients is associated with the development of multiple organ failure, septic shock, sepsis severity and mortality rate (237–242). In our systemic inflammation model, treatment with

the three classical iron chelators further increased INF-γ and IL-6 levels. However, DIBI was able to prevent higher than LPS-induced levels of IFN-γ and IL-6 release (Figure 17, parts B and D).

Early during systemic (hyper-)inflammatory response in sepsis, anti-inflammatory cytokines such as IL-10 are released (80). IL-10, produced by CD4+ Th2 cells, monocytes, and B cells, inhibits phagocytosis and antigen presentation to the adaptive immune cells. As a sign of dysregulated immune response in the early, hyper-inflammatory phase of sepsis, high levels of IL-10 were associated with poor outcome including organ failure and death (243,244). In the later stages of sepsis, increased IL-10 levels are interpreted as anti-inflammatory response. In this study, IL-10 levels at 2 hours and 45 minutes were increased with DIBI and DFX treatment from control levels (Figure 17, part E), which could imply beneficial effects on systemic (hyper-) inflammation.

Analyzing the cytokine levels allowed a better understanding of the inflammatory response. Further studies with plasma collection from multiple time-points through our experimental procedure are needed to confirm the change in cytokine release kinetics in response to DIBI that we hypothesized. In these experiments, ideally animals should be divided into IVM or cytokine measurement groups. Though care is taken to minimize the trauma, IVM is an invasive technique. Some of the mice were not able to survive its duration and thus blood could not be collected from them. This was also a limitation of the present study as samples were not collected from the sickest animals in the untreated group (LPS). By having IVM as a separate subset of LPS group, blood can be taken from mice at multiple timepoints with less mortality. This also enables cytokine measurements in the sickest animals as multiple sample collection timepoints are in place.

4.1.2.4 Histology

Epithelial cells are integral to the cellular and structural integrity of innate immunity. We are only just beginning to appreciate their immunomodulatory role as we learn more about their dynamic behaviour. Upon activation through PRR signalling, they release antimicrobial peptides (defensins), pro-inflammatory cytokines, and can recruit leukocytes.

At the core, they are well known for their role in barrier defence in protecting tissues from the external environment and pathogens. Their apical TJs, made of claudin and attachment adhesion molecules, prevents commensal microflora, pathogens, and harmful agents from translocating to the mucosa and the systemic circulation. In sepsis, mucosal permeability is impaired, and this increases para- and trans-cellular bacterial translocation resulting in secondary pathogen invasion and potentially worsening of multi-organ failure (245,246). The endotoxemia model induces systemic inflammation and barrier dysfunction through pro-inflammatory mediator activation, and accelerating epithelium apoptosis, and TJ damage (247). The TJ dysfunction in sepsis has been attributed to increased iNOS expression (248) and is mediated though the TLR-4/MYD88 response (249). Furthermore, as oxidative stress is involved in the pathology of sepsis, antioxidant therapies have the potential to reduce this pathology. Pre-treatment with MitoQ, a mitochondrial antioxidant maintained structural integrity of the intestine and alleviated the leukocyte recruitment, and inflammatory cell infiltration in a LPS-induced model of sepsis (250). At the cellular level, MitoQ treatment also increased the expression of TJ proteins, and up regulation of antioxidant genes.

In the endotoxemia model used in the present study, we observed minimal histological damage at baseline as assessed by the Chiu score, most likely related to the surgery and sample collection process (Figure 18). LPS administration did not cause additional damage within three hours of observation time. This can be explained by the low LPS dose and the short duration of the model. Higher doses of LPS, at least twice of the amount used in this model, resulted in intestinal epithelial cell apoptosis and shedding, and villus shortening at 1.5 hours. Five hours post-LPS administration intestinal permeability was largely increased (251). In another study of LPS-induced intestinal inflammation, the histological injury, extensive ulceration, oedema and structural damage of the jejunum epithelium by LPS increased the Chiu score after 6 hours (252). To better understand the effect of iron chelation treatment, it would be valuable to re-assess treatment impact and efficacy in a sepsis model of intestinal epithelium damage at later time points or with higher doses of LPS.

Despite the advantages of being a reproducible and relatively simple model of systemic inflammation, the endotoxemia model has some limitations. This model lacks an active infection, which is required to study the full spectrum of immune response. Additionally, infections tend to develop gradually with PAMP release over time, which is in contrast with endotoxemia's one-time rapid LPS trigger (253). As such, we were interested in investigating iron chelation effect in a clinical infection model of sepsis.

4.2. Iron chelation in infection

4.2.1 CASP

4.2.1.1 Leukocyte-endothelial interactions

To have a better understanding of iron chelation, the same IVM parameters were selected in CASP model to complement findings from endotoxemia. In the sham group, there was baseline leukocyte adhesion due to the surgical trauma that the mice underwent. As previously shown, we saw a rise in the number of adhering leukocytes with CASP surgery (191,254). In V1 vessels, DFP, DFO, and DIBI reduced leukocyte adhesion compared to untreated CASP animals (Figure 19, part A). This reduction was not a complete reversal to the level of sham animals, which was not the goal of the experiment. The goal was to reduce leukocyte hyper-activation yet allowing the immune system to generate a response to the present infection. Our results are in agreement with previous findings. Leukocyte recruitment was reduced with DIBI alone or in combination with antibiotic co-treatment in the same CASP model (191). In a separate study, antioxidant therapy using DFO and N-acetylcysteine reduced oxidative stress, neutrophil infiltration, and increased survival drastically in a CLP model of systemic infection (255). Moreover, DFO administration improved survival in a sepsis model of CLP (256).

Similar to the endotoxemia experiments, we did not observe significant changes in leukocyte adhesion in V3 vessels (Figure 20, part A). Again, this is most likely due to the different shear forces in those smaller, post-capillary venules, complicating any potential beneficial effects of experimental therapies.

CASP-induced reduction in the numbers of rolling leukocytes did not return to the levels of sham animals regardless of the selected treatment (Figures 19 and 20, part B). This is similar to our findings in endotoxemia and correlates with the unchanged plasma levels of P-selectin confirming the idea of iron chelation modulating the firm adhesion stage of leukocyte extravasation.

4.2.1.2 Capillary perfusion

As expected, we saw a reduction in capillary perfusion of the intestinal wall in untreated CASP animals. In the muscle layer, there was high variability within the treatment groups (Figure 21, part A). In the mucosa layer, DFX and DFP treated animals showed higher FCD values, compared to DFO and DIBI treatment (Figure 21, part B). FCD is a multi-factorial parameter and leukocyte adhesion represents only one of the contributing factors. Edema (compressing microvascular blood flow), redistribution of blood flow, and increased microvascular permeability are other important contributors (101). Furthermore, the region of interest for microscopy was the ileum, making it in close proximity to the ascending colon where the stent was placed, potentially interfering with the recording. Thus, FCD results, as a secondary outcome parameter, should be taken as a preliminary data and investigated in the future with more animals per group to better understand changes in FCD.

4.2.1.3 Plasma cytokine measurements

Given the beneficial effects seen with DIBI treatment in endotoxemia, we were interested in comparing cytokine levels in the CASP model. Thus, plasma samples were collected at 9 hours post-CASP surgery and the previously measured cytokines were analyzed. In sham animals, both the pro- and anti-inflammatory cytokine levels were low. Compared to the endotoxemia model, there were major differences observed in sepsis groups. In general, the cytokine levels were lower in the CASP model (Figure 22). The higher levels of early cytokines release and the proposed kinetics shift with DIBI administration were not observed here. There are multiple explanations for the observed results including timing, site of inflammation, and route of administration. In endotoxemia, the peak of early pro-inflammatory cytokines is reported to be at 60 to 90 minutes post-LPS administration (80). Our samples were collected after this peak at 3 hours after LPS administration. In the CASP group, dependent on fecal matter leakage, the

cytokine levels are expected to rise at 3 hours and the peak has been shown to be at 12 hours after surgery (257–259), while plasma was collected at 9 hours post-CASP surgery. This can explain the low levels of cytokines detected in the CASP model.

In the endotoxemia model, the inflammatory trigger, LPS, was in the systemic circulation. Thus, DIBI was also administered IV to provide systemic treatment. In the CASP model, the infection was localized in the peritoneum and the abdominal cavity. Hence DIBI was administered IP to maximize its effect at the site and reduce systemic (side) effects. Measuring tissue cytokine levels would have been helpful in CASP model to better understand the impact of iron chelation locally.

The route of administration of DIBI may impact its mechanism of action and shift in cytokine release. DIBI is a large polymer (9.5 kilodalton) and likely most of its molecules were retained in the abdominal cavity and not absorbed in systemic circulation with IP administration in the CASP model (212). Importantly, when double doses of DIBI were given in the same CASP model, IV administration of the second dose induced highest cytokine release in the plasma (186). This mimicked the endotoxemia result with DIBI (IV), increasing the cytokine levels. Further experiments are essential to investigate the kinetics of DIBI (both IV and IP administration) in a CASP model with plasma collection at multiple time points.

4.2.1.4 Histology

Again, we observed minor baseline inflammation in the sham group (Figure 23). This could be due to the CASP surgery and IVM that the animals underwent. In the CASP group there was further intestinal damage present. The histological changes observed in the present study are higher compared to the damage observed by Islam *et al*., who observed minimal damage 16 hours post-poly-bacterial sepsis in mice (191). However, in an interferon-therapy study by Hu *et al*., intestinal damage was significantly increased (Chiu score of 3), 5 hours after CLP surgery (260).

DFX, DFP, and DFO treatments were able to improve this CASP-induced damage (Figure 23). Though there was a reduction with DIBI, it was not significant. Why other chelators were

superior to DIBI in this matter may be due to their molecular size. As DIBI molecules are bigger than DFO, DFP, and DFX, they may not have been internalized and absorbed into the intestinal tissue. In contrast, the three classical iron chelators were most likely absorbed directly into the intestine and were able to modulate intestinal damage directly.

4.2.1.5 Bacterial enumeration and microbiome analysis

As expected, the bacterial burden increased with CASP surgery (Figure 24). In PLF and blood samples, there were no significant changes with the iron chelation therapy. However, given the logarithmic dimension of the results, there was a trend of bacterial burden reduction by DFO and DIBI. This ability to reduce the bacterial load is even more meaningful since there was ongoing fecal leakage for the entire duration of the model.

Previously, in other studies the antibacterial effects of iron chelators have been tested. In the CASP model of sepsis, the combination of DIBI and imipenem (beta-lactam antibiotic) reduced the bacterial burden in both blood and plasma samples compared to the untreated group (191). However, DIBI alone was not able to improve this bacterial clearance. Compared to other iron chelators, DIBI has demonstrated superior anti-infective properties. In a study by Holbein and Orduna, DIBI effectively limited the growth of opportunistic pathogens *Candida albicans* and C. *vini* over a four-day period, though DFP and DFO were not able to do so (261). This effect of DIBI was reversed upon iron supplementation, emphasizing DIBI's iron-specific effects. Moreover, DIBI (but not DFP or DFO) enhanced the efficacy of azoles (anti-fungals) in reducing the growth of clinical isolated of C. *albicans* (where resistance to anti-fungals is recorded) and *in vivo* model of vaginitis (262). DIBI demonstrated synergistic effects with fluconazole to lower the vaginal fungal burden, but alone, it did not reduce it (262).

The gut microbiome is a dynamic microbial network and is constantly adapting to environmental changes and host factors. During the early stage of poly-bacterial abdominal infection induced by microbiota, the aerobic bacteria such as E. Coli replicate and colonize the tissues. This tissue damages reduces the oxygen-reduction potential of the oxygenated tissue (264). In addition to infection-induced hypoxia, the microcirculatory disruptions

observed in sepsis further create an anaerobic environment where the obligative anaerobes, such as *Bacteroidaceae* can colonize, replicate, and lead to the secondary infection observed in the chronic stage of infection (264). As iron is a requirement for almost all forms of life including bacteria, we expected iron deprivation (via iron chelation) to create changes in the species diversity and dominance of the microbiome. Thus, the microbiome composition of the bacteria in PLF samples was analyzed. Low environmental iron creates competition, leaving some species susceptible and others resistant to these changes. Though there was variability within the groups, we observed some overarching trends.

In our samples, the *Bacteroidaceae* family from *Bacteroidia* class formed the majority of the microbial composition (Figure 25, part A). *Bacteroidia* are Gram-negative, obligate anaerobic bacteria that are part of the gut microbiome. Though they are normally commensals, if the intestinal barrier is compromised such as through gastrointestinal rupture or intestinal surgery, they can translocate to the blood stream or surrounding tissues. In this family, *Bacillus fragilis* are opportunistic aerotolerant pathogens that cause infections within peritoneal cavity and are considered the leading anaerobic bacteria in sepsis and bacteremia (263). Species from the *Bacteroidaceae* family are known to have the highest rates of antibiotic resistance of all anaerobic pathogens (264). Thus, with the rise of antibiotic resistant strains (to beta-lactams and aminoglycosides), their need for iron can be a target of adjuvant therapies. During extra-intestinal infections, *Bacteroidaceae* family acquire iron from heme and inorganic sources, though the exact mechanisms are under investigation (265). We did not observe changes in this class. However, in a CASP experiment with a second dose of DIBI administered IV, *Bacteroidia* were almost wiped out entirely (186). Perhaps *Bacteroidia* are more susceptible to iron deprivation through the bloodstream than in the abdominal cavity, given the low penetration of DIBI into the intestine.

The second most common family of bacteria in the PLF sample analyzed were the *Enterobacteriaceae* from the *Gammaproteobacteria* class. This large and diverse Gram-negative family includes highly virulent human pathogens that release potent immune-stimulatory toxins. They include *Salmonella, Shigella*, *Vibrio cholera*, and *Yersinia*

species. Three of the most common causative agents for abdominal bacterial sepsis belong to this family: *E. coli*, *P. aeruginosa, and Klebsiella* (266), all of which have evolved complex iron-acquisition systems (44, 200, 265).

Interestingly, DFO treated animals had the least proportion of *Gammaproteobacteria* class and *Enterobacteriaceae* family. This is in contrast to what has been reported before. As iron contributes to virulence and pathogenicity, DFO use in patients with Beta-thalassemia is associated with high risk for *Y. enterocolitica* septicemia (268). *Y. enterocolitica* utilize iron bound to other siderophores (DFO) for growth *in vitro*; whereas DFP did not promote *Y. enterocolitica* growth most likely due to DFP's higher affinity for iron and non-microbial origin, making it harder for *Y. enterocolitica* to access the bound-iron (268).

And finally, *Clostridia* and *Bacilli*, both Gram-positive species, were the two other major groups. *Clostridia*, obligate anaerobes, includes *C. dificile* species which is the most common hospital-acquired infection and it is part of the antibiotic resistance threat (269, 270). It can cause much more severe sepsis if it is the causative agent. *Clostridia* class also includes *C. perfringens. C. perfringens* is responsible for food poisoning and causes necrosis upon endospore release into wounds. In our findings, there was higher distribution of *Clostridia* with DFO and DFP treatments; this change in microbiome diversity could be detrimental to health and thus DFO and DFP's effects on microbiota must be further explored. Intravenous DIBI has been shown to eradicate their distribution (186).

Bacilli are aerobes and facultative anaerobes. Though they are part of the homeostasis and gut microbiome, some of their species such as *B. cereus* induce bacteremia and peritonitis in immunocompromised patients (271). DIBI did not change *Bacilli* diversity in CASP though DFO and DFX appear to have increased *Bacilli* proportion. Although not detected in the PLF samples analyzed, within this class, *Staphylococcus* imposes a major health burden on the health care system. They are a problem in surgical-site infections, and ventilator-associated infections, which makes them the second most common causative agents of hospital acquired infections (272–274). Vancomycin resistant and methicillin resistant *S. aureus* are extremely difficult to treat and need immediate attention. DIBI has effectively been shown

to reduce *S. aureus* growth *in vivo* and *in vitro* (275, 276). DFX therapy appear to increase this *Streptococcaceae* bacterial population, which is one of the most common Gram-positive agents in abdominal infection.

Taken together, there were only subtle changes in the PLF of septic mice with iron chelation therapy (Figure 25). This can be due to the short duration of the experiments. As mentioned, many bacteria have iron acquisition systems and thus an acute iron deprivation may not display the complete impact of iron chelation therapy on the bacterial diversity and distribution. However, it is interesting that in a previous study with the same model when a second IV dose of DIBI was administered, the composition of the PLF samples changed considerably (186). These preliminary findings highlight the complexity of targeting iron as a dual-purpose target in host and the infection agents. As mentioned, to assess whether these changes are beneficial or harmful, longer experimental timelines are required. And importantly, in order to draw accurate conclusions, more animals must be included to be able to comprehend changes deeper within the taxonomic groups such as the genus and species levels.

One limitation of this model was the continuous fecal matter leakage through the stent. Although this helped to mimic the heterogeneity in infection severity observed in sepsis patients, it made it difficult to analyze the treatments' effects in the context of infection severity. We were not able to adjust the readouts based on the amount of fecal matter leakage present. To overcome this limitation, pre-measured feces can be injected as part of fecal slurry model (277, 278). This would ensure consistent bacterial inoculum in each mouse. However, this model does not represent the heterogeneity observed in sepsis progression.

Up to now, we have observed improvements of inflammatory parameters with DIBI administration. As iron deprivation can impact the ability of the host response to clear pathogens, we were curious to observe long time effects of DIBI and its overall impact on the immune system in survival experiments. Which is why in the next model, we introduced

a new surgical intervention step to fix the "leak" in an attempt to make it more clinically viable. Given the synergy of anti-infective drugs with DIBI and the requirement of antibiotics as part of standard care, we proposed to include an antibiotic in our next study.

4.2.2 CASP-I

One downside of alleviating the early hyperinflammatory stage of sepsis is the potential interference with the immune system's ability to clear pathogens. This should be taken into consideration when proposing novel therapeutic options. Previous studies targeting oxidative stress have been shown to improve survival (256, 279). Thus, we were interested in how DIBI's anti-inflammatory effects impact recovery over time in extended time sepsis model. To do this, we modified the CASP model to include an additional surgical step to fix the source of infection through stent removal. This model (CASP-I) mimics clinical approach to treatment of abdominal sepsis where the perforation is surgically addressed in combination to drug administration (257).

4.2.2.1 MSS score and survival

The MSS score provides a way to assess morbidity in mice. Without treatment, animals with CASP-I induced sepsis had a rapid decline of health leading to high MSS scores and death within 24 hours (Figures 26 and 27). Mice treated with DIBI did not improve the MSS scores and survival significantly. However, DIBI not worsening the outcome as compared to no treatment is an important finding, since the reduction in ROS level by DIBI did not impair immune defence during this infection.

Per clinical (human) sepsis guidelines (116), antibiotics are considered standard therapy and should be used in experimental treatment studies as well (129). When DIBI was administered in combination with the antibiotic, imipenem, survivability of the mice increased even more than with imipenem alone. These mice also displayed healthier behaviour as indicated by their lower MSS scores throughout the observation period. Previously it was shown that DIBI as co-treatment with imipenem in CASP model

additively reduced the leukocyte recruitment (191). These results suggest that DIBI does not interfere with imipenem's function and it has potential for acting as adjuvant with antibiotic therapy.

Although addition of DIBI to imipenem was not statistically superior to imipenem only, there was a trend of improvement observed in the combination therapy. Within the first 24 hours, the survival curves overlap, and similar death rate is observed. However, after the 24-hour timepoint, more animals survived for longer with the combination treatment. Given the high mortality and rapid progression of sepsis, increasing the median survival time of even a few hours represents a meaningful improvement; in patients with sepsis a difference of few hours can be amplified through supportive therapies. This indicates the beneficial efficacy of DIBI as an adjuvant therapy. Given the half-life of DIBI and imipenem, future investigation would be more translatable to clinical setting if the treatments, including DIBI, were repeated throughout the timeline as needed, similar to the care provided to septic patients.

4.2.2.2 Bacterial enumeration

To investigate iron chelation effects on bacterial burden, PLF fluid was collected at the time of intervention surgery. Combination treatment of imipenem and double dose DIBI significantly reduced aerobic gram-negative and total anaerobic bacterial burden (Figure 28, parts B and C). This finding was promising as combination of DIBI (especially double dose) and imipenem, demonstrated synergistic effects, supporting DIBI's potential as an adjuvant. Additionally, repeating DIBI dose (and furthering iron restriction), did not impair innate immunity's ability to respond to the infection.

In the context of anaerobic bacteria, higher iron deprivation in combination with imipenem reduced the bacterial burden. In severe infections such as sepsis, there is a dynamic shift in the bacterial species in response to changing environment, such as lower oxygen levels in the environment. Given the reduction in oxygen in tissues (hypoxia), facultative anaerobes are at an advantage for survival (280), though some aerobic and facultative anaerobic bacteria can shift to anaerobic metabolism (277, 278). The reduction in anaerobic bacterial

burden with imipenem and double dose DIBI in the present study highlights the beneficial effect of adjuvant therapy for targeting suspected anaerobic bacterial infection.

Imipenem belongs to the carbapenem class of antibiotics, which are considered our last resort antibiotic due to their broad spectrum of activity and relatively low resistance (283). However, it is concerning that even carbapenems efficacy is reducing with antibiotic resistant strains in nosocomial infections, posing one of the greatest health threats (284). The observed additive antibacterial effect of (double dose) DIBI and imipenem in our study, can be even more meaningful since in clinical setting, there is emerging antibiotic resistance which renders imipenem less effective. There is an urgent need to develop novel therapies to boost antibiotic efficacy. It would be interesting to investigate DIBI's effects in sepsis models with resistant strains of bacteria.

4.2.3 Limitation of the *in vivo* murine models

Some common limitations can be identified in the utilized animal models. In the models, young, healthy, male mice were used. In sepsis, age is a risk factor with older population being more vulnerable to developing sepsis after an infection. Additionally, these patients often suffer from co-morbidities such as hypertension, auto-immune diseases, chronic obstructive pulmonary disorder, and chronic renal failure, which can be positively correlated with mortality and ICU-readmission (71, 72, 281, 282). Additionally, we did not control for sex in our study. Thus, in future experiments, older male and female mice with comorbidities should be investigated. Though murine models are effective in assessing the effect of treatments and they are genetically and physiologically similar to humans (287), they are not a substitute to human models. Thus, findings must be carefully interpreted for transition into clinical trials. Another limitation is the short time frame of these models which did not comprehensively assess the long-term effects of iron chelation. Even though iron chelation would most likely be administered as an acute treatment, long-term effects of reducing systemic iron levels should be closely investigated as sepsis patients are at risk for infection progression and having an immunocompromised state. DIBI's short half-life can be beneficial as its plasma levels (and degree of iron chelation) can be better controlled.

4.3. Iron chelation in inflammation and infection

We utilized CF as experimental model to study the role of iron in an inflammatory environment combined with bacterial toxin exposure. Patients with CF suffer from chronic pulmonary inflammation and recurrent infections in their airways. CFTR dysfunction not only impairs the MCC, but it also affects immune functions. Airway epithelial cells are closely involved in the pulmonary inflammatory response. Already under physiological conditions, those cells show high baseline immune activation as they are continuously exposed to antigens from the external environment. In the CF airways, the epithelial cells are constitutively in pro-inflammatory state (138, 287). Despite this heightened response, the pathogen clearance is not effective, and the chronic inflammation can lead to pathological changes of the lung tissue. Thus, alleviation of this baseline inflammation is a potential target for treatment. The CF pathology is partly driven by oxidative stress. The

goal of this part of the project was to study the impact of iron chelation on immune activation under the specific condition of combined inflammatory state and infectious challenge.

4.3.1 Low-dose iron chelation has pro-inflammatory effects

In our study, the incubation of unstimulated CF15 cells with lower doses of DIBI increased IL-6 secretion from the apical and basolateral membranes (Figure 30). Additionally, NF-κB P65 signalling was increased with low dose (25 μM) of DIBI treatment (Figure 36 and Figure 41, part A). This increased inflammatory response to iron chelation, has also been shown previously. In a study by Nelson *et al.* conducted in human respiratory epithelial cells, iron chelation by enterobactin (siderophore produced by *Enterobacteriaceae*) initiated an inflammatory response (289). In a different study conducted in intestinal epithelial cells, DFO triggered the activation of inflammatory pathways (290). These findings suggest that iron homeostasis disruption can act as a pro-inflammatory signal to warn against iron-consuming microbial invasion.

Upon establishing an effective LPS stimulation dose, transcription of pro-inflammatory genes was induced (Figure 32). Incubation of CF15 cells in LPS and low dose of DIBI, further amplified IL-6 secretion (Figure 33). This change was most likely conducted through the NF-κB signalling pathway, as higher P65 signalling was observed (Figure 36). Interestingly, P-STAT3 signal was reduced with low dose (25 μM) of DIBI treatment (Figure 40). P-STAT3 is a pleiotropic nuclear factor and has activation-specific response. Although IL-6 cytokine signals through the STAT3 pathway, we cannot exclude the presence of other cytokines and mediators such as IL-10 that may have been produced by the CF15 cells. By analyzing a bigger array of inflammatory cytokines and chemokines, we would better understand the orchestrated (pro- and anti-) inflammatory responses to iron chelation treatment by CF epithelial cells.

In our model we did not observe IL-8 changes with DIBI 25 μM treatment (Figures 31 and 34). This finding was unexpected as CF patients have elevated IL-8 secretions in their airways. One possible explanation is the dysregulated immune response by epithelial cells

in CF: the high baseline activation of pro-inflammatory pathways in CF cells could result in smaller (fold-change) magnitude of response to inflammatory stimulations, as compared to non-CF cells. Carrabino *et al*. measured the activity of NF-κB and IL-8 secretions of explant cultures of nasal epithelial cells from CF and non-CF patients at baseline and with P. *aeruginosa* and IL-1β/H_2O_2 co-stimulation (137). This study demonstrated the higher baseline activation of NF-κB and IL-8 secretion in the CF cells, compared to non-CF cells. However, once the cells were stimulated, the response in NF-κB activity and IL-8 release was much higher in the non-CF cells. Additionally, it suggested that basal dysregulation in IL-8 secretion is linked to the hyperactivity of NF-κB in CF cells. These findings can explain why in our study CF15 cells did not change IL-8 secretion with DIBI 25 μM treatment. The higher P65 signal observed with DIBI 25 μM can also confirm the suggested link between NF-κB hyperactivity and IL-8 dysregulation. In a separate study by Massengale *et al*., (291) airway epithelial CF cells had a lower induction of IL-8 mRNA and proteins levels in response to IL-1β stimulation, as compared to its isogenic CFTR-corrected control. Taken together, the changes in P-STAT3 activation and IL-6 secretion suggest that low dose (25 μM) of DIBI has pro-inflammatory effects (Figure 41).

4.3.2 Anti-inflammatory effects of high dose iron chelation treatment

Iron regulation is a dynamic process and when high amounts of extracellular iron are chelated, such as with higher dose of DIBI, intracellular iron can be mobilized to regain homeostasis. High dose of DIBI (200 μM) in unstimulated cells did not change the cytokine secretion (Figures 30 and 31). However, P-STAT3 signal was increased (Figure 40), perhaps indicating activation of anti-inflammatory signalling, but had no impact on the measured cytokines' secretion. Once the cells were stimulated with LPS, high-dose DIBI treatment reduced the LPS-induced IL-6 and IL-8 secretion levels (Figures 33 and 34). The underlying mechanisms may be due to reduction of iron-dependant protein tyrosine phosphatase activity (292), reduced nuclear factor synthesis (293), and or decreased ROS-induced upregulation of IL-6 and IL-8. These results, taken together highlight the anti-inflammatory potential of higher dose of DIBI and its utility to alleviate the immune

response (Figure 42). These results also highlight the importance of dose studies specially when the target, such as iron, is an important player in various other cellular pathways.

To our knowledge, this is the first time that P65, P-STAT1, and P-STAT3 were studied by immunofluorescence in CF15 cells. In the present study, no changes were observed with P-STAT1 (Figure 38). This may be due to the low interferon secretion by the CF15 cells in response to LPS stimulation. Further studies analyzing a more comprehensive set of cytokines will shed a light on these responses. Another possible reason can be the high baseline activation of the CF15 cells which lowered the sensitivity of detecting differences between treatments by immunofluorescence. Performing quantitative methods such as Western blot analysis or q-PCR are needed to establish a deeper understanding of changes in the amounts of nuclear factors and signalling proteins. By measuring proteins at various stages of the intracellular signalling cascade, such as STAT3 and P-STAT3, we can better understand the stage(s) that iron chelation is modulating the pathway.

When the same LPS dose was used to stimulate non-CF airway epithelial cells, Calu-3 cells, their response was not as potent as CF15 cells' response (data not shown). Studies with effective stimulation of Calu-3 cells report using higher doses of LPS (294,295). This highlights the immunomodulatory impact of defective CFTR channel and the pro-inflammatory profile of CF15 cells. This must be considered for future investigations as healthy epithelial cells with functional CFTR channels are not appropriate for direct comparison. Instead, pharmacological interventions with the CFTR channel in the same cell line would yield more accurate findings (291).

In our study the CF15 cells were polarized, enabling measurement of IL-6 and IL-8 secretion from both apical and basolateral compartments. Direct comparison of the absolute values revealed higher IL-6 and IL-8 secretion on the apical side. This polarized response creates a chemotactic gradient, promoting trans-epithelial migration of leukocytes into the apical compartment from basolateral compartment. This is consistent with previous studies which demonstrated a polarized response in human airway epithelial cells during inflammation (296–298). In the context of CF, where high neutrophil recruitment and

activation are responsible for inducing damage (neutrophilic-inflammation), the reduction of IL-6 and IL-8 observed by higher dose of DIBI can be beneficial by alleviating this response. In future investigations, CF15 cells can be co-cultured with immune cells such as neutrophils to have a better understanding of iron chelation's polarized impact.

4.3.3 Future direction: Iron chelation as a potential anti-microbial therapy in CF

Given that iron contributes to pathological leukocyte activation through increased ROS production and serves as a nutrient for invading pathogens, iron chelation provides a unique opportunity to explore both targets in CF. Though diverse set of pathogens colonize these airways, *Pseudomonas aeruginosa* remains the most common infection (299). Airways of CF patients have higher iron and ferritin concentration which may contribute to the persistent *P. aeruginosa* infection and biofilm formation (300, 301). Interestingly, these higher levels of iron are present even before *P. aeruginosa* infection, suggesting that CFTR-defect induces excess iron secretion, promoting their colonization (300). As part of innate immune defence, host iron-acquiring proteins, such as siderocalin, are found in abundance in the airways to reduce iron bioavailability and bind to siderophores, such as enterobactin (289). Additionally, local hepcidin expression in the airways exerts direct antimicrobial effects and serves as an iron detoxifier (302, 303). In order to understand these interactions between the lung microbiome and the host, more biologically relevant systems are preferred for investigation. For example, co-culturing *P. aeruginosa* and epithelial cells, or epithelial and immune cells (with bacterial-culture supernatants) can enhance our understanding of these interactions and treatment effects. DIBI's biochemical properties makes it possible to pursue iron chelation therapy in infection context as it does not supply the pathogens with iron and renders it inaccessible.

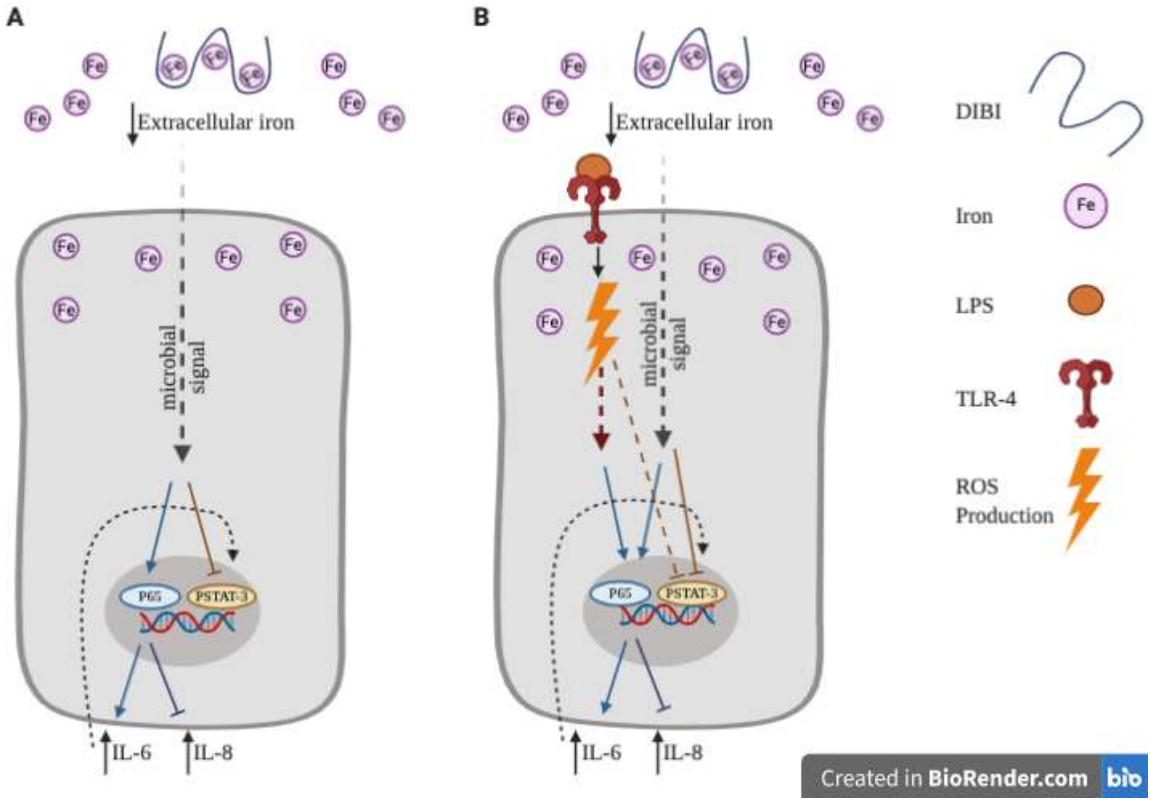

Figure 41. Proposed mechanism of low dose iron chelation with DIBI (25 μM) and its effect on cytokine response.

A) Low dose iron chelation, similar to bacterial growth, results in reduction of extracellular iron concentration; this can be perceived as a microbial signal. Through activation of nuclear factor pathways, such as NF-κB, p38 or ERK1/2, pro-inflammatory cascades are initiated resulting in increased release of IL-6 (290). Although iron chelation can induce IL-8 release, over activated NF-κB activity in CF can impair IL-8 release, resulting in no change. IL-6 is an inducer of STAT3 pathway. However, iron chelation can interfere with STAT3 activity, thus no changes were observed with low dose DIBI. B) LPS binds to TLR-4, activating downstream nuclear factor pathways, such as NF-κB. This also leads to generation of reactive oxygen species (ROS). These pathways support the IL-6 synthesis induced by low dose iron chelation (304). Abbreviations: Fe: iron; LPS: Lipopolysaccharide; TLR-4: Toll-like receptor 4; ROS: reactive oxygen species.

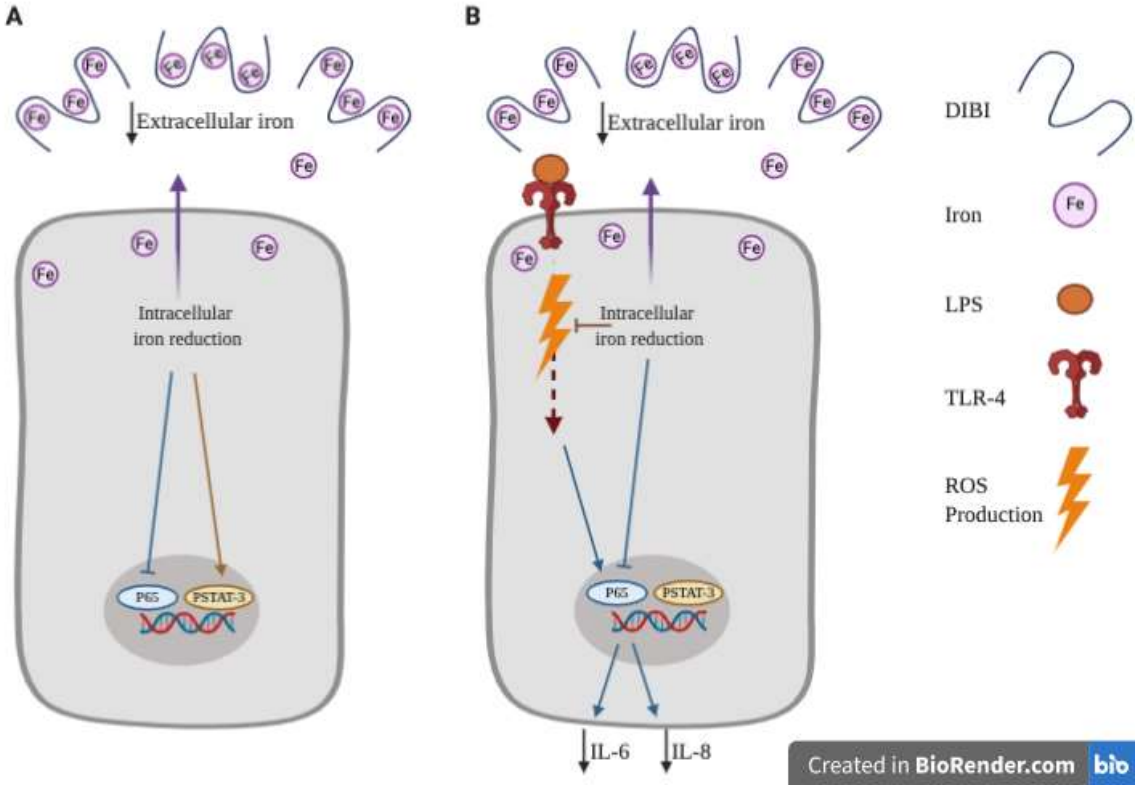

Figure 42. Proposed mechanism of high dose iron chelation with DIBI (200 μM) and its effect on cytokine response.

A) High dose iron chelation does not only reduce extracellular, but also intracellular iron levels. This results in decreased intracellular nuclear factor synthesis (293) which can explain why NF-κB activity was not initiated with DIBI 200 μM, as compared to microbial signal indicated by lower iron chelation dose. Neither IL-6 nor IL-8 secretions were changed from basal conditions. P-STAT3 activation can induce anti-inflammatory and pro-healing pathways as triggered by low intracellular iron levels (305). B) High dose iron chelation reduced LPS-induced IL-6 and IL-8 release by direct (iron-related reduction of nuclear factor synthesis) and indirect (decreased ROS-induced up-regulation of IL-6 and IL-8) mechanisms due to intracellular reduction of iron levels (293). Abbreviations: Fe: iron; LPS: Lipopolysaccharide; TLR-4: Toll-like receptor 4; ROS: reactive oxygen species.

4.4 Conclusion

The present dissertation investigated the impact of iron chelation on both the immune response and bacterial growth with a potential for therapeutic application in the context of sepsis and CF. We employed various models of inflammation and infection both *in vivo* and *in vitro*. This was the first time that the three FDA approved iron chelators deferoxamine (DFO), deferiprone (DFP), and desferasirox (DFX) and the novel synthetic iron chelator, DIBI, were tested in experimental inflammation and infection models.

In experimental systemic inflammation, DFO, DFP, and DIBI effectively reduced excessive immune activation as shown by attenuated leukocyte-endothelial interactions and restored capillary perfusion in the intestinal microcirculation using intravital microscopy. Plasma inflammatory mediator levels were altered with DIBI, indicating potential kinetic modulation of mediator secretion. In experimental infection, we observed reduction of leukocyte-endothelial interactions with DFO, DFP, and DIBI treatment. Of these chelators, DFO and DFP also attenuated intestinal histological damages. Iron chelation therapy did not impact bacterial growth, which can be explained by the model limitations. In survival experiments, DIBI treatment in combination with the antibiotic, imipenem, lowered mortality and reduced bacterial growth. Importantly, iron chelation did not impair the host immune response to bacterial infection in the survival experiments. Our findings in CF15 cells as a model of airway inflammation and infection also suggest that iron chelator effects are dose-specific. We observed anti-inflammatory effects of DIBI with the higher doses studied whereas lower doses induced a pro-inflammatory response, which appeared to be signalled through NF-κB and JAK/STAT3 pathway.

In conclusion, these results support the immuno-modulatory role of DIBI, in particular its therapeutic potential to alleviate hyper-activated immune response. Additionally, these results suggest a promising role for DIBI as an adjunct anti-bacterial treatment, including therapeutic options for antibiotic-resistant infections. Further pharmacological and immunological investigations are required before clinical studies can be considered.

REFERENCES

1. Morgan JW, Anders E. Chemical composition of Earth, Venus, and Mercury. Proc Natl Acad Sci. 1980;77(12):6973–7.
2. Ganz T. Systemic iron homeostasis. Physiol Rev. 2013;93(4):1721–41.
3. Zhang C. Essential functions of iron-requiring proteins in DNA replication, repair and cell cycle control. Protein Cell. 2014;5(10):750–60.
4. Gunshin H, Mackenzie B, Berger U V., Gunshin Y, Romero MF, Boron WF, et al. Cloning and characterization of a mammalian proton-coupled metal-ion transporter. Nature. 1997;388(6641):482–8.
5. Leidgens S, Bullough KZ, Shi H, Li F, Shakoury-Elizeh M, Yabe T, et al. Each member of the poly-r(C)-binding protein 1 (PCBP) family exhibits iron chaperone activity toward ferritin. J Biol Chem. 2013;288(24):17791–802.
6. Skikne BS, Whittaker P, Cooke A, Cook JD. Ferritin excretion and iron balance in humans. Br J Haematol. 1995 Jul;90(3):681–7.
7. Hunt JR, Roughead ZK. Nonheme-iron absorption, fecal ferritin excretion, and blood indexes of iron status in women consuming controlled lactoovovegetarian diets for 8 wk. Am J Clin Nutr. 1999;69(5):944–52.
8. Donovan A, Lima CA, Pinkus JL, Pinkus GS, Zon LI, Robine S, et al. The iron exporter ferroportin/Slc40a1 is essential for iron homeostasis. Cell Metab. 2005 Mar 1;1(3):191–200.
9. Flowers CH, S SB, Covell AM, Cook JD. The clinical measurement of serum transferrin receptor. J Lab Clin Med. 1989;114(4):368–77.
10. Hentze MW, Muckenthaler MU, Galy B, Camaschella C. Two to tango: regulation of mammalian iron metabolism. Cell. 2010 Jul 9;142(1):24–38.
11. Knutson MD. Iron transport proteins: Gateways of cellular and systemic iron homeostasis. J Biol Chem. 2017;292(31):12735–43.
12. Knutson MD, Oukka M, Koss LM, Aydemir F, Wessling-Resnick M. Iron release from macrophages after erythrophagocytosis is up-regulated by ferroportin 1 overexpression and down-regulated by hepcidin. Proc Natl Acad Sci U S A. 2005;102(5):1324–8.

13. Laftah AH, Ramesh B, Simpson RJ, Solanky N, Bahram S, Schümann K, et al. Effect of hepcidin on intestinal iron absorption in mice. Blood. 2004;103(10):3940–4.
14. Ramey G, Deschemin J-C, Durel B, Canonne-Hergaux F, Nicolas G, Vaulont S. BRIEF REPORTS Hepcidin targets ferroportin for degradation in hepatocytes. Haematol |. 2010;95(3).
15. De Domenico I, Zhang TY, Koening CL, Branch RW, London N, Lo E, et al. Hepcidin mediates transcriptional changes that modulate acute cytokine-induced inflammatory responses in mice. J Clin Invest. 2010;120(7):2395–405.
16. Katsarou MS, Latsi R, Papasavva M, Demertzis N, Kalogridis T, Tsatsakis AM, et al. Population-based analysis of the frequency of HFE gene polymorphisms: Correlation with the susceptibility to develop hereditary hemochromatosis. Mol Med Rep. 2016 Jul 1;14(1):630–6.
17. Katsarou MS, Papasavva M, Latsi R, Drakoulis N. Hemochromatosis: Hereditary hemochromatosis and HFE gene. In: Vitamins and Hormones. 2019. p. 201–22.
18. Chen L, Deng H, Cui H, Fang J, Zuo Z, Deng J, et al. Inflammatory responses and inflammation-associated diseases in organs. Oncotarget. 2018;9(6):7204–18.
19. Chaplin DD. Overview of the immune response. J Allergy Clin Immunol. 2010 Feb;125(2):S3.
20. Ribet D, Cossart P. How bacterial pathogens colonize their hosts and invade deeper tissues. Vol. 17, Microbes and Infection. Elsevier Masson SAS; 2015. p. 173–83.
21. Akira S, Takeda K. Toll-like receptor signalling. Nat Rev Immunol. 2004 Jul 1;4(7):499–511.
22. Kawasaki T, Kawai T. Toll-like receptor signaling pathways. Front Immunol. 2014 Sep 25;5:461.
23. Oliveira Júnior JO de, Portella Junior CSA, Cohen CP. Inflammatory mediators of neuropathic pain. Rev Dor. 2016;17(1):35–42.
24. Cui H, Kong Y, Zhang H. Oxidative stress, mitochondrial dysfunction, and aging. J Signal Transduct. 2012;2012:1–13.
25. Schrader M, Fahimi HD. Peroxisomes and oxidative stress. Biochim Biophys Acta - Mol Cell Res. 2006 Dec 1;1763(12):1755–66.

26. Snezhkina A, Kudryavtseva A, Kardymon O, Savvateeva M, Melnikova N, Krasnov G, et al. ROS generation and antioxidant defense systems in normal and malignant cells. Oxid Med Cell Longev. 2019 Aug 5;2019:6175804.
27. Nunes P, Demaurex N, Dinauer MC. Regulation of the NADPH oxidase and associated ion fluxes during phagocytosis. Traffic. 2013 Aug 1;14(11):1118–31.
28. Hassan TH, Badr MA, Karam NA, Zkaria M, El Saadany HF, Rahman DMA, et al. Impact of iron deficiency anemia on the function of the immune system in children. Med (United States). 2016;95(47).
29. Nathan C. Specificity of a third kind: reactive oxygen and nitrogen intermediates in cell signaling. J Clin Invest. 2003 Mar 15;111(6):769–78.
30. Mortadza SAS, Wang L, Li D, Jiang LH. TRPM2 channel-mediated ROS-sensitive Ca2+ signaling mechanisms in immune cells. Front Immunol. 2015 Aug 7;6(JUL):407.
31. Tschopp J, Schroder K. NLRP3 inflammasome activation: The convergence of multiple signalling pathways on ROS production? Nat Rev Immunol. 2010;10(3):210–5.
32. Xu Q, Choksi S, Qu J, Jang J, Choe M, Banfi B, et al. NADPH oxidases are essential for macrophage differentiation. J Biol Chem. 2016;291(38):20030–41.
33. Mantovani A, Biswas SK, Galdiero MR, Sica A, Locati M. Macrophage plasticity and polarization in tissue repair and remodelling. Vol. 229, Journal of Pathology. Wiley-Blackwell; 2013. p. 176–85.
34. Griess B, Mir S, Datta K, Teoh-Fitzgerald M. Scavenging reactive oxygen species selectively inhibits M2 macrophage polarization and their pro-tumorigenic function in part, via Stat3 suppression. Free Radic Biol Med. 2020;147:48–60.
35. Zhang Y, Choksi S, Chen K, Pobezinskaya Y, Linnoila I, Liu ZG. ROS play a critical role in the differentiation of alternatively activated macrophages and the occurrence of tumor-associated macrophages. Cell Res. 2013;23(7):898–914.
36. Galli F, Battistoni A, Gambari R, Pompella A, Bragonzi A, Pilolli F, et al. Oxidative stress and antioxidant therapy in cystic fibrosis. Biochim Biophys Acta - Mol Basis Dis. 2012 May;1822(5):690–713.

37. Prauchner CA. Oxidative stress in sepsis: Pathophysiological implications justifying antioxidant co-therapy. Burns. 2017;43(3):471–85.
38. Weiss G, Ganz T, Goodnough LT. Anemia of inflammation. Blood. 2019;133(1):40–50.
39. Mateen S, Moin S, Khan AQ, Zafar A, Fatima N. Increased reactive oxygen species formation and oxidative stress in rheumatoid arthritis. PLoS One. 2016;11(4).
40. Huang WJ, Zhang X, Chen WW. Role of oxidative stress in Alzheimer's disease. Biomed Reports. 2016;4(5):519–22.
41. Kurian GA, Rajagopal R, Vedantham S, Rajesh M. The Role of oxidative stress in myocardial ischemia and reperfusion injury and remodeling: revisited. Oxid Med Cell Longev. 2016:1656450.
42. Ener K, Keske M, Aldemir M, Özcan MF, Okulu E, Özayar A, et al. Evaluation of oxidative stress status and antioxidant capacity in patients with painful bladder syndrome/interstitial cystitis: preliminary results of a randomised study. Int Urol Nephrol. 2015;47(8):1297–302.
43. Prauchner CA. Oxidative stress in sepsis: Pathophysiological implications justifying antioxidant co-therapy. Burns. 2017 May;43(3):471–85.
44. Reid DW, Anderson GJ, Lamont IL. Cystic fibrosis: ironing out the problem of infection? Am J Physiol - Lung Cell Mol Physiol. 2008 Jul;295(1):L23-24.
45. Tyrrell J, Callaghan M. Iron acquisition in the cystic fibrosis lung and potential for novel therapeutic strategies. Microbiology. 2016 Feb;162(2):191–205.
46. Hilty M, Burke C, Pedro H, Cardenas P, Bush A, Bossley C, et al. Disordered microbial communities in asthmatic airways. PLoS One. 2010Jan; 5(1):e8578.
47. Pulvirenti G, Parisi GF, Giallongo A, Papale M, Manti S, Savasta S, et al. Lower airway microbiota. Front Pediatr. 2019;7(393):1–10.
48. Padilla C, Lobos O, Hubert E, Poblete F, Navarro A, Nuñez L. In vitro antibacterial activity of the peptide PsVP-10 against *Streptococcus mutans* and *Streptococcus sobrinus* with and without glycocalyx. Int J Antimicrob Agents. 2006;27(3):212–6.
49. Kerr JR. Suppression of fungal growth exhibited by *Pseudomonas aeruginosa*. J Clin Microbiol. 1994;32(2):525–7.

50. Hogan DA, Vik Å, Kolter R. A *Pseudomonas aeruginosa* quorum-sensing molecule influences Candida albicans morphology. Mol Microbiol. 2004 Oct 15;54(5):1212–23.
51. Yoon MY, Lee K, Yoon SS. Protective role of gut commensal microbes against intestinal infections. J Microbiol. 2014;52(12):983–9.
52. Rowland I, Gibson G, Heinken A, Scott K, Swann J, Thiele I, et al. Gut microbiota functions: metabolism of nutrients and other food components. Eur J Nutr. 2018;57(1):1–24.
53. Lloyd CM, Marsland BJ. Lung homeostasis: influence of age, microbes, and the immune system. Immunity. 2017;46(4):549–61.
54. Nauseef WM. Identification and quantitation of superoxide anion: essential steps in elucidation of the phagocyte "respiratory burst." J Immunol. 2014;193(11):5357–8.
55. Hoffmann MH, Griffiths HR. The dual role of reactive oxygen species in autoimmune and inflammatory diseases: evidence from preclinical models. Free Radic Biol Med. 2018 Sep;125:62–71.
56. Gardiner GJ, Deffit SN, McLetchie S, Pérez L, Walline CC, Blum JS. A role for NADPH oxidase in antigen presentation. Front Immunol. 2013 Sep 23;4(SEP):295.
57. Hennigar SR, McClung JP. Nutritional Immunity: starving pathogens of trace minerals. Am J Lifestyle Med. 2014;10(3):170–3.
58. Xiao X, Yeoh BS, Saha P, Olvera RA, Singh V, Vijay-Kumar M. Lipocalin 2 alleviates iron toxicity by facilitating hypoferremia of inflammation and limiting catalytic iron generation. BioMetals. 2016;29(3):451–65.
59. Wessling-Resnick M. Iron homeostasis and the inflammatory response. Annu Rev Nutr. 2010;30(1):105–22.
60. Trivier D, Davril M, Houdret N, Courcol R. Influence of iron depletion on growth kinetics, siderophore production, and protein expression of Staphylococcus aureus. FEMS Microbiol Lett. 1995;127(3):195–200.
61. Freidank HM, Billing H, Wiedmann-Al-Ahmad M. Influence of iron restriction on Chlamydia pneumoniae and C. trachomatis. J Med Microbiol. 2001;50(3):223–7.
62. Goldoni P, Visca P, Pastoris MC, Valenti P, Orsi N. Growth of Legionella spp. under conditions of iron restriction. J Med Microbiol. 1991;34(2):113–8.

63. Zeng MY, Inohara N, Nuñez G. Mechanisms of inflammation-driven bacterial dysbiosis in the gut. Mucosal Immunol. 2017;10(1):18–26.
64. Cornelis P, Dingemans J. *Pseudomonas aeruginosa* adapts its iron uptake strategies in function of the type of infections. Front Cell Infect Microbiol. 2013;3(November):75.
65. Ghysels B, Ochsner U, Möllman U, Heinisch L, Vasil M, Cornelis P, et al. The *Pseudomonas aeruginosa* pir A gene encodes a second receptor for ferrienterobactin and synthetic catecholate analogues. FEMS Microbiol Lett. 2005 May 15;246(2):167–74.
66. Paauw A, Leverstein-van Hall MA, van Kessel KPM, Verhoef J, Fluit AC. Yersiniabactin reduces the respiratory oxidative stress response of innate immune cells. PLoS One. 2009;4(12):8240.
67. Mickelsen PA, Blackman E, Sparling PF. Ability of *Neisseria gonorrhoeae*, *Neisseria meningitidis*, and commensal *Neisseria* species to obtain iron from lactoferrin. Infect Immun. 1982;35(3):915–20.
68. Perkins-Balding D, Ratliff-Griffin M, Stojiljkovic I. Iron Transport Systems in Neisseria meningitidis. Microbiol Mol Biol Rev. 2004 Mar 1;68(1):154–71.
69. Singer M, Deutschman CS, Seymour C, Shankar-Hari M, Annane D, Bauer M, et al. The third international consensus definitions for sepsis and septic shock (sepsis-3). JAMA - J Am Med Assoc. 2016 Feb 23;315(8):801–10.
70. Rudd KE, Johnson SC, Agesa KM, Shackelford KA, Tsoi D, Kievlan DR, et al. Global, regional, and national sepsis incidence and mortality, 1990–2017: analysis for the Global Burden of Disease Study. Lancet. 2020;395(10219):200–11.
71. Rhee C, Jones TM, Hamad Y, Pande A, Varon J, O'Brien C, et al. Prevalence, underlying causes, and preventability of sepsis-associated mortality in US acute care hospitals. JAMA Netw open. 2019 Feb 1;2(2):e187571.
72. Torio CM, Moore BJ. National Inpatient Hospital Costs: The Most Expensive Conditions by Payer, 2013: Statistical Brief #204. Healthcare Cost and Utilization Project (HCUP) Statistical Briefs. Agency for Healthcare Research and Quality (US); 2006.

73. Gotts JE, Matthay MA. Sepsis: Pathophysiology and clinical management. BMJ. 2016 May 23;353:i1585.
74. Sinapidis D, Kosmas V, Vittoros V, Koutelidakis IM, Pantazi A, Stefos A, et al. Progression into sepsis: An individualized process varying by the interaction of comorbidities with the underlying infection. BMC Infect Dis. 2018;18(1):242.
75. Whiles B, Deis A, Miller P, Simpson S. Comorbid Conditions Predict Outcomes in Patients With Severe Sepsis. Chest. 2016;149(4):A170.
76. Caraballo C, Ascuntar J, Hincapié C, Restrepo C, Bernal E, Jaimes F. Association between site of infection and in-hospital mortality in patients with sepsis admitted to emergency departments of tertiary hospitals in Medellin, Colombia. Rev Bras Ter Intensiva. 2019;31(1):47–56.
77. Abe T, Ogura H, Kushimoto S, Shiraishi A, Sugiyama T, Deshpande GA, et al. Variations in infection sites and mortality rates among patients in intensive care units with severe sepsis and septic shock in Japan. J Intensive Care. 2019 Dec 3;7(1):28.
78. Wang Y, Wang D, Fu J, Liu Y. Predictive value of SOFA, qSOFA score and traditional evaluation index on sepsis prognosis. Zhonghua Wei Zhong Bing Ji Jiu Yi Xue. 2017 Aug 1;29(8):700–4.
79. Jentzer JC, Bennett C, Wiley BM, Murphree DH, Keegan MT, Gajic O, et al. Predictive value of the sequential organ failure assessment score for mortality in a contemporary cardiac intensive care unit population. J Am Heart Assoc. 2018;7(6): e008169.
80. Schulte W, Bernhagen J, Bucala R. Cytokines in sepsis: Potent immunoregulators and potential therapeutic targets - An updated view. Mediators Inflamm. 2013;2013:16.
81. Kunsch C, Medford RM. Oxidative stress as a regulator of gene expression in the vasculature. Circ Res. 1999 Oct 15;85(8):753–66.
82. Esmon CT. The interactions between inflammation and coagulation. Br J Haematol. 2005 Nov;131(4):417–30.
83. Assinger A, Schrottmaier WC, Salzmann M, Rayes J. Platelets in sepsis: An update on experimental models and clinical data. Front Immunol. 2019 Jul 17;10(JULY):1687.

84. Pawlinski R, Mackman N. Cellular sources of tissue factor in endotoxemia and sepsis. Thromb Res. 2010 Apr;125 Suppl 1:S70-3.
85. Gyawali B, Ramakrishna K, Dhamoon AS. Sepsis: The evolution in definition, pathophysiology, and management. SAGE Open Med. 2019;72050312119835043.
86. Semeraro F, Colucci M, Caironi P, Masson S, Ammollo CT, Teli R, et al. Platelet drop and fibrinolytic shutdown in patients with sepsis. Crit Care Med. 2018 Mar;46(3):E221–8.
87. Abraham E. Nuclear factor–κB and its role in sepsis-associated organ failure. J Infect Dis. 2003;187(s2):S364–9.
88. Xie QW, Kashiwabara Y, Nathan C. Role of transcription factor NF-κB/Rel in induction of nitric oxide synthase. J Biol Chem. 1994;269(7):4705–8.
89. Rubio-Gayosso I, Platts SH, Duling BR. Reactive oxygen species mediate modification of glycocalyx during ischemia-reperfusion injury Reactive oxygen species mediate modification of glycocalyx dur-ing ischemia-reperfusion injury. Am J Physiol Hear Circ Physiol. 2006;290:2247–56.
90. Auriemma CL, Zhuo H, Delucchi K, Deiss T, Liu T, Jauregui A, et al. Acute respiratory distress syndrome-attributable mortality in critically ill patients with sepsis. Intensive Care Med. 2020;46(6): 1222–1231.
91. Gattinoni L, Brazzi L, Pelosi P, Latini R, Tognoni G, Pesenti A, et al. A trial of goal-oriented hemodynamic therapy in critically ill patients. N Engl J Med. 1995 Oct 19;333(16):1025–32.
92. Xiang F, Wang J. Role of mitochondrial dysfunction in the pathogenesis of septic cardiomyopathy. Zhonghua Wei Zhong Bing Ji Jiu Yi Xue. 2018 Feb 1;30(2):189–92.
93. Fink MP. Cytopathic hypoxia and sepsis: Is mitochondrial dysfunction pathophysiologically important or just an epiphenomenon. Pediatr Crit Care Med. 2015 Jan 21;16(1):89–91.
94. Mantzarlis K, Tsolaki V, Zakynthinos E. Role of oxidative stress and mitochondrial dysfunction in sepsis and potential therapies. Oxid Med Cell Longev. 2017;5985209.

95. Crouser ED. Mitochondrial dysfunction in septic shock and multiple organ dysfunction syndrome. Mitochondrion. 2004;4(5–6):729–41.
96. Segal AW, Coade SB. Kinetics of oxygen consumption by phagocytosing human neutrophils. Biochem Biophys Res Commun. 1978 Oct 16;84(3):611–7.
97. Radi R. Oxygen radicals, nitric oxide, and peroxynitrite: Redox pathways in molecular medicine. Proc Natl Acad Sci U S A. 2018 Jun 5;115(23):5839–48.
98. Brealey D, Brand M, Hargreaves I, Heales S, Land J, Smolenski R, et al. Association between mitochondrial dysfunction and severity and outcome of septic shock. Lancet. 2002;360(9328):219–23.
99. Chuang CC, Shiesh SC, Chi CH, Tu YF, Hor LI, Shieh CC, et al. Serum total antioxidant capacity reflects severity of illness in patients with severe sepsis. Crit Care. 2006 Feb 20;10(1):R36.
100. De Backer D, Creteur J, Preiser J-C, Dubois M-J, Vincent J-L. Microvascular blood flow is altered in patients with sepsis. Am J Respir Crit Care Med. 2002 Jul 1;166(1):98–104.
101. Spronk PE, Zandstra DF, Ince C. Bench-to-bedside review: sepsis is a disease of the microcirculation. Crit Care. 2004 Dec;8(6):462–8.
102. Hotchkiss RS, Tinsley KW, Swanson PE, Schmieg RE, Hui JJ, Chang KC, et al. Sepsis-Induced apoptosis causes progressive profound depletion of B and CD4 + T lymphocytes in humans. J Immunol. 2001;166(11):6952–63.
103. Borrelli E, Roux-Lombard P, Grau GE, Girardin E, Ricou B, Dayer JM, et al. Plasma concentrations of cytokines, their soluble receptors, and antioxidant vitamins can predict the development of multiple organ failure in patients at risk. Crit Care Med. 1996;24(3):392–7.
104. Khan FA, Fisher MA, Khakoo RA. Association of hemochromatosis with infectious diseases: expanding spectrum. Int J Infect Dis. 2007;11(6):482–7.
105. Belotti A, Duca L, Borin L, Realini S, Renso R, Parma M, et al. Non transferrin bound iron (NTBI) in acute leukemias throughout conventional intensive chemotherapy: Kinetics of its appearance and potential predictive role in infectious complications. Leuk Res. 2015;39:88–91.

106. Tacke F, Nuraldeen R, Koch A, Strathmann K, Hutschenreuter G, Trautwein C, et al. Iron parameters determine the prognosis of critically ill patients. Crit Care Med. 2016 Jun 1;44(6):1049–58.
107. Lan P, Pan K han, Wang S jia, Shi Q cheng, Yu Y xian, Fu Y, et al. High serum iron level is associated with increased mortality in patients with sepsis. Sci Rep. 2018;8(11072).
108. Wizorek JJ, Turnbull IR, Buchman TG. Iron overload before cecal ligation and puncture increases mortality. Shock. 2003;20(1):52–5.
109. Patteril M V, Davey-Quinn AP, Gedney JA, Murdoch SD, Bellamy MC. Functional iron deficiency, infection and systemic inflammatory response syndrome in critical illness. Anaesth Intensive Care. 2001;29(5):473–8.
110. Takeda K, Shimada Y, Amano M, Sakai T, Okada T, Yoshiya I. Plasma lipid peroxides and alpha-tocopherol in critically ill patients. Crit Care Med. 1984;12(11):957–9.
111. Goode HF, Cowley HC, Walker BE, Howdle PD, Webster NR. Decreased antioxidant status and increased lipid peroxidation in patients with septic shock and secondary organ dysfunction. Crit Care Med. 1995;23(4):646–51.
112. Cowley HC, Bacon PJ, Goode HF, Webster NR, Jones JG, Menon DK. Plasma antioxidant potential in severe sepsis: A comparison of survivors and nonsurvivors. Crit Care Med. 1996 Jul;24(7):1179–83.
113. Karapetsa M, Pitsika M, Goutzourelas N, Stagos D, Tousia Becker A, Zakynthinos E. Oxidative status in ICU patients with septic shock. Food Chem Toxicol. 2013 Nov;61:106–11.
114. Borrelli E, Roux-Lombard P, Grau GE, Girardin E, Ricou B, Dayer JM, et al. Plasma concentrations of cytokines, their soluble receptors, and antioxidant vitamins can predict the development of multiple organ failure in patients at risk. Crit Care Med. 1996;24(3):392–7.
115. Lowes DA, Webster NR, Murphy MP, Galley HF. Antioxidants that protect mitochondria reduce interleukin-6 and oxidative stress, improve mitochondrial function, and reduce biochemical markers of organ dysfunction in a rat model of acute sepsis. Br J Anaesth. 2013;110(3):472–80.

116. Levy MM, Evans LE, Rhodes A. The surviving sepsis campaign bundle: 2018 update. Intensive Care Med. 2018;44(6):925–8.
117. Park SK, Shin SR, Hur M, Kim WH, Oh EA, Lee SH. The effect of early goal-directed therapy for treatment of severe sepsis or septic shock: A systemic review and meta-analysis. J Crit Care. 2017;38:115–22.
118. Rivers E, Nguyen B, Havstad S, Ressler J, Muzzin A, Knoblich B, et al. Early goal-directed therapy in the treatment of severe sepsis and septic shock. N Engl J Med. 2001;345(19):1368–77.
119. Guillon A, Preau S, Aboab J, Azabou E, Jung B, Silva S, et al. Preclinical septic shock research: why we need an animal ICU. Ann Intensive Care. 2019;9(1):66.
120. Dickson K, Lehmann C. Inflammatory response to different toxins in experimental sepsis models. Int J Mol Sci. 2019;20(18):4341.
121. Murakami E, Shionoya T, Komenoi S, Suzuki Y, Sakane F. Cloning and characterization of novel testis-specific diacylglycerol kinase η splice variants 3 and 4. PLoS One. 2014;11(9).
122. Schabbauer G. Polymicrobial sepsis models: CLP versus CASP. Drug Discov Today Dis Model. 2012 Mar 1;9(1):e17–21.
123. Knapp S, Schultz MJ, Van Der Poll T. Pneumonia models and innate immunity to respiratory bacterial pathogens. Shock. 2005 Dec;24:12–8.
124. Coopersmith CM, Stromberg PE, Michael Dunne W, Davis CG, Amiot DM, Buchman TG, et al. Inhibition of intestinal epithelial apoptosis and survival in a murine model of pneumonia-induced sepsis. J Am Med Assoc. 2002 Apr 3;287(13):1716–21.
125. Svensson M, Yadav M, Holmqvist B, Lutay N, SVanborg C, Godaly G. Acute pyelonephritis and renal scarring are caused by dysfunctional innate immunity in mCxcr2 heterozygous mice. Kidney Int. 2011;80(10):1064–72.
126. Muenzer JT, Davis CG, Dunne BS, Unsinger J, Dunne WM, Hotchkiss RS. Pneumonia after cecal ligation and puncture: A clinically relevant “two-hit” model of sepsis. Shock. 2006 Dec;26(6):565–70.

127. Zingarelli B, Coopersmith CM, Drechsler S, Efron P, Marshall JC, Moldawer L, et al. Part I: Minimum Quality Threshold in Preclinical Sepsis Studies (MQTiPSS) for Study Design and Humane Modeling Endpoints. Shock. 2019;51(1):10–22.
128. Libert C, Ayala A, Bauer M, Cavaillon JM, Deutschman C, Frostell C, et al. Part II: Minimum Quality Threshold in Preclinical Sepsis Studies (MQTiPSS) for Types of Infections and Organ Dysfunction Endpoints. Vol. 51, Shock. 2019. p. 23–32.
129. Hellman J, Bahrami S, Boros M, Chaudry IH, Fritsch G, Gozdzik W, et al. Part III: Minimum Quality Threshold in Preclinical Sepsis Studies (MQTiPSS) for Fluid Resuscitation and Antimicrobial Therapy Endpoints. Shock. 2019 Jan 1;51(1):33–43.
130. Cystic Fibrosis Canada. The Canadian Cystic Fibrosis Registry: 2018 Annual data report. 2018.
131. Veit G, Avramescu RG, Chiang AN, Houck SA, Cai Z, Peters KW, et al. From CFTR biology toward combinatorial pharmacotherapy: Expanded classification of cystic fibrosis mutations. Mol Biol Cell. 2016;27(3):424–33.
132. Sabharwal S. Gastrointestinal manifestations of cystic fibrosis. Gastroenterol Hepatol. 2016;12(1):43–7.
133. Kayani K, Mohammed R, Mohiaddin H. Cystic fibrosis-related diabetes. Front Endocrinol (Lausanne). 2018;9(20).
134. Turcios NL. Cystic Fibrosis Lung Disease: An Overview. Respir Care. 2020 Feb 1;65(2):233–51.
135. Moore PJ, Tarran R. The epithelial sodium channel (ENaC) as a therapeutic target for cystic fibrosis lung disease. Expert Opin Ther Targets. 2018 Aug 3;22(8):687–701.
136. Balázs A, Mall MA. Mucus obstruction and inflammation in early cystic fibrosis lung disease: Emerging role of the IL-1 signaling pathway. Pediatr Pulmonol. 2019 Nov 12;54(S3):S5–12.
137. Carrabino S, Carpani D, Livraghi A, Di Cicco M, Costantini D, Copreni E, et al. Dysregulated interleukin-8 secretion and NF-κB activity in human cystic fibrosis nasal epithelial cells. J Cyst Fibros. 2006 May 1;5(2):113–9.

138. Bérubé J, Roussel L, Nattagh L, Rousseau S. Loss of cystic fibrosis transmembrane conductance regulator function enhances activation of p38 and erk mapks, increasing interleukin-6 synthesis in airway epithelial cells exposed to *Pseudomonas aeruginosa*. J Biol Chem. 2010;285(29):22299–307.
139. Bonfield TL, Konstan MW, Berger M. Altered respiratory epithelial cell cytokine production in cystic fibrosis. J Allergy Clin Immunol. 1999;104(1):72–8.
140. Nguyen GT, Green ER, Mecsas J. Neutrophils to the ROScue: Mechanisms of NADPH oxidase activation and bacterial resistance. Front Cell Infect Microbiol. 2017;7:373.
141. Morris MR, Doull IJM, Dewitt S, Hallett MB. Reduced iC3b-mediated phagocytotic capacity of pulmonary neutrophils in cystic fibrosis. Clin Exp Immunol. 2005;142(1):68–75.
142. Sly PD, Brennan S, Gangell C, De Klerk N, Murray C, Mott L, et al. Lung disease at diagnosis in infants with cystic fibrosis detected by newborn screening. Am J Respir Crit Care Med. 2009;180(2):146–52.
143. Khan MA, Ali ZS, Sweezey N, Grasemann H, Palaniyar N. Progression of cystic fibrosis lung disease from childhood to adulthood: Neutrophils, neutrophil extracellular trap (NET) formation, and NET degradation. Genes (Basel). 2019;10(183).
144. Sly PD, Gangell CL, Chen L, Ware RS, Ranganathan S, Mott LS, et al. Risk factors for bronchiectasis in children with cystic fibrosis. N Engl J Med. 2013;368(21):1963–70.
145. Tate S, MacGregor G, Davis M, Innes JA, Greening AP. Airways in cystic fibrosis are acidified: Detection by exhaled breath condensate. Thorax. 2002;57(11):926–9.
146. Kim CS, Ahmad S, Wu T, Walton WG, Redinbo MR, Tarran R. SPLUNC1 is an allosteric modulator of the epithelial sodium channel. FASEB J. 2018 May 1;32(5):2478–91.
147. Peter Di Y. Functional roles of SPLUNC1 in the innate immune response against Gram-negative bacteria. In: Biochemical Society Transactions. 2011. p. 1051–5.

148. Walton WG, Ahmad S, Little MS, Kim CSK, Tyrrell J, Lin Q, et al. Structural Features Essential to the Antimicrobial Functions of Human SPLUNC1. Biochemistry. 2016;55(21):2979–91.
149. Gakhar L, Bartlett JA, Penterman J, Mizrachi D, Singh PK, Mallampalli RK, et al. PLUNC is a novel airway surfactant protein with anti-biofilm activity. PLoS One. 2010;5(2):e9098.
150. Ahmad S, Gilmore RC, Alexis NE, Tarran R. SPLUNC1 loses its antimicrobial activity in acidic cystic fibrosis airway secretions. Am J Respir Crit Care Med. 2019 Sep 1;200(5):633–6.
151. Alaiwa MHA, Reznikov LR, Gansemer ND, Sheets KA, Horswill AR, Stoltz DA, et al. pH modulates the activity and synergism of the airway surface liquid antimicrobials β-defensin-3 and LL-37. Proc Natl Acad Sci U S A. 2014 Dec 30;111(52):18703–8.
152. Cantin AM, Hartl D, Konstan MW, Chmiel JF. Inflammation in cystic fibrosis lung disease: Pathogenesis and therapy. J Cyst Fibros. 2015;14(4):419–30.
153. John G, Yildirim AÖ, Rubin BK, Gruenert DC, Henke MO. TLR-4-mediated innate immunity is reduced in cystic fibrosis airway cells. Am J Respir Cell Mol Biol. 2010 Apr;42(4):424–31.
154. Yang HZ, Wang JP, Mi S, Liu HZ, Cui B, Yan HM, et al. TLR4 activity is required in the resolution of pulmonary inflammation and fibrosis after acute and chronic lung injury. Am J Pathol. 2012 Jan 1;180(1):275–92.
155. John G, Yildirim AÖ, Rubin BK, Gruenert DC, Henke MO. TLR-4-mediated innate immunity is reduced in cystic fibrosis airway cells. Am J Respir Cell Mol Biol. 2010;42(4):424–31.
156. John G, Chillappagari S, Rubin BK, Gruenert DC, Henke MO. Reduced surface toll-like receptor-4 expression and absent interferon-γinducible protein-10 induction in cystic fibrosis airway cells. Exp Lung Res. 2011;37(6):319–26.
157. Vencken SF, Greene CM. Toll-Like Receptors in Cystic Fibrosis: Impact of Dysfunctional microRNA on Innate Immune Responses in the Cystic Fibrosis Lung. J Innate Immun. 2016;8(6):541–9.

158. Vandeplassche E, Tavernier S, Coenye T, Crabbé A. Influence of the lung microbiome on antibiotic susceptibility of cystic fibrosis pathogens. Eur Respir Rev. 2019 Jun 30;28(152).
159. Learn DB, Brestel EP, Seetharama S. Hypochlorite scavenging by *Pseudomonas aeruginosa* alginate. Infect Immun. 1987;55(8):1813–8.
160. Mets OM, Roothaan SM, Bronsveld I, Luijk B, Van De Graaf EA, Vink A, et al. Emphysema is common in lungs of cystic fibrosis lung transplantation patients: A histopathological and computed tomography study. Vij N, editor. PLoS One. 2015 Jun 5;10(6):e0128062.
161. Wielpütz MO, Weinheimer O, Eichinger M, Wiebel M, Biederer J, Kauczor HU, et al. Pulmonary emphysema in cystic fibrosis detected by densitometry on chest multidetector computed tomography. PLoS One. 2013;8(8):e73142.
162. van der Vliet A. NADPH oxidases in lung biology and pathology: Host defense enzymes, and more. Free Radic Biol Med. 2008;44(6):938–55.
163. Conese M, Copreni E, Gioia S Di, Rinaldis P De, Fumarulo R. Neutrophil recruitment and airway epithelial cell involvement in chronic cystic fibrosis lung disease. J Cyst Fibros. 2003 Sep;2(3):129–35.
164. Ghio AJ, Roggli VL, Soukup JM, Richards JH, Randell SH, Muhlebach MS. Iron accumulates in the lavage and explanted lungs of cystic fibrosis patients. J Cyst Fibros. 2013 Jul;12(4):390–8.
165. Moreau-Marquis S, Bomberger JM, Anderson GG, Swiatecka-Urban A, Ye S, O'Toole GA, et al. The DeltaF508-CFTR mutation results in increased biofilm formation by *Pseudomonas aeruginosa* by increasing iron availability. Am J Physiol Lung Cell Mol Physiol. 2008 Jul;295(1):L25-37.
166. Ridley K, Condren M. Elexacaftor-Tezacaftor-Ivacaftor: The First Triple-Combination Cystic Fibrosis Transmembrane Conductance Regulator Modulating Therapy. J Pediatr Pharmacol Ther. 2020;25(3):192–7.
167. Chmiel JF, Konstan MW, Elborn JS. Antibiotic and anti-inflammatory therapies for cystic fibrosis. Cold Spring Harb Perspect Med. 2013;3(10):a009779.

168. Neufeld EJ. Oral chelators deferasirox and deferiprone for transfusional iron overload in thalassemia major: New data, new questions. Blood. 2006 May 1;107(9):3436–41.
169. Jordan LB, Vekeman F, Sengupta A, Corral M, Guo A, Duh MS. Persistence and compliance of deferoxamine versus deferasirox in Medicaid patients with sickle-cell disease. J Clin Pharm Ther. 2012 Apr;37(2):173–81.
170. QuarterWatch: 2009 Quarter 4 Monitoring MedWatch Reports Executive Summary. 2010. https://www.ismp.org/sites/default/files/attachments/2018-01/2009Q4.pdf
171. The Danish Medicines Agency's "Prevention of Medication Errors" Network. Medicines most frequently involved in serious adverse drug events. 2011. https://laegemiddelstyrelsen.dk/en/publications/2011/publication-on-medicines-most-frequently-involved-in-serious-adverse-drug events/~/media/D351DCAA2DB4463498724643F4E876C6.ashx
172. Desferal ® deferoxamine mesylate for injection USP Vials Rx only Prescribing Information. Novartis. https://www.accessdata.fda.gov/drugsatfda_docs/label/2007/016267s044lbl.pdf
173. Molitoris BA, Alfrey PS, Miller NL, Hasbargen JA, Kaehney WD, Smith BJ. Efficacy of intramuscular and intraperitoneal deferoxamine for aluminium chelation. Kidney Int. 1987 Apr 1;31(4):986–91.
174. Di Nicola M, Barteselli G, Dell'Arti L, Ratiglia R, Viola F. Functional and structural abnormalities in deferoxamine retinopathy: A review of the literature. Biomed Res Int. 2015;2015:249617.
175. Olivieri NF, Brittenham GM, Mclaren CE, Templeton DM, Cameron RG, Mcclelland RA, et al. Long-term safety and effectiveness of iron-chelation therapy with deferiprone for thalassemia major. N Engl J Med. 1998;339(7):417–23.
176. Tricta F, Uetrecht J, Galanello R, Connelly J, Rozova A, Spino M, et al. Deferiprone-induced agranulocytosis: 20 years of clinical observations. Am J Hematol. 2016 Oct 1;91(10):1026–31.
177. Kattamis A. Combined therapy with deferoxamine and deferiprone. In: Annals of the New York Academy of Sciences. New York Academy of Sciences; 2005. p. 175–82.

178. Parquet M del C, Savage KA, Allan DS, C Ang MT, Chen W, Logan SM, et al. Antibiotic-resistant *acinetobacter baumannii* Is susceptible to the novel iron-sequestering anti-infective DIBI in vitro and in experimental pneumonia in mice. Antimicrob Agents Chemother. 2019;63(9).
179. Prus E, Fibach E. The labile iron pool in human erythroid cells. Br J Haematol. 2008 Jul;142(2):301–7.
180. Cozens AL, Yezzi MJ, Chin L, Simon EM, Finkbeiner WE, Wagner JA, et al. Characterization of Immortal Cystic Fibrosis Tracheobronchial Gland Epithelial Cells. Source Proc Natl Acad Sci United States Am Med Sci. 1992;89(89):5171–5.
181. Chappe F, Loewen ME, Hanrahan JW, Chappe V. Vasoactive intestinal peptide increases cystic fibrosis transmembrane conductance regulator levels in the apical membrane of Calu-3 cells through a protein kinase C-dependent mechanism. J Pharmacol Exp Ther. 2008 Oct;327(1):226–38.
182. Poroca DR, Amer N, Li A, Hanrahan JW, Chappe VM. Changes in the R-region interactions depend on phosphorylation and contribute to PKA and PKC regulation of the cystic fibrosis transmembrane conductance regulator chloride channel. FASEB BioAdvances. 2020 Jan 24;2(1):33–48.
183. Shrum B, Anantha R V., Xu SX, Donnelly M, Haeryfar SMM, McCormick JK, et al. A robust scoring system to evaluate sepsis severity in an animal model. BMC Res Notes. 2014 Apr 12;7(1):233.
184. Chiu CJ, Scott HJ, Gurd FN. II. The Protective Effect of Intraluminal Glucose as Energy Substrate. Arch Surg. 1970;101(4):484–8.
185. Comeau AM, Douglas GM, Langille MGI. Microbiome Helper: a Custom and Streamlined Workflow for Microbiome Research. Am Soc Microbiol. 2017;2(1).
186. Thorburn TV. Iron-related immune cell function in sepsis. Dalhousie University; 2018.
187. Liu J, Li X, Yue Y, Li J, He T, He Y. The inhibitory effect of quercetin on IL-6 production by LPS-stimulated neutrophils. Cell Mol Immunol. 2005 Dec 1;2(6):455–60.

188. Aida Y, Pabst MJ. Priming of neutrophils by lipopolysaccharide for enhanced release of superoxide: Requirement for plasma but not for tumor necrosis factor-α. J Immunol. 1990;145(9):3017–25.
189. Gomes NE, Brunialti MKC, Mendes ME, Freudenberg M, Galanos C, Salomão R. Lipopolysaccharide-induced expression of cell surface receptors and cell activation of neutrophils and monocytes in whole human blood. Brazilian J Med Biol Res. 2010;43(9):853–9.
190. Narazaki M, Kishimoto T. The two-faced cytokine IL-6 in host defense and diseases. Int J Mol Sci. 2018;19(11).
191. Islam S, Jarosch S, Zhou J, Parquet MDC, Toguri JT, Colp P, et al. Anti-inflammatory and anti-bacterial effects of iron chelation in experimental sepsis. J Surg Res. 2015;200(1):266–73.
192. Venkatakrishnan A, Stecenko AA, King G, Blackwell TR, Brigham KL, Christman JW, et al. Exaggerated activation of nuclear factor-κB and altered IκB-β processing in cystic fibrosis bronchial epithelial cells. Am J Respir Cell Mol Biol. 2000;23(3):396–403.
193. Weber AJ, Soong G, Bryan R, Saba S, Prince A. Activation of NF-κB in airway epithelial cells is dependent on CFTR trafficking and Cl- channel function. Am J Physiol - Lung Cell Mol Physiol. 2001;281(1 25-1).
194. DiMango E, Ratner AJ, Bryan R, Tabibi S, Prince A. Activation of NF-κB by adherent *Pseudomonas aeruginosa* in normal and cystic fibrosis respiratory epithelial cells. J Clin Invest. 1998;101(11):2598–606.
195. Giridharan S, Srinivasan M. Mechanisms of NF-κB p65 and strategies for therapeutic manipulation. J Inflamm Res. 2018;11:407–19.
196. Greenshields AL, Power Coombs MR, Fernando W, Holbein BE, Hoskin DW. DIBI, a novel 3-hydroxypyridin-4-one chelator iron-binding polymer, inhibits breast cancer cell growth and functions as a chemosensitizer by promoting S-phase DNA damage. BioMetals. 2019;32(6):909–21.
197. Kurz T, Eaton JW, Brunk UT. The role of lysosomes in iron metabolism and recycling. Int J Biochem Cell Biol. 2011;43:1686–97.

198. Yu Z, Persson HL, Eaton JW, Brunk UT. Intralysosomal iron: A major determinant of oxidant-induced cell death. Free Radic Biol Med. 2003;34(10):1243–52.
199. Kurz T, Gustafsson B, Brunk UT. Intralysosomal iron chelation protects against oxidative stress-induced cellular damage. FEBS J. 2006 Jul;273(13):3106–17.
200. Tenopoulou M, Kurz T, Doulias PT, Galaris D, Brunk UT. Does the calcein-AM method assay the total cellular "labile iron pool" or only a fraction of it? Biochem J. 2007;403(2):261–6.
201. Saha P, Yeoh BS, Olvera RA, Xiao X, Singh V, Awasthi D, et al. Bacterial Siderophores Hijack Neutrophil Functions. J Immunol. 2017;198(11):4293–303.
202. Williams AE, Chambers RC. The mercurial nature of neutrophils: still an enigma in ARDS? AJP Lung Cell Mol Physiol. 2014;306(3):L217–30.
203. Mittal R, Coopersmith CM. Redefining the gut as the motor of critical illness. Trends Mol Med. 2014;20(4):214–23.
204. Fokam D, Dickson K, Kamali K, Holbein B, Colp P, Stueck A, et al. Iron chelation in murine models of systemic inflammation induced by gram-positive and gram-negative toxins. Antibiotics. 2020 May 26;9(6):283.
205. Arora N, Islam S, Wafa K, Zhou J, Toguri JT, Cerny V, et al. Evaluation of iris functional capillary density in experimental local and systemic inflammation. J Microsc. 2017 Apr;266(1):55–9.
206. Lehmann C, Islam S, Jarosch S, Zhou J, Hoskin D, Greenshields A, et al. The Utility of Iron Chelators in the Management of Inflammatory Disorders. Mediators Inflamm. 2015;2015:1–12.
207. Brazil JC, Parkos CA. Pathobiology of neutrophil-epithelial interactions. Immunol Rev. 2016 Sep;273(1):94–111.
208. Thimmulappa RK, Lee H, Rangasamy T, Reddy SP, Yamamoto M, Kensler TW, et al. Nrf2 is a critical regulator of the innate immune response and survival during experimental sepsis . J Clin Invest. 2006;116(4).
209. Schieber M, Chandel NS. ROS function in redox signaling and oxidative stress. Curr Biol. 2014 May 19;24(10):R453–62.

210. Cermanova J, Kadova Z, Dolezelova E, Zagorova M, Safka V, Hroch M, et al. Deferoxamine but not dexrazoxane alleviates liver injury induced by endotoxemia in rats. Shock. 2014;42(4):372–9.
211. Heli H, Mirtorabi S, Karimian K. Advances in iron chelation: An update. Expert Opin Ther Pat. 2011 Jun;21(6):819–56.
212. Ang MTC, Gumbau-Brisa R, Allan DS, McDonald R, Ferguson MJ, Holbein BE, et al. DIBI, a 3-hydroxypyridin-4-one chelator iron-binding polymer with enhanced antimicrobial activity. Medchemcomm. 2018;9(7):1206–12.
213. Thorburn T, Aali M, Kostek L, LeTourneau-Paci C, Colp P, Zhou J, et al. Anti-inflammatory effects of a novel iron chelator, DIBI, in experimental sepsis. Jünger M, Krüger-Genge A, Jung F, editors. Clin Hemorheol Microcirc. 2017 Dec 9;67(3–4):241–50.
214. Arora N, Islam S, Wafa K, Zhou J, Toguri JT, Cerny V, et al. Evaluation of iris functional capillary density in experimental local and systemic inflammation. J Microsc. 2017 Apr;266(1):55–9.
215. Matharu NM, Butler LM, Rainger GE, Gosling P, Vohra RK, Nash GB. Mechanisms of the anti-inflammatory effects of hydroxyethyl starch demonstrated in a flow-based model of neutrophil recruitment by endothelial cells. Crit Care Med. 2008 May 1;36(5):1536–42.
216. Nohé B, Johannes T, Reutershan J, Rothmund A, Haeberle HA, Ploppa A, et al. Synthetic colloids attenuate leukocyte-endothelial interactions by inhibition of integrin function. Anesthesiology. 2005;103(4):759–67.
217. Handrigan MT, Burns AR, Donnachie EM, Bowden RA. Hydroxyethyl starch inhibits neutrophil adhesion and transendothelial migration. Shock. 2005 Nov;24(5):434–9.
218. Pascual JL, Ferri LE, Chaudhury P, Seely AJE, Campisi G, Giannias B, et al. Hemorrhagic shock resuscitation with a low molecular weight starch reduces neutrophil-endothelial interactions and vessel leakage in vivo. Surg Infect (Larchmt). 2001;2(4):275–88.

219. Miranda ML de, Balarini M de M, Caixeta DM da L, Bouskela E. Microcirculatory dysfunction in sepsis: pathophysiology, clinical monitoring, and potential therapies. Am J Physiol Heart Circ Physiol. 2016 Jul 1;311(1):H24–35.
220. Ince C. The microcirculation is the motor of sepsis. Crit Care. 2005;9 Suppl 4:S13-9.
221. Ince C. Hemodynamic coherence and the rationale for monitoring the microcirculation. Crit Care. 2015;19(Suppl 3):S8.
222. Verdant CL, De Backer D, Bruhn A, Clausi CM, Su F, Wang Z, et al. Evaluation of sublingual and gut mucosal microcirculation in sepsis: A quantitative analysis. Crit Care Med. 2009;37(11):2875–81.
223. Lima A, Van Rooij T, Ergin B, Sorelli M, Ince Y, Specht PAC, et al. Dynamic contrast-enhanced ultrasound identifies microcirculatory alterations in sepsis-induced acute kidney injury. Crit Care Med. 2018;46(8):1284–92.
224. Boerma EC, Van Der Voort PHJ, Spronk PE, Ince C. Relationship between sublingual and intestinal microcirculatory perfusion in patients with abdominal sepsis. Crit Care Med. 2007;35(4):1055–60.
225. Massey MJ, Hou PC, Filbin M, Wang H, Ngo L, Huang DT, et al. Microcirculatory perfusion disturbances in septic shock: Results from the ProCESS trial. Crit Care. 2018;22(1).
226. De Backer D, Creteur J, Dubois MJ, Sakr Y, Koch M, Verdant C, et al. The effects of dobutamine on microcirculatory alterations in patients with septic shock are independent of its systemic effects. Crit Care Med. 2006;34(2):403–8.
227. De Backer D, Creteur J, Preiser JC, Dubois MJ, Vincent JL. Microvascular blood flow is altered in patients with sepsis. Am J Respir Crit Care Med. 2002;166(1):98–104.
228. Lehmann C, Bac VH, Pavlovic D, Lustig M, Maier S, Feyerherd F, et al. Metronidazole improves intestinal microcirculation in septic rats independently of bacterial burden. Clin Hemorheol Microcirc. 2006;34(3):427–38.
229. Pinsky MR, Vincent JL, Deviere J, Alegre M, Kahn RJ, Dupont E. Serum cytokine levels in human septic shock; Relation to multiple-system organ failure and mortality. Chest. 1993;103(2):565–75.

230. Tang BM, Huang SJ, McLean AS. Genome-wide transcription profiling of human sepsis: A systematic review. Crit Care. 2010;14(6):R237.
231. Okusawa S, Gelfand JA, Ikejima T, Connolly RJ, Dinarello CA. Interleukin 1 induces a shock-like state in rabbits. Synergism with tumor necrosis factor and the effect of cyclooxygenase inhibition. J Clin Invest. 1988;81(4):1162–72.
232. Cohen J. The immunopathogenesis of sepsis. Nature. 2002;420(6917):885–91.
233. Parameswaran N, Patial S. Tumor necrosis factor-a signaling in macrophages. Crit Rev Eukaryot Gene Expr. 2010;20(2):87–103.
234. Mera S, Tatulescu D, Cismaru C, Bondor C, Slavcovici A, Zanc V, et al. Multiplex cytokine profiling in patients with sepsis. APMIS. 2011 Feb 1;119(2):155–63.
235. Leentjens J, Kox M, Koch RM, Preijers F, Joosten LAB, Van Der Hoeven JG, et al. Reversal of immunoparalysis in humans in vivo: A double-blind, placebo-controlled, randomized pilot study. Am J Respir Crit Care Med. 2012 Nov 1;186(9):838–45.
236. Romero CR, Herzig DS, Etogo A, Nunez J, Mahmoudizad R, Fang G, et al. The role of interferon-γ in the pathogenesis of acute intra-abdominal sepsis. J Leukoc Biol. 2010 Oct;88(4):725–35.
237. Hack CE, De Groot ER, Felt-Bersma RJF, Nuijens JH, Strack Van Schijndel RJM, Eerenberg-Belmer AJM, et al. Increased plasma levels of interleukin-6 in sepsis. Blood. 1989;74(5):1704–10.
238. Ritter C, Andrades ME, Reinke A, Menna-Barreto S, Moreira JCF, Dal-Pizzol F. Treatment with N-acetylcysteine plus deferoxamine protects rats against oxidative stress and improves survival in sepsis. Crit Care Med. 2004;32(2):342–9.
239. Waage A, Brandtzaeg P, Halstensen A, Kierulf P, Espevik T. The complex pattern of cytokines in serum from patients with meningococcal septic shock. Association between interleukin 6, interleukin 1, and fatal outcome. J Exp Med. 1989;169(1):333–8.
240. Gouel-Chéron A, Allaouchiche B, Guignant C, Davin F, Floccard B, Monneret G. Early interleukin-6 and slope of monocyte human leukocyte antigen-DR: A powerful association to predict the development of sepsis after major trauma. PLoS One. 2012;7(3):e33095.

241. Wu HP, Chen CK, Chung K, Tseng JC, Hua CC, Liu YC, et al. Serial cytokine levels in patients with severe sepsis. Inflamm Res. 2009;58(7):385–93.
242. Kumar A, Sudhir U, Punith K, Kumar R, Ravi Kumar V, Rao M. Cytokine profile in elderly patients with sepsis. Indian J Crit Care Med. 2009 Apr 1;13(2):74–8.
243. Gogos CA, Drosou E, Bassaris HP, Skoutelis A. Pro- versus Anti-inflammatory Cytokine Profile in Patients with Severe Sepsis: A Marker for Prognosis and Future Therapeutic Options. J Infect Dis. 2000 Jan;181(1):176–80.
244. Friedman G, Jankowski S, Marchant A, Goldman M, Kahn RJ, Vincent JL. Blood interleukin 10 levels parallel the severity of septic shock. J Crit Care. 1997;12(4):183–7.
245. Haak BW, Prescott HC, Wiersinga WJ. Therapeutic potential of the gut microbiota in the prevention and treatment of sepsis. Front Immunol. 2018;9(2042).
246. Assimakopoulos SF, Triantos C, Thomopoulos K, Fligou F, Maroulis I, Marangos M, et al. Gut-origin sepsis in the critically ill patient: pathophysiology and treatment. Infection. 2018;46(6):751–60.
247. Xie K, Xie H, Su G, Chen D, Yu B, Mao X, et al. β-Defensin 129 Attenuates Bacterial Endotoxin-Induced Inflammation and Intestinal Epithelial Cell Apoptosis. Front Immunol. 2019 Oct 4;10:2333.
248. Han X, Fink MP, Yang R, Delude RL. Increased iNOS activity is essential for intestinal epithelial tight junction dysfunction in endotoxemic mice. Shock. 2004 Mar;21(3):261–70.
249. Nighot M, Al-Sadi R, Guo S, Rawat M, Nighot P, Watterson MD, et al. Lipopolysaccharide-induced increase in intestinal epithelial tight permeability is mediated by toll-like receptor 4/myeloid differentiation primary response 88 (MyD88) activation of myosin light chain kinase expression. Am J Pathol. 2017;187(12):2698–710.
250. Zhang S, Zhou Q, Li Y, Zhang Y, Wu Y. MitoQ modulates lipopolysaccharide-induced intestinal barrier dysfunction via regulating Nrf2 signaling. Mediators Inflamm. 2020;2020:1–9.

251. Williams JM, Duckworth CA, Watson AJM, Frey MR, Miguel JC, Burkitt MD, et al. A mouse model of pathological small intestinal epithelial cell apoptosis and shedding induced by systemic administration of lipopolysaccharide. DMM Dis Model Mech. 2013 Nov 1;6(6):1388–99.
252. Zhang L, Wei X, Zhang R, Si D, Petitte JN, Ahmad B, et al. A novel peptide ameliorates LPS-induced intestinal inflammation and mucosal barrier damage via its antioxidant and antiendotoxin effects. Int J Mol Sci. 2019;20(3974).
253. Lewis AJ, Seymour CW, Rosengart MR. Current Murine Models of Sepsis. Surg Infect (Larchmt). 2016;17(4):385–93.
254. Lehmann C, Kianian M, Zhou J, Küster I, Kuschnereit R, Whynot S, et al. Cannabinoid receptor 2 activation reduces intestinal leukocyte recruitment and systemic inflammatory mediator release in acute experimental sepsis. Crit Care. 2012;16(2):R47.
255. Ritter C, Andrades ME, Reinke A, Menna-Barreto S, Moreira JCF, Dal-Pizzol F. Treatment with N-acetylcysteine plus deferoxamine protects rats against oxidative stress and improves survival in sepsis. Crit Care Med. 2004 Feb;32(2):342–9.
256. Messaris E, Antonakis PT, Memos N, Chatzigianni E, Leandros E, Konstadoulakis MM. Deferoxamine administration in septic animals: Improved survival and altered apoptotic gene expression. Int Immunopharmacol. 2004;4(3):455–9.
257. Traeger T, Koerner P, Kessler W, Cziupka K, Diedrich S, Busemann A, et al. Colon Ascendens Stent Peritonitis (CASP) - a standardized model for polymicrobial abdominal sepsis. J Vis Exp. 2010;46(46):2299.
258. Emmanuilidis K, Weighardt H, Maier S, Gerauer K, Fleischmann T, Zheng XX, et al. Critical role of kupffer cell-derived IL-10 for host defense in septic peritonitis. J Immunol. 2001;167(7):3919–27.
259. Jusek G, Reim D, Tsujikawa K, Holzmann B. Deficiency of the CGRP receptor component RAMP1 attenuates immunosuppression during the early phase of septic peritonitis. Immunobiology. 2012 Aug 1;217(8):761–7.
260. Hu Q, Ren H, Li G, Wang D, Zhou Q, Wu J, et al. STING-mediated intestinal barrier dysfunction contributes to lethal sepsis. EBioMedicine. 2019;41:497–508.

261. Holbein BE, Mira De Orduña R. Effect of trace iron levels and iron withdrawal by chelation on the growth of Candida albicans and Candida vini. FEMS Microbiol Lett. 2010;307(1):19–24.
262. Savage KA, del Carmen Parquet M, Allan DS, Davidson RJ, Holbein BE, Lilly EA, et al. Iron restriction to clinical isolates of candida albicans by the novel chelator dibi inhibits growth and increases sensitivity to azoles in vitro and in vivo in a murine model of experimental vaginitis. Antimicrob Agents Chemother. 2018;62(8):e02576-17.
263. Choi VM, Herrou J, Hecht AL, Teoh WP, Turner JR, Crosson S, et al. Activation of Bacteroides fragilis toxin by a novel bacterial protease contributes to anaerobic sepsis in mice. Nat Med. 2016;22(5):563–7.
264. Wexler HM. Bacteroides: the good, the bad, and the nitty-gritty. Vol. 20, Clinical Microbiology Reviews. 2007. p. 593–621.
265. Rocha ER, Bergonia HA, Gerdes S, Jeffrey Smith C. Bacteroides fragilis requires the ferrous-iron transporter FeoAB and the CobN-like proteins BtuS1 and BtuS2 for assimilation of iron released from heme. Microbiologyopen. 2019;8(4):669.
266. Mayr FB, Yende S, Angus DC. Epidemiology of severe sepsis. Virulence. 2014;5(1):4–11.
267. Santajit S, Indrawattana N. Mechanisms of Antimicrobial Resistance in ESKAPE Pathogens. Biomed Res Int. 2016.
268. Lesic B, Foulon J, Carniel E. Comparison of the effects of deferiprone versus deferoxamine on growth and virulence of Yersinia enterocolitica. Antimicrob Agents Chemother. 2002;46(6):1741–5.
269. Monegro AF, Regunath H. Hospital Acquired Infections. 2020 Jan; https://www.ncbi.nlm.nih.gov/books/NBK441857/
270. Peng Z, Jin D, Kim HB, Stratton CW, Wu B, Tang YW, et al. Update on antimicrobial resistance in Clostridium difficile: Resistance mechanisms and antimicrobial susceptibility testing. J Clin Microbiol. 2017;55(7):1998–2008.
271. Hirabayashi K, Shiohara M, Suzuki T, Saito S, Tanaka M, Yanagisawa R, et al. Critical illness polyneuropathy and myopathy caused by bacillus cereus sepsis in acute lymphoblastic leukemia. J Pediatr Hematol Oncol. 2012 Apr;34(3):e110-3.

272. Luyt CE, Hékimian G, Koulenti D, Chastre J. Microbial cause of ICU-acquired pneumonia: Hospital-acquired pneumonia versus ventilator-associated pneumonia. Curr Opin Crit Care. 2018;24(5):333–8.
273. Humphreys H, Becker K, Dohmen PM, Petrosillo N, Spencer M, van Rijen M, et al. Staphylococcus aureus and surgical site infections: benefits of screening and decolonization before surgery. J Hosp Infect. 2016 Nov 1;94(3):295–304.
274. Magill SS, Edwards JR, Bamberg W, Beldavs ZG, Dumyati G, Kainer MA, et al. Multistate point-prevalence survey of health care-associated infections. N Engl J Med. 2014;370(13):1198–208.
275. Allan DS, Del Carmen Parquet M, Savage KA, Holbein BE. Iron sequestrant DIBI, a potential alternative for nares decolonization of methicillin-resistant Staphylococcus aureus, is anti-infective and inhibitory for mupirocin-resistant isolates. Antimicrob Agents Chemother. 2020;64(3):e02353-19.
276. Parquet M del C, Savage KA, Allan DS, Davidson RJ, Holbein BE. Novel iron-chelator DIBI inhibits Staphylococcus aureus growth, suppresses experimental MRSA infection in mice and enhances the activities of diverse antibiotics in vitro. Front Microbiol. 2018;9.
277. Gentile LF, Nacionales DC, Lopez MC, Vanzant E, Cuenca A, Cuenca AG, et al. Protective immunity and defects in the neonatal and elderly immune response to sepsis. J Immunol. 2014;192(7):3156–65.
278. Gentile LF, Nacionales DC, Lopez MC, Vanzant E, Cuenca A, Szpila BE, et al. Host responses to sepsis vary in different low-lethality murine models. PLoS One. 2014;9(5).
279. Galvão AM, Wanderley MSO, Silva RA, Filho CAM, Melo-Junior MR, Silva LA, et al. Intratracheal co-administration of antioxidants and ceftriaxone reduces pulmonary injury and mortality rate in an experimental model of sepsis. Respirology. 2014 Oct 1;19(7):1080–7.
280. Minasyan H. Sepsis and septic shock: Pathogenesis and treatment perspectives. J Crit Care. 2017 Aug 1;40:229–42.

281. Dickson K, Liu S, Zhou J, Langille M, Holbein BE, Lehmann C. Selective sensitivity of the gut microbiome to iron chelators in polybacterial abdominal sepsis. Med Hypotheses. 2018;120:68–71.
282. Brook I. Spectrum and treatment of anaerobic infections. J Infect Chemother. 2016 Jan 1;22(1):1–13.
283. Papp-Wallace KM, Endimiani A, Taracila MA, Bonomo RA. Carbapenems: Past, present, and future. Antimicrob Agents Chemother. 2011;55(11):4943–60.
284. Boucher HW, Talbot GH, Bradley JS, Edwards JE, Gilbert D, Rice LB, et al. Bad bugs, no drugs: no ESKAPE! An ppdate from the infectious diseases society of america. Clin Infect Dis. 2009;48(1):1–12.
285. Huang W, Xie R, Hong Y, Chen Q. Association between comorbid chronic obstructive pulmonary disease and prognosis of patients admitted to the intensive care unit for non-COPD reasons: A retrospective cohort study. Int J COPD. 2020;15:279–87.
286. Chen C-H, Lai C-C, Wang Y-H, Wang C-Y, Wang H-C, Yu C-J, et al. The impact of sepsis on the outcomes of COPD patients: A population-based cohort study. J Clin Med. 2018;7(11):393.
287. Perlman RL. Mouse models of human disease: an evolutionary perspective. Evol Med Public Heal. 2016;2016(1):170–176.
288. Guan X, Hou Y, Sun F, Yang Z, Li C. Dysregulated chemokine signaling in cystic fibrosis lung disease: a potential therapeutic target. Curr Drug Targets. 2016;17(13):1535–44.
289. Nelson AL, Ratner AJ, Barasch J, Weiser JN. Interleukin-8 secretion in response to aferric enterobactin is potentiated by siderocalin. Infect Immun. 2007 Jun;75(6):3160–8.
290. Choi E-Y, Kim E-C, Oh H-M, Kim S, Lee H-J, Cho E-Y, et al. Iron Chelator Triggers Inflammatory Signals in Human Intestinal Epithelial Cells: Involvement of p38 and Extracellular Signal-Regulated Kinase Signaling Pathways. J Immunol. 2004;172(11):7069–77.

291. Rene A, Massengale D, Quinn F, Yankaskas J, Weissman D, McClellan WT, et al. Reduced interleukin-8 production by cystic fibrosis airway epithelial cells. Am J Respir Cell Mol Biol. 1999;20(5):1073–80.
292. Gomez MA, Alisaraie L, Shio MT, Berghuis AM, Lebrun C, Gautier-Luneau I, et al. Protein tyrosine phosphatases are regulated by mononuclear iron dicitrate. J Biol Chem. 2010;285(32):24620–8.
293. Gira AK, Kowalczyk AP, Feng Y, Swerlick RA. Iron chelators and hypoxia mimetics inhibit IFNγ-mediated Jak-STAT signaling. J Invest Dermatol. 2009 Mar;129(3):723–9.
294. Gillette DD, Shah PA, Cremer T, Gavrilin MA, Besecker BY, Sarkar A, et al. Analysis of human bronchial epithelial cell proinflammatory response to Burkholderia cenocepacia infection: Inability to secrete IL-1 β. J Biol Chem. 2013;288(6):3691–5.
295. Alfaro-Moreno E, Torres V, Miranda J, Martínez L, García-Cuellar C, Nawrot TS, et al. Induction of IL-6 and inhibition of IL-8 secretion in the human airway cell line Calu-3 by urban particulate matter collected with a modified method of PM sampling. Environ Res. 2009;109(5):528–35.
296. Carolan EJ, Mower DA, Casale TB. Cytokine-induced neutrophil transepithelial migration is dependent upon epithelial orientation. Am J Respir Cell Mol Biol. 1997;17(6):727–32.
297. Sun Y, Wu F, Sun F, Huang P. Adenosine promotes IL-6 release in airway epithelia. J Immunol. 2008;180(6):4173–81.
298. Chow AW, Liang JF, Wong JS, Fu Y, Tang NL, Ko W. Polarized secretion of interleukin (IL)-6 and IL-8 by human airway epithelia 16HBE14o- cells in response to cationic polypeptide challenge. PLoS One. 2010 Aug;5(8):e12091.
299. Filkins LM, O'Toole GA. Cystic fibrosis lung infections: polymicrobial, complex, and hard to treat. PLoS Pathog. 2015;11(12):e1005258.
300. Reid DW, Anderson GJ, Lamont IL. Cystic fibrosis: Ironing out the problem of infection? Am J Physiol - Lung Cell Mol Physiol. 2008 Jul;295(1).

301. Moreau-Marquis S, Bomberger JM, Anderson GG, Swiatecka-Urban A, Ye S, O'Toole GA, et al. The ΔF508-CFTR mutation results in increased biofilm formation by *Pseudomonas aeruginosa* by increasing iron availability. Am J Physiol - Lung Cell Mol Physiol. 2008;295(1):25–37.
302. Yang F, Haile DJ, Wang X, Dailey LA, Stonehuerner JG, Ghio AJ, et al. Apical location of ferroportin 1 in airway epithelia and its role in iron detoxification in the lung. Am J Physiol Lung Cell Mol Physiol. 2005;289:14–23.
303. Park CH, Valore E V, Waring AJ, Ganz T. Hepcidin, a urinary antimicrobial peptide synthesized in the liver. J Biol Chem. 2001;276(11):7806–10.
304. Palmberg L, Larsson BM, Malmberg P, Larsson K. Induction of IL-8 production in human alveolar macrophages and human bronchial epithelial cells in vitro by swine dust. Thorax. 1998;53(4):260–4.
305. Ramezanpour M, Smith JLP, Ooi ML, Gouzos M, Psaltis AJ, Wormald PJ, et al. Deferiprone has anti-inflammatory properties and reduces fibroblast migration in vitro. Sci Rep. 2019;9(1):2378.